DIGITAL ACCESS TO
SCHOLARSHIP AT HARVARD

Development of Earth-Abundant Tin(II) Sulfide Thin-Film Solar Cells by Vapor Deposition

The Harvard community has made this article openly available.
Please share how this access benefits you. Your story matters.

Citation	Sinsermsuksakul, Prasert. 2013. Development of Earth-Abundant Tin(II) Sulfide Thin-Film Solar Cells by Vapor Deposition. Doctoral dissertation, Harvard University.
Accessed	April 17, 2018 4:11:25 PM EDT
Citable Link	http://nrs.harvard.edu/urn-3:HUL.InstRepos:11051177
Terms of Use	This article was downloaded from Harvard University's DASH repository, and is made available under the terms and conditions applicable to Other Posted Material, as set forth at http://nrs.harvard.edu/urn-3:HUL.InstRepos:dash.current.terms-of-use#LAA

(Article begins on next page)

© 2013 by Prasert Sinsermsuksakul

All rights reserved.

Professor Roy G. Gordon Prasert Sinsermsuksakul

Development of Earth-Abundant Tin(II) Sulfide Thin-Film Solar Cells by Vapor Deposition

ABSTRACT

To sustain future civilization, the development of alternative clean-energy technologies to replace fossil fuels has become one of the most crucial and challenging problems of the last few decades. The thin film solar cell is one of the major photovoltaic technologies that is promising for renewable energy. The current commercial thin film PV technologies are based on $Cu(In,Ga)Se_2$ and CdTe. Despite their success in reducing the module cost below $1/Wp, these absorber materials face limitations due to their use of scarce (In and Te) and toxic (Cd) elements. One promising candidate for an alternative absorber material is tin monosulfide (SnS). Composed of cheap, non-toxic and earth-abundant elemental constituents, SnS can potentially provide inexpensive PV modules to reach the global energy demand in TW levels.

Because of the high volatility of sulfur and various oxidation states of tin, non-stoichiometric chemical composition, traces of other phases (i.e. Sn, Sn_2S_3, and SnS_2), and elemental impurities (*e.g.* oxygen) are usually observed in SnS films obtained from various reported deposition techniques. First, we present a process to prepare pure, stoichiometric, single-phase SnS films from atomic layer deposition (ALD). The as-deposited SnS films exhibit several attractive properties, including suitable energy band gaps (E_g,~ 1.1 – 1.3 eV), a large absorption coefficient ($\alpha > 10^4$ cm^{-1}), and a proper carrier concentration ($[p] \sim 10^{15} – 10^{16}$ cm^{-3}). Then, heterojunction solar cells were fabricated from *p*-type SnS and *n*-type zinc oxysulfide

(Zn(O,S)). A record high active-area efficiency of 2.46 % was achieved via conduction band offset engineering by varying the oxygen-to-sulfur ratio in Zn(O,S).

Finally, we address two approaches potentially used for improving a device efficiency of the SnS solar cell. First, via doping to create an *n*-type SnS, a *p*-*n* homojunction device could be made. We present the processes and the results of doping SnS films with antimony and chlorine, potential *n*-type dopants. Second, by post-deposition heat treatment, an improvement in the transport properties of SnS film can be achieved. We discuss the effect of temperature and an annealing ambient (N_2, H_2S, and sulfur) on grain growth and the electrical properties of annealed SnS films.

Acknowledgements

Without the support from people around me, this thesis would not be possible. First and foremost, I would like to express my utmost gratitude to my advisor, Professor Roy G. Gordon, who made me realize and appreciate a quote from one of my favorite scientists, Thomas A. Edison: “I have not failed. I've just found 10,000 ways that won't work.” It is one thing to know the meaning, and quite another to actually experience it. During the last several years conducting research at Harvard, a lot of results did not turn out the way I hoped for; but Roy kept reminding me that there is no failed experiment as long as I have learned something from it. His wise words have taught me an invaluable lesson on how to conduct research, and perhaps approach life in general. I am also grateful for Roy’s kindness as a person; his generosity with his time, knowledge and advice, his unwavering support and encouragement, and his dedicated guidance on the work I have pursued, which is crystallized in this thesis.

The Gordon group was perhaps a second home during my time at Harvard. Throughout the last several years, I have had the fortune of collaborating with a wonderful group of people, who supported me both mentally and professionally. I learned a great deal from mentors such as Dr. Hongtao Wang, Dr. Sheng Xu, Dr. Hoon Kim, Dr. Harish Bhandari, and Dr. Jaeyeong Heo. Harish helped me tremendously with atomic layer deposition (ALD) reactor design and construction. Jaeyeong, in particular, taught me so many little things in science and always gave

constructive criticism and insightful suggestions. I acknowledge the help, advice and friendship of the Gordon alumni: Dr. Yeung (Billy) Au, Dr. Xinwei Wang, Dr. Yiqun Liu, Dr. Zhefeng Li, Dr. Wantae Noh, Dr. Jun-Jieh Wang, and Dr. Adam S. Hock. I appreciate the friendship and support offered by Dr. Sang Woon Lee, Dr. Norifusa Satoh, Jing Yang, Lauren Hartle, Kecheng Li, Xiabing Lou, Ashwin Jayaraman, and Lu Sun. Also, I thank my colleagues in the Gordon solar-cell subgroup, who worked closely with me: Dr. Sang Bok Kim, Leizhi Sun, Danny Chua, Helen Hejin Park, and Rachel Heasley. It has been a great pleasure working with them. I am also grateful to our lab administrators, Teri Howard and Marie Purcell, for their daily help.

Beyond the Gordon group, I would like to extend my thanks to the collaborators in the Buonassisi group of the Massachusetts Institute of Technology for their contributions to this dissertation: Katy Hartman, Rupak Chakraborty, Dr. Yaron Segal, Dr. Yun Seog Lee, and Professor Tonio Buonassisi. In addition, I am grateful to Professors Eric Mazur and Theodore Betley for serving on my committee. I thank Dr. Mark Winkler and Meng-Ju (Renee) Sher from the Mazur group for their help with the Hall measurements. I acknowledge the financial support of the Development and Promotion of Science and Technology Talents Project (DPST), Thailand, for giving me the opportunity to study in the United States.

Finally, I must sincerely thank my parents, who provided me everything a child could ask for: unconditional love, patience and deep understanding, providing support and hope, and teaching me right from wrong. They also encouraged and helped me build the foundation of my education. During my childhood, my parents always emphasized and taught me the value of an education, something that they both missed while growing up in less fortunate families. My mom

did not have an opportunity to attend a middle school. My dad is the only child among his six siblings who received a college degree. He had to help his family business during the day and attended college at night. Their stories made me feel privileged and obligated to do my only task, studying, to the best of my ability during my childhood. For the wisdom and opportunities they have given, I dedicate this dissertation to my parents.

Prasert Sinsermsuksakul
Cambridge, Massachusetts
April 2013

Contents

Abstract iii

Acknowledgements v

Table of Contents viii

List of Figures xi

List of Tables xiii

List of Publications xiv

List of Symbols and Acronyms xv

1 Introduction 1
1.1 Motivation 1
1.2 Characteristics of the photovoltaic cell 4
1.3 Thin film solar cell 5
1.4 Connection and organization of the dissertation 8

2 Atomic Layer Deposition of Tin(II) Sulfide Thin Films 10
2.1 Chapter abstract 10
2.2 Introduction 11
2.3 Experiment section 14
2.3.1 bis(*N*,*N'*-diisopropylacetamidinato)tin(II) 14
2.3.2 Atomic Layer Deposition of SnS 15
2.3.3 Characterization of ALD SnS thin film 16
2.4 Results and discussion 18
2.4.1 ALD growth behavior 18
2.4.2 Surface morphology and topography 20
2.4.3 Crystal structure 22
2.4.4 Film composition and purity 25
2.4.4.1 Phase purity 25
2.4.4.2 Stoichiometry 27
2.4.4.3 Elemental purity 28

2.4.5 Optical properties 29
2.4.6 Electrical properties 34
2.5 Conclusions 36

3 SnS/Zn(O,S) Heterojunction Solar Cells 38
3.1 Chapter abstract 38
3.2 Introduction 39
3.3 Experiment section 40
3.4 Results and discussion 43
3.5 Conclusions 50
3.6 Acknowledgements 51

4 Antimony-doped SnS Thin Films 52
4.1 Chapter abstract 52
4.2 Introduction 53
4.3 Experiment section 55
4.4 Results and discussion 57
4.4.1 SnS(Sb) film properties 57
4.4.2 EXAFS measurements on SnS(Sb) 61
4.5 Conclusions 68
4.6 Acknowledgements 68

5 Heat Treatment in SnS Thin Films 69
5.1 Chapter abstract 69
5.2 Introduction 70
5.3 Experiment Section 71
5.4 Results and discussion 72
5.4.1 Grain growth in heat-treated SnS films 72
5.4.2 Rapid thermal annealing 77
5.4.3 Electrical properties of heat-treated SnS films 79
5.4.4 Sulfur annealing 82
5.5 Conclusions 83
5.6 Acknowledgements 84

A Tin(II) Complex Precursors 85
A.1 Experiment Section 85
A.1.1 Synthesis of tin(II) precursors 85
A.1.2 Characterization 89
A.2 Results 90
A.2.1 Pictures of tin(II) precursors 90
A.2.2 ^{1}H and ^{13}C NMR spectrum 91
A.2.3 X-ray crystal structures 97
A.2.4 Thermal gravimetric analysis 99
A.3 Acknowledgements 99

B ALD SnS Films from Cyclic Amide of Tin(II) 100
B.1 Experiment Section 100
B.2 Results 102
B.2.1 ALD growth behavior 102
B.2.2 Surface morphology and topography 103
B.2.3 Crystal structure and film composition 104

C Chlorine-doped SnS Films 105

D Schematic Diagram of the Reactor 108

Reference 109

List of Figures

1.1 The record of best research-cell efficiency 3
1.2 *J-V* characteristics of a typical solar cell 5
1.3 The device structure of CIGS and CdTe thin film solar cells 6
1.4 The effects of parasitic resistances 7

2.1 Synthetic route of bis(*N*,*N'*-diisopropylacetamidinato)tin(II). 14
2.2 Saturation curve and growth rate of ALD SnS films from $Sn(amd)_2$ 18
2.3 The growth rate of SnS as a function of temperature 19
2.4 SEM images of SnS films (~ 100 nm-thick) 21
2.5 SEM images of SnS films (~ 300 nm-thick) 21
2.6 XRD spectra of SnS films 22
2.7 Raman spectra of SnS films 26
2.8 TEM image and SAED of SnS films 26
2.9 RBS spectrum of SnS films 27
2.10 XPS depth profiling of SnS films 28
2.11 Optical properties of SnS films 31
2.12 Absorption coefficient of SnS and other absorber materials 31
2.13 Calculated absorption coefficient of SnS 33

3.1 The effect of the conduction-band offset 40
3.2 The device structure of SnS/Zn(O,S) solar cell 41
3.3 *J-V* characteristics at different Zn(O,S) compositions 43
3.4 SEM image of SnS/Zn(O,S) solar cell 45
3.5 *J-V*, XRD, and IQE properties of SnS/Zn(O,S) solar cell 46
3.6 NREL-certified *J-V* characteristics of a champion SnS/Zn(O,S) solar cell 48
3.7 IQE modeling 49

4.1 SEM image of Sb-doped SnS films 57
4.2 SIMS depth profile of Sb-doped SnS films 58
4.3 XRD spectrum of Sb-doped SnS films 60
4.4 EXAFS data at the Sb edge of Sb-doped SnS films 63
4.5 Atomic arrangement of Sb in SnS and Sb_2S_3 and Sb metal 63
4.6 EXAFS modeling fits for Sb edge in Sb-doped SnS films 65

4.7 Fourier transformed EXAFS data and fits of Sb-doped SnS 66

5.1 Temperature profiles used for annealing SnS 71
5.2 SEM images of SnS films annealed in N_2 ambient....73
5.3 SEM images of SnS films annealed in H_2S ambient 73
5.4 SEM images of SnS films annealed in sulfur ambient 74
5.5 Cross-sectional SEM images of SnS films annealed in N_2, H_2S, and sulfur 75
5.6 XRD spectrum of SnS films annealed in N_2 and H_2S....76
5.7 SEM images of RTA SnS films in H_2S 77
5.8 SEM image of SnS films showing crack formation at grain boundary 78
5.9 Hall measurement results on annealed SnS films....80
5.10 Calculated defect formation enthalpies for intrinsic defects in SnS....81

A.1 Synthesis routes of tin(II) precursors....85
A.2 Pictures of tin(II) precursors 90
A.3 NMR spectrum of tin(II) amidinate....91
A.4 NMR spectrum of cyclic amide of tin(II) 94
A.5 X-ray crystal structures of tin(II) precursors 97
A.6 Thermal gravimetric analysis curves of tin(II) precursors....99

B.1 Saturation curve and growth rate of ALD SnS films from CAT 102
B.2 SEM images of SnS films....103
B.3 XRD spectrum of SnS film....104
B.4 RBS spectrum of SnS film....104

C.1 EDX of SnS films before and after exposure to chlorine 106
C.2 SEM images of chlorine-doped SnS films....107

D.1 Schematic diagram of the reactor 108

List of Tables

2.1 Crystal structure, optical and electronic properties of SnS films....................................23

4.1 Lattice constant and electrical properties of SnS(Sb) as a function of [Sb] 61
4.2 Structure model of SnS(Sb) for EXAFS..64
4.3 Best-fit EXAFS parameters for Sb-doped SnS...66

A.1 Crystallographic data for tin(II) compounds..98

C.1 Electrical properties of SnS(Cl)..107

List of Publications

Parts of this dissertation cover research reported in the following articles:

[1] Sinsermsuksakul, Prasert; Hartman, Katy; Kim, Sang Bok; Heo, Jaeyeong; Sun, Leizhi; Park, Helen Hejin; Chakraborty, Rupak; Buonassisi, Tonio; Gordon, Roy G. "Enhancing the efficiency of SnS solar cells via band-offset engineering with a zinc oxysulfide buffer layer" *Applied Physics Letters*. **102** (5), 053901.1-053901.5 (2013).

[2] Sinsermsuksakul, Prasert; Chakraborty, Rupak; Kim, Sang Bok; Heald, Steven M.; Buonassisi, Tonio; Gordon, Roy G. "Antimony-Doped Tin(II) Sulfide Thin Films" *Chemistry of Materials*. **24** (23), 4556-4562 (2012).

[3] Sinsermsuksakul, Prasert; Heo, Jaeyeong; Noh, Wontae; Hock, Adam S.; Gordon, Roy G. Atomic Layer Deposition of Tin Monosulfide Thin Films. *Advanced Energy Materials*. **1** (*6*), 1116-1125 (2011).

List of Symbols and Acronyms

Symbols

α	absorption coefficient
η	power-conversion efficiency of a solar cell under one sun
χ	electron affinity
d	film thickness
E_c	energy of conduction band edge
E_F	Fermi energy or Fermi level
E_g	energy of the band gap
E_v	energy of valence band edge
J	current density
J_{sc}	short-circuit current density
q	charge of an electron
R	reflectance
R_s	series resistance
R_{sh}	shunt resistance
T	transmittance
V	voltage
V_{oc}	open-circuit voltage

Acronyms

ALD	atomic layer deposition
AM1.5	standard terrestrial solar-spectrum of air mass 1.5
CAT	cyclic amide of tin(II): *rac*-1,3-Di-tert-butyl-4,5-dimethyl-1,3-diaza-2-stannacyclopentane-2-ylide [Sn(II)(μ-NBu^t)CH(CH_3)CH(CH_3)(μ-NBu^t)]
CBM	conduction band minimum
CBO	conduction band offset
CIGS	Cu(In,Ga)Se_2
CSS	closed space sublimation
CVD	chemical vapor deposition
CZTS	Cu_2ZnSnS_4
CZTSSe	$Cu_2ZnSn(S,Se)_4$
EDX	energy-dispersive x-ray spectroscopy
EQE	external quantum efficiency
EXAFS	extended x-ray absorption fine structure
FF	fill factor
IQE	internal quantum efficiency
NMR	nuclear magnetic resonance
RBS	Rutherford backscattering spectrometry
RIE	reactive ion etching
RTA	rapid thermal annealing
SEM	scanning electron microscopy

SIMS secondary ion mass spectrometry

$Sn(amd)_2$ tin(II) amidinate: bis(*N*,*N'*-diisopropylacetamidinato)tin(II) [$Sn(MeC(N\text{-}^{i}Pr)_2)_2$]

TCO transparent conductive oxide

TEM transmission electron microscopy

TGA thermal gravimetric analysis

VBM valence band maximum

XPS x-ray photoelectron spectroscopy

XRD x-ray diffraction

XRF x-ray fluorescence spectroscopy

XRR x-ray reflectivity

To my parents

for their love and support

ให้กับ ป่าป๊า ม่าม๊า

สำหรับ ความรักและกำลังใจ ที่ให้

Chapter 1

Introduction

1.1 Motivation

To sustain future civilization, the development of alternative clean-energy technologies to replace fossil fuels has become one of the most challenging problems of the last few decades. The current energy supply is unsustainable – environmentally, economically, and socially. One concern for carbon-based fuels, *e.g.* natural gas, oil and coal, is their negative effects on the ecosystem and climate change, the phenomenon known as the global warming. In addition to environmental issues, these traditional energy resources will be depleted in the near future.[1] The global energy demand has been predicted to grow by more than one-third by 2035.[2] Securing our energy supply will have a profound impact on the future foundation of the global economy and, inevitably, on societal well-being.

Among an array of renewable-energy resources such as wind power, biomass, geothermal energy and hydropower, solar energy is the most promising source because of its natural massive abundance, universal accessibility and long-term sustainability. Devices that convert solar power directly into electricity are generally termed photovoltaic (PV) devices, also referred to as solar cells. To generate enough power for practical applications, a number of solar cells are connected and assembled into a solar module. The main absorber materials used for current commercially available solar modules, with their highest confirmed terrestrial-module efficiencies included, are based on crystalline Si (22.9 ± 0.6%), large crystalline Si (21.4 ± 0.6%), multicrystalline Si (18.5 ± 0.4%), thin film polycrystalline Si (8.2 ± 0.2%), GaAs (24.1 ± 1.0%), copper indium gallium diselenide (CIGS, 15.7 ± 0.5%), and CdTe (15.3 ± 0.5%).[3]

Despite their promising potentials, one factor impeding utilization of photovoltaic systems from widespread expansion has been the high cost of the PV module. The aim to reduce the cost per watt has driven the shift from wafer-based crystalline silicon (the so-called first generation solar cells), which requires high-purity material and energy-intensive manufacturing, to thin film technology. Thin film technology uses less material and offers low processing cost and rapid production, which is suitable for large-scale manufacturing. In addition, a lot of effort has been put into the development of other technologies such as dye-sensitized solar cells, organic solar cells and quantum dot solar cells. These emerging technologies have shown some promising potential for even lower cost and faster production, but are not yet commercially available. They are still in the early stages of development with relatively low efficiency and questionable long-term device stability. Figure 1.1 shows the highest research-cell efficiencies of the different technologies over the last three decades.

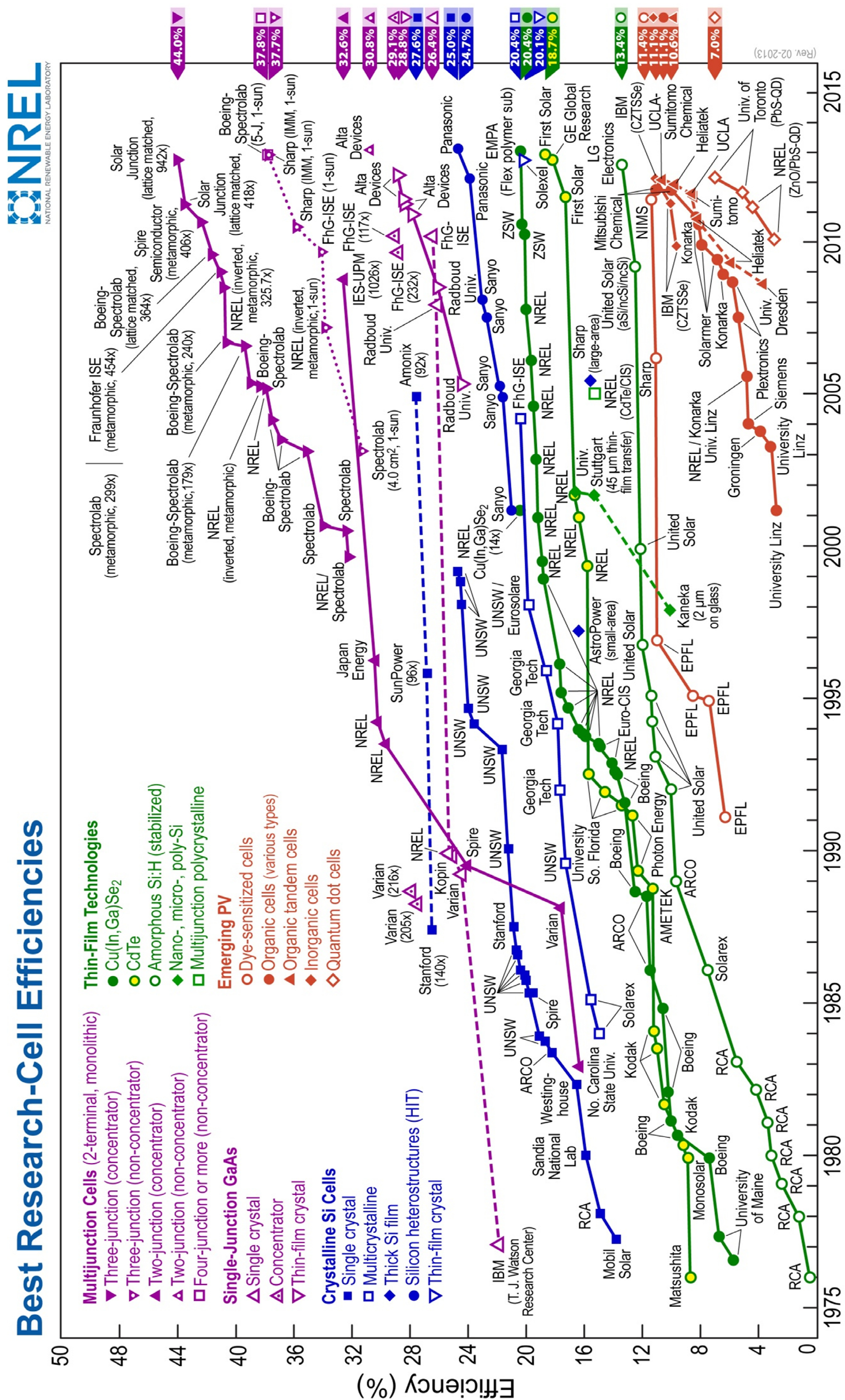

Figure 1.1: The record of best research-cell efficiencies [source: National Renewable Energy Laboratory (NREL), Feb 2013].

1.2 Characteristics of the photovoltaic cell

The solar cell is the basic building block of a photovoltaic module. It can be viewed as a two terminal device that behaves as a diode in the dark and generates a photovoltage under radiant illumination. This requires the device not only to absorb sunlight to create electron-hole pairs, but also to separate these charge carriers to be collected at the electrodes. The photovoltaic device operates in three basic steps: (i) carrier generation through photon absorption, (ii) charge carrier separation via an asymmetric junction, and (iii) carrier collection to the device terminals. The generation of photocurrent density J_{sc} in a solar cell depends on these three steps and thus relates to the incident light spectrum and the probability that an incident photon of energy E will deliver one electron to the external circuit. Therefore,

$$J_{sc} = q \int \mathrm{F}(E)\mathrm{EQE}(E)dE \quad (1.1)$$

where q is an electron charge, F(E) is the incident spectral flux density, and EQE(E) is the cell's external quantum efficiency. Figure 1.2 illustrates dark and illuminated current density versus voltage (J-V) characteristics of a typical solar cell. For a diode model, the net current density in the cell can be expressed as

$$J\,(V) = J_{dark}(V) - J_{sc} = J_o(e^{qV/nK_BT} - 1) - J_{sc} \quad (1.2)$$

where J_{sc} is a short circuit current density, J_o is a constant, K_B is Boltzmann's constant, n is an ideality factor, and T is temperature. The photovoltaic effect is operated from the bias voltage of 0 to V_{oc}, in which the device delivers power to an external load. The power density ($P = JV$) of a device thus depends on the operated voltage, which is controlled by the resistance of the load, and reaches a maximum value at some voltage V_m and current density J_m, as shown in Figure

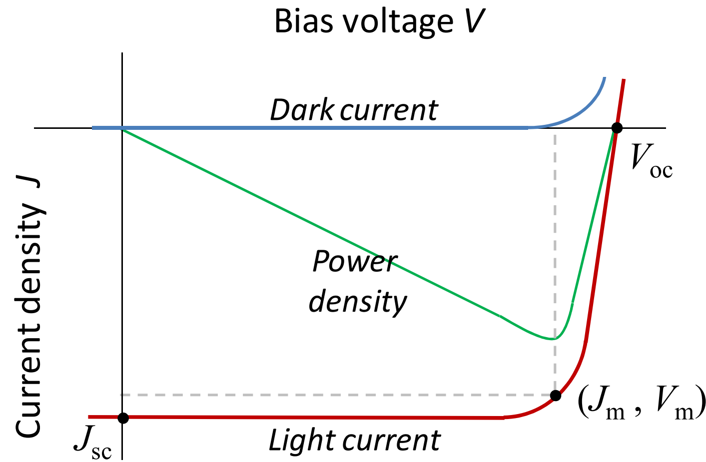

Figure 1.2: current density-voltage (*J-V*) characteristics of a typical solar cell under dark and illumination.

1.2. The maximum power-conversion efficiency, η, of a solar cell is then given by

$$\eta = \frac{J_{\mathrm{m}}V_{\mathrm{m}}}{P_i} = \frac{J_{\mathrm{sc}}V_{\mathrm{oc}}\mathrm{FF}}{P_i} \tag{1.3}$$

where P_{i} is the incident power density and FF is a fill factor, which is a ratio of $J_{\mathrm{m}}V_{\mathrm{m}}$ to $J_{\mathrm{sc}}V_{\mathrm{oc}}$. The performance of a solar cell is normally described by these four quantities, J_{sc}, V_{oc}, FF, and η of a standard testing condition (Air Mass 1.5 spectrum, an incident power density of 100 mW cm^{-2}, and a temperature of 25 °C).

1.3 Thin film solar cell

Thin film photovoltaic technology offers substantial cost reduction compared to the traditional wafer-based crystalline silicon because of advantages such as lower material use, fewer processing steps, simpler device processing and compatible manufacturing technology for rapid, continuous, large-area production. Unlike crystalline silicon (*c*-Si), the absorber layer used

in thin film technology is a direct band gap material which provides very strong absorptions. Therefore, these materials require much thinner thickness (~ 1-2 µm) to completely absorb sunlight, as compared to that of *c*-Si (~ 200 µm). Moreover, with a thinner absorber, a minority carrier diffusion length required for an effective carrier collection can also be reduced, resulting in a better defect and impurity tolerance and thus easier manufacture.

In general, thin film solar cells utilize a *p*-*n* junction that generates a local electric field to separate charge carriers. The structures of typical thin film solar cells are illustrated in Figure 1.3. Both devices essentially have the same basic structure: back contact/*p*-type absorber layer/*n*-type buffer layer/n^+-type emitter/top contact/anti-reflection coating (not shown), which are

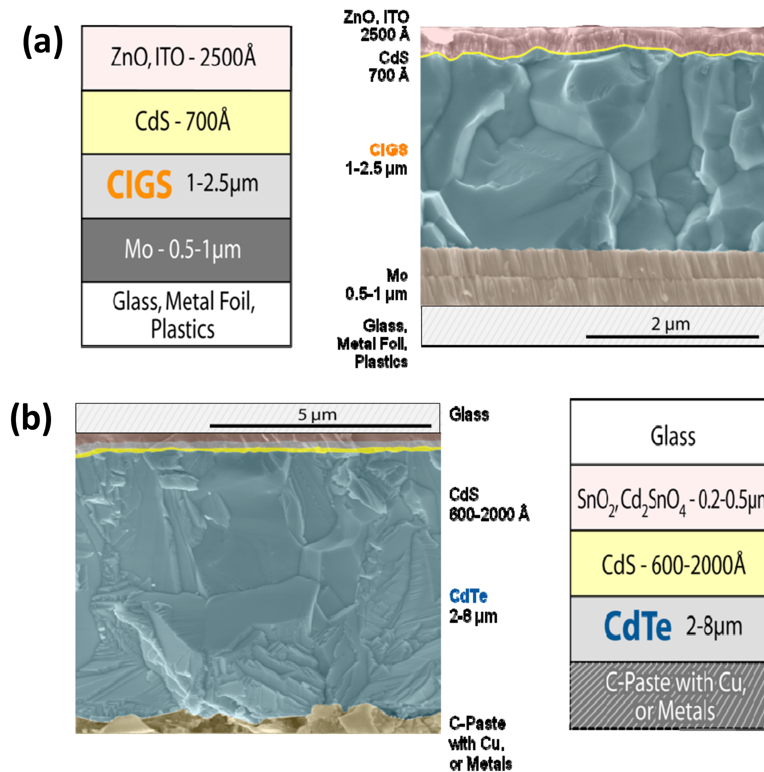

Figure 1.3: The device structures of **(a)** CIGS substrate solar cell (glass/Mo/CIGS/CdS/ZnO/ITO) and **(b)** CdTe superstrate solar cell (glass/SnO_2:F/Cd_2SnO_4/CdS/CdTe/Metals). [source: National Renewable Energy Laboratory (NREL)]

deposited on a cheap substrate, typically soda-lime glass. To obtain an efficient device, material in each layer needs to have proper optical, electrical and transport properties and exhitbit suitable interface properties when combined into a device stack. For example, the absorber material should have a suitable optical band gap, a high optical absorption coefficient, a high quantum yield for the excited carriers, a long carrier diffusion length, and a low recombination velocity. In a real device, parasitic resistances, *i.e.*, series resistance (R_s) and shunt resistance (R_{sh}), can play a role in the efficiency of the cell (Figure 1.4). To reduce series resistance, the material used for contact need to be highly conductive; metals can serve best. Nonetheless, to let the light pass into the absorber layer in the bottom part of the cell, metal cannot be used for the top layers and a conductive material with a high band gap, *e.g.*, TCO, is normally selected for its transparency. A detailed review of device structure and desired material properties used in thin film solar cells

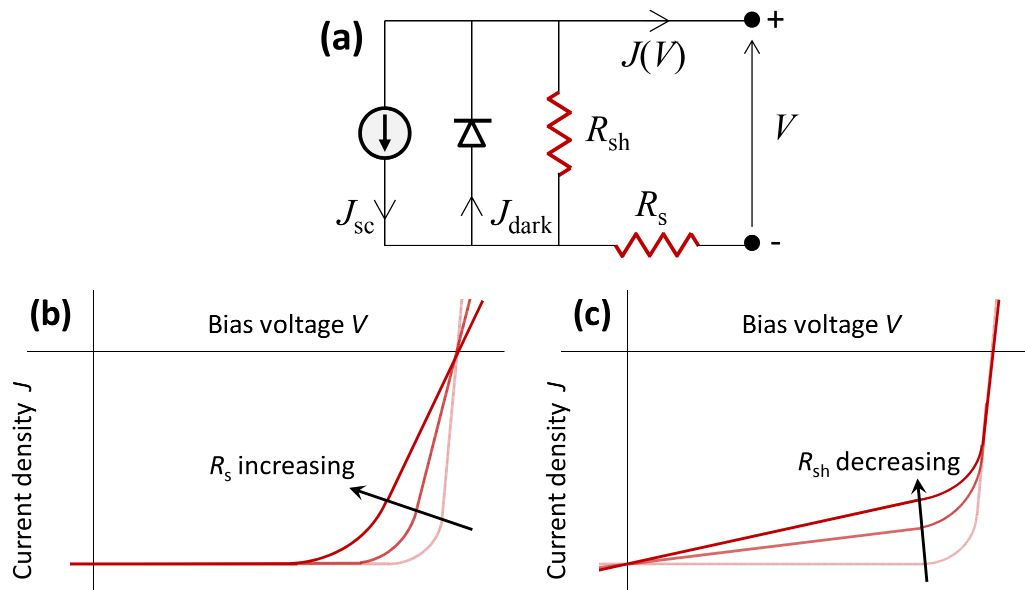

Figure 1.4: **(a)** Equivalent circuit of a solar cell with the effect of **(b)** series resistance (R_s) and **(c)** shunt resistance (R_{sh}). [Adapted from Nelson, J., *The Physics of Solar Cells*. Imperial College Press: London, 2003.]

can be found in Ref. [4-6].

1.4 Connection and organization of the dissertation

Today, the most developed thin film solar cells are based on amorphous silicon (*a*-Si), CIGS and CdTe. Photovoltaic modules using these materials have achieved the lowest cost per watt of any technology, less than $1.0/Wp and are continually decreasing. Nevertheless, these absorber materials still have some limitations; the growth rate of *a*-Si is far too slow to allow the production of inexpensive cells and its cell efficiency is still relative low (Figure 1.1). CIGS and CdTe cells contain toxic (Cd) and require scarce elements (In and Te) from the Earth's crust, which makes manufacturing scalability to worldwide electricity production relatively unrealistic. For instance, estimates indicate worldwide production of indium can support a CIGS production capacity of approximately 70 GW/yr, well below the desired terawatt level.[7] The abundance of tellurium is even lower. The constraints in environmental sensitivity and material availability urge a development of alternative absorber materials.

Tin (II) sulfide (SnS) is among the ongoing investigated earth-abundant materials such as Cu_2O,[8] Cu_2S,[9] FeS_2,[10,11] $Cu_2ZnSn(S_xSe_{1-x})_4$,[12] and $ZnSnP_2$.[13] SnS has a suitable band gap (E_g ~ 1.1 - 1.5 eV),[14,15] strong optical absorption ($\alpha > 10^4$ cm^{-1}),[16] and proper carrier concentration ([p] ~ 10^{14} - 10^{17} cm^{-3}).[17] In addition, the double layer held by van der Waals forces in SnS is expected to give a chemically inert surface with few surface states.[18] This defect-tolerant surface might reduce the carrier recombination loss due to defects at *p*-*n* junctions and at grain boundaries. Despite these promising properties, thin film solar cells based on SnS absorbers have

not achieved a conversion efficiency higher than 1.3%,[19] while theoretically such cells should be able to reach Shockley-Queisser efficiency limit of 32%. This poor performance may be due to defects and/or impurities in SnS layers that results from the preparation methods used to make the films.

This dissertation presents the development of an earth-abundant SnS-based thin film solar cell. Its aim is to investigate the potentials of SnS as an alternative absorber material and develop some understanding of the material system as well as the device design, knowledge which can leverage learning to other thin film photovoltaic systems. Chapter 2 introduces a deposition of SnS from ALD using a novel Sn(II) amidinate precursor and a detailed study of the ALD process and material properties of SnS. Chapter 3 presents a photovoltaic device made from SnS/Zn(O,S) heterojunction and improved efficiency via conduction-band offset engineering. Chapter 4 provides a route to adjust the electrical properties of SnS through antimony doping; EXAFS analysis was performed to study the chemical environment of antimony in the doped films. Chapter 5 summarizes the effects of heat treatment in N_2, H_2S, and sulfur ambient on grain growth and the electrical properties of SnS films.

Chapter 2

Atomic Layer Deposition of Tin(II) Sulfide Thin Films

2.1 Chapter abstract

Thin film solar cells made from earth-abundant, non-toxic materials are needed to replace the current technology that uses $Cu(In,Ga)(S,Se)_2$ and CdTe, which contain scarce and toxic elements. One promising candidate absorber material is tin monosulfide (SnS). In this report, pure, stoichiometric, single-phase SnS films were obtained by atomic layer deposition (ALD) using the reaction of bis(*N*,*N'*-diisopropylacetamidinato)tin(II) [$Sn(MeC(N\text{-}^iPr)_2)_2$] and hydrogen sulfide ($H_2S$) at low temperatures (100 to 200 °C). The direct optical band gap of SnS is around 1.3 eV and strong optical absorption ($\alpha > 10^4$ cm^{-1}) is observed throughout the visible and near-infrared spectral regions. The films are p-type semiconductors with carrier concentration on the order of 10^{16} cm^{-3} and hole mobility 0.8-15 cm^{2}V^{-1}s^{-1} in the plane of the films. The electrical properties are anisotropic, with three times higher mobility in the direction through the film, compared to the in-plane direction.

2.2 Introduction

To achieve cost-effective thin film solar cells for large-scale production of solar energy, the absorbing semiconductor material used in the device needs to satisfy many requirements. First, the constituent elements should be inexpensive, non-toxic and abundant. Second, to obtain high energy conversion efficiency, the material should have appropriate optical and electrical properties such as a suitable optical band gap, a high optical absorption coefficient, a high quantum yield for the excited carriers, a long carrier diffusion length, and a low recombination velocity. With these characteristics in mind, tin(II) sulfide (SnS) satisfies some of these criteria and thus is a promising candidate as an absorber material for solar cells. Its constituent elements (tin and sulfur) are inexpensive, environmental friendly and abundant in nature. This feature gives it an advantage over the current best-developed thin film photovoltaic (PV) cells made from $Cu(In,Ga)(S,Se)_2$ (CIGS) and CdTe, which contain toxic Cd and the rare elements In, Ga, Se, and Te. Moreover, the binary compound SnS provides much simpler chemistry than multicomponent $Cu_2ZnSn(S,Se)_4$ (CZTSSe), one of the most promising earth-abundant absorber materials, with a solar conversion efficiency up to 11.1%.[20] In addition, SnS has proper optical properties for PV applications; it has an indirect optical band gap of 1.0-1.1 eV and a high absorption coefficient (greater than 10^4 cm^{-1}) above the direct absorption edge at 1.3-1.5 eV.[16,19,21-23] SnS crystallizes in an orthorhombic unit cell, with lattice parameters of a = 4.334 Å, b = 11.200 Å, and c = 3.987 Å,[24] which can be viewed as a distorted rocksalt (NaCl) structure. It is composed of double SnS layers perpendicular to the b axis with tin and sulfur atoms covalently bonded within the layers and weak van der Waals bonds between the layers.[25] The double layer held by van der Waals forces in SnS is expected to give a chemically inert surface

with few surface states.[18] This defect-tolerant surface might reduce the carrier recombination loss due to defects at *p-n* junctions and at grain boundaries.

Despite these promising properties, solar cells based on SnS absorbers have not achieved conversion efficiency higher than 1.3%,[19] while theoretically such cells should be able to reach the Shockley-Queisser efficiency limit of 32%. This poor performance may be due to defects and/or impurities in SnS layers that result from the preparation methods used to make the films.

Tin(II) sulfide films have been deposited from various techniques, which can be roughly divided into three categories. The first method involves solution-based techniques such as chemical bath deposition (CBD),[18,26] successive ionic layer adsorption and reaction (SILAR),[27,28] and electrochemical deposition (ECD).[21,22,29,30] A second technique is physical vapor deposition from a SnS target such as thermal evaporation,[31-33] RF sputtering,[14] and electron beam evaporation.[34] The last method uses transport by chemical vapors such as chemical spray pyrolysis,[35-37] chemical vapor deposition (CVD),[23,38-41] and atomic layer deposition (ALD).[42] Due to the various oxidation states of tin (0, +2, and +4), traces of other phases (*i.e.*, Sn, Sn_2S_3, and SnS_2) have often been co-deposited into the films as reported by several authors.[21,31,41,43] To prevent the formation of the Sn_2S_3 and SnS_2 phases, relatively high deposition temperatures are needed in thermal evaporation (above 275 °C)[32] and CVD (above 500 °C)[40,44]. Although a pure SnS phase can be obtained at certain substrate temperatures or growth conditions, the chemical composition of the films usually deviates from ideal stoichiometric SnS by as much as 10-20%. For vapor-based deposition techniques such as chemical spray pyrolysis and thermal evaporation, this effect is attributed to the high vapor pressure of sulfur, which evaporates out

from the deposited film.[15,35] Non-stoichiometric SnS caused by either Sn^{2+} vacancies[45,46] or excess tin atoms[23,34] contains deep acceptor states with an activation energy (E_a) in a range between 0.22 and 0.45 eV[23,34,45-49] depending on the deposition technique. The deep acceptor states, which could act as carrier recombination catalysts, are expected to lower the solar energy conversion efficiency. In addition to other binary compounds and the non-stoichiometric problem, solution-based deposition methods such as CBD and ECB result in films contaminated by oxygen in the forms of SnO_2 or $[SO_4]^{-2}$.[21,22] Chlorine contamination was also reported in SnS films grown by CVD using tin chloride.[23, 38]

ALD SnS was reported by Kim *et al.* using the reaction of tin 2,4-pentanedionate ($Sn(acac)_2$) and hydrogen sulfide (H_2S).[42] However, the growth rate was relatively low (0.24 Å cycle^{-1}), which might be partly because Sn-O bonds (532 kJ mol^{-1}) are stronger than Sn-S bonds (464 kJ mol^{-1}),[50] resulting in an unfavorable thermodynamic enthalpy change. Optical properties were measured only on a very thin film (23 nm); crystal structure and electrical properties of this film were not studied.

In this chapter, we present ALD of pure, stoichiometric, single-phase SnS films from the reaction of bis(*N*,*N'*-diisopropylacetamidinato)tin(II) $[Sn(MeC(N\text{-}^iPr)_2)_2]$ (referred to as $Sn(amd)_2$ in this work) and H_2S at substrate temperatures between 100 and 200 °C. The utilization of a Sn(II), rather than Sn(IV) precursor used in previously reported CVD processes,[23,40,43,44] mitigates possible contamination by the Sn_2S_3 and SnS_2 phases. Moreover, the deposition temperature is relatively low, thus overcoming the problem of sulfur-deficiency due to sulfur re-evaporation. Low temperature growth of SnS also enables the formation of solar cells

on thermally sensitive substrates such as flexible polymers. The deposited SnS films were thoroughly characterized by their elemental composition, surface morphology, crystal structure, optical, and electrical properties**.** These SnS films possess high potential for use in photovoltaic devices.

2.3 Experiment Section

2.3.1 bis(*N*,*N'*-diisopropylacetamidinato)tin(II)

The tin precursor, bis(*N*,*N'*-diisopropylacetamidinato)tin(II), was prepared according to the synthetic route depicted in Figure 2.1, which was adopted from the work by Lim *et al.*[51] A solution of methyllithium (1.6 M in Et_2O, 20 mL, 0.032 mol) was added dropwise to a solution of 1,3-diisopropylcarbodiimide (4.0 g, 0.032 mol) in Et_2O (75 mL) at −78 °C. The solution was allowed to warm up to room temperature and stirred for an additional two hours. This colorless solution was then slowly added to a solution of tin(II) chloride (reagent grade 98%, 3.0 g, 0.016 mol) in Et_2O (50 mL). This reaction mixture was stirred for 15 hours. Then, the solvent was

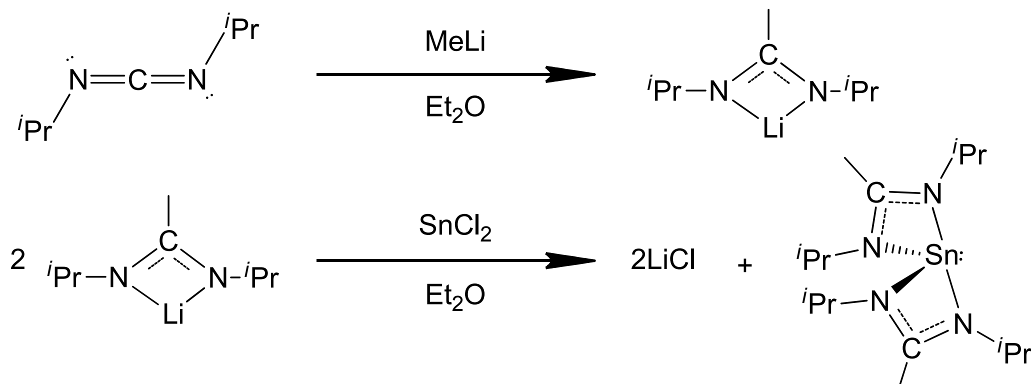

Figure 2.1: Synthetic route of bis(*N*,*N'*-diisopropylacetamidinato)tin(II).

removed under vacuum. The resulting white solid was extracted with pentane (150 mL) and filtered through Celite on a glass frit to remove LiCl salt. The resulting colorless filtrate was placed under vacuum to remove pentane, giving a white powder. Subsequent sublimation at 90 °C and 30 mTorr for three hours yielded pure white crystals (5.2 g, 81%). ^{1}H NMR (C_6D_6, 500 MHz): δ 3.67(sep, J = 6.5, 4H), δ 1.55(s. 6H), δ 1.28(d, J= 6.5, 24H), ^{13}C NMR (C_6D_6, 100 MHz, δ) 165.4, 47.6, 25.5, 12.2 EA: Calcd (%) C 47.90, H 8.54, N 13.97 found (%) C 47.72, H 8.57, N 13.99.

2.3.2 Atomic layer deposition of SnS

SnS thin films were deposited in a custom-built hot-wall ALD reactor[52] from the reaction of $Sn(amd)_2$ and H_2S. The tin precursor was kept at a constant temperature of 95 °C which gives a vapor pressure of 0.64 Torr, as measured by a capacitance manometer. A gas mixture of 4% H_2S in N_2 (Airgas Inc.) was used as the source of sulfur. H_2S is a toxic, corrosive and flammable gas (lower flammable limit of 4%);[53] thus, it should be handled with caution. An appropriate reactor design for H_2S compatibility can be found elsewhere.[54] Purified N_2 gas was used for assisting the delivery of $Sn(amd)_2$ vapor from the precursor container to the deposition zone and also for purging between each precursor pulse. The Sn precursor and H_2S injection were done by using the stop-flow ALD mode. Detailed explanation of the stop-flow ALD mode and the valve operation procedure can be found elsewhere.[55,56] The exposures from each single dose of $Sn(amd)_2$ and H_2S were estimated to be 0.50 and 0.36 Torr·s, respectively. By changing the number of tin precursor and H_2S doses, reproducible variations in the total precursor exposure were achieved. The N_2 purge time between each precursor pulse was set at 10 s, which is

sufficient to remove the excess precursor and reaction by-products. The cycles of sequential alternation between Sn(amd)$_2$ and H_2S were repeated until the desired film thickness was reached.

2.3.3 Characterization of ALD SnS thin film

Surface morphology and topology of the films were examined by using field-emission scanning electron microscopy (FESEM, Zeiss, Ultra-55). The film thickness was determined using a combination of cross-sectional SEM and X-ray fluorescence spectroscopy (XRF, Spectro, Xepos-III); the average thickness of rough films was determined by XRF utilizing a calibration curve of Sn $L_{\alpha 1}$ line intensity (count min^{-1}) versus the film thickness of smooth films measured by cross-sectional SEM. The crystal structure of the SnS films was characterized by X-ray diffraction (XRD, PANalytical X'Pert Pro) with Cu K_{α} radiation (λ = 1.542 Å) using θ-2θ scan. Raman spectroscopy (Renishaw, inVia Raman microscope) with an exciting wavelength of 633 nm and transmission electron microscopy (TEM, JEOL 2100) were employed to check for the presence of any additional phases of tin sulfide. The elemental composition and the purity of the films were determined by Rutherford backscattering spectrometry (RBS, Charles Evans RBS and Ionex 1.7 MV Tandetron), X-ray photoelectron spectroscopy (XPS, Surface Science, SSX-100), and time-of-flight secondary ion mass spectroscopy (TOF-SIMS).

The optical transmittance (T) and reflectance (R) were recorded at normal incidence using a UV-Vis-near IR spectrophotometer with an integrating sphere (Hitachi U-4100) in the wavelength range of 400 to 2500 nm. The absorption coefficient (α) and the optical band gap (E_g) were calculated from the measured optical transmittance and reflectance. The lateral

resistivity, carrier concentration and carrier mobility of the films were determined from Hall measurement according to the Van der Pauw method at room temperature. Indium pads were deposited by soldering to provide an ohmic contact to the SnS films.[57,58] The current was supplied from a Keithley 6220 Current Source and the voltage was measured by Keithley 6514 Electrometer with input impedance > 200 TΩ. Due to fluctuations of the current source, the errors of carrier concentration and mobility, determined from standard deviation of the Hall voltage, are roughly 20% or less. The vertical resistivity of SnS film was determined by *I*-*V* measurement from the slope of a plot of resistance through Au/SnS/Au stacks versus 1/area. The top Au electrodes were squares with sides 100, 200, 300, or 500 μm long, evaporated through a shadow mask. SnS films outside the area of the top Au electrode were removed by reactive ion etching (RIE, Nexx Systems, Cirrus 150) using Cl_2 plasma.

2.4 Results and Discussion

2.4.1 ALD growth behavior

Figure 2.2a and 2.2b show the effect of $Sn(amd)_2$ and H_2S exposures on the growth per cycle of SnS films deposited for 1000 cycles at a substrate temperature of 120 °C. To saturate the surface reactions, minimum exposures of 1.5 and 1.1 Torr·s of $Sn(amd)_2$ and H_2S are required for each ALD cycle, respectively. The thicknesses of SnS films are uniform across the deposition zone (30 cm in length) within the XRF measurement error (~3%). With lower exposure to either precursor, the film thickness at the outlet is roughly 10-15% thinner than that at the inlet. Unless mentioned otherwise, exposures of 1.5 Torr·s of $Sn(amd)_2$ and 1.1 Torr·s of H_2S were employed in subsequent experiments. Figure 2.2c shows the linear relationship between the film thickness and the number of cycles, which is the characteristic of ideal layer-by-layer ALD growth. From

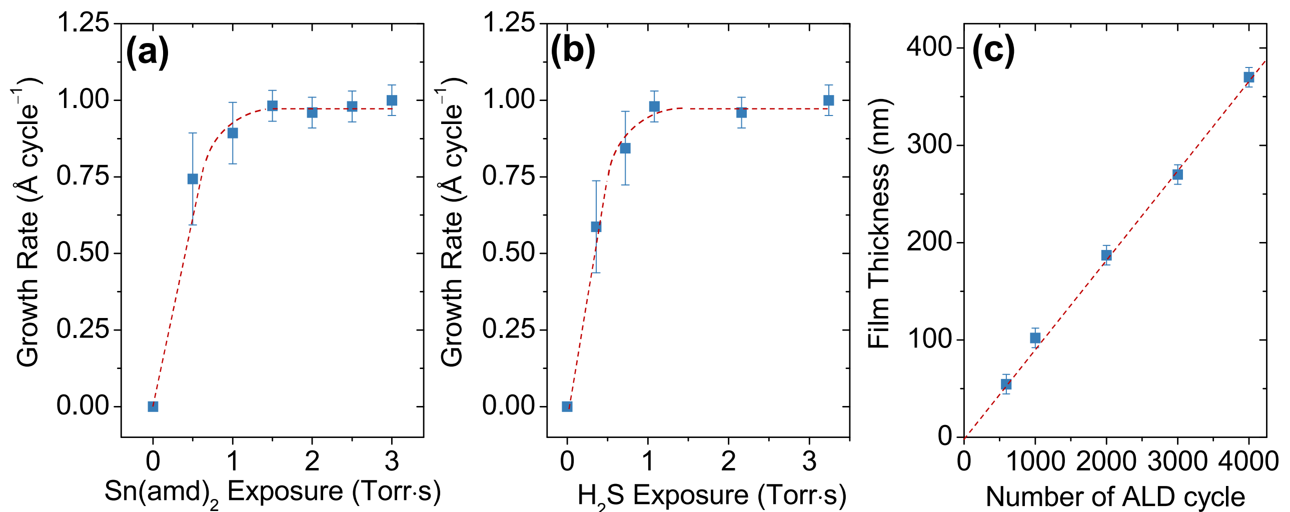

Figure 2.2: The growth rate of SnS films at a deposition temperature of 120 °C for different exposures of **(a)** Sn precursor at fixed H_2S exposure of 2.2 Torr·s and of **(b)** H_2S at fixed Sn precursor exposure of 1.5 Torr·s. **(c)** The thickness of SnS films on SiO_2 substrates using 1.5 Torr·s of Sn precursor and 1.1 Torr·s of H_2S exposure as a function of the number of ALD growth cycles at 120 °C.

the slope, the deposition rate of SnS at 120 °C on a thermal oxide (SiO_2) substrate is 0.90 ± 0.02 Å $cycle^{-1}$. A small positive y-intercept within the measurement error indicates that ALD SnS initiates growth immediately without any incubation delay on SiO_2 surfaces.

The growth rates of SnS films (Figure 2.3) remain roughly constant over the deposition temperature range of 100-250 °C with slightly decreasing values toward higher temperatures. The growth rate at the inlet and the outlet of the deposition zone are the same between 100 and 200 °C, indicating uniform film deposition across 30 cm length within this temperature range. The growth rate difference between the inlet and the outlet becomes noticeable at 250 °C and dramatically increases at 300 °C. This thickness non-uniformity above 250 °C is the result of tin precursor decomposition at high temperature, indicated by carbon detection in these films by XPS, which will be discussed later. Based on this result, the ALD temperature window for SnS film is between 100 and 200 °C. The growth rate of 0.86-0.90 Å $cycle^{-1}$ presented here is about 4

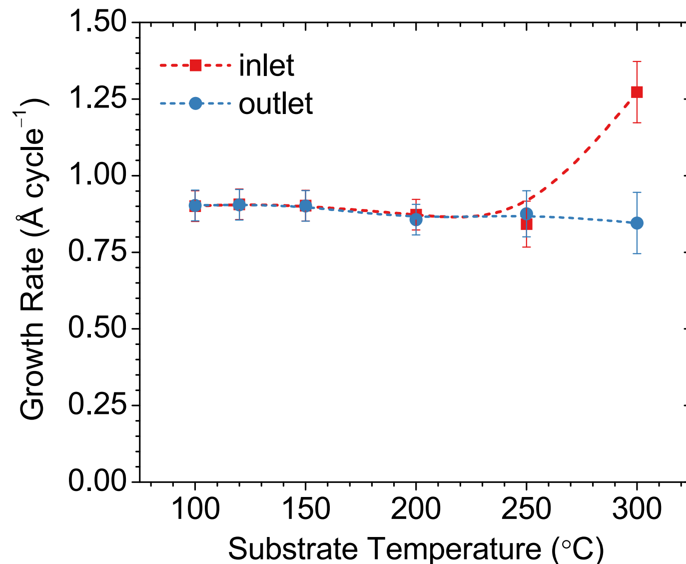

Figure 2.3: The growth rates of SnS films deposited between 100 and 300 °C at the inlet and outlet of the deposition zone (30 cm in length).

times higher than the value (0.22-0.24 Å $cycle^{-1}$) obtained from a β-diketonate precursor.[42]

2.4.2 Surface morphology and topography

Figure 2.4 shows the surface morphologies of ~90 nm-thick SnS films (1000 cycles) deposited at 120, 200, 250, and 300 °C, as taken by SEM. At 120 °C, the SnS film is composed of small grains with a rectangular-plate shape coalescing together. From the cross-sectional view, the lateral grain size of the film at 200 °C is noticeably larger than at 120 °C. At 250 and 300 °C, sharp crystal facets can be observed on each SnS grain which indicates improved crystallinity of the films. In general, the grain size and crystallinity of SnS increases with increasing growth temperature. Nonetheless, the film surface becomes much rougher above 250 °C. The effect of crystallinity and surface roughness can be observed by eye; below 200 °C, the SnS films appear smooth, shiny, uniform, and pin-hole free. In contrast, the films deposited above 250 °C look rough and have several pin-holes.

Due to high surface roughness, pin-hole problems, and precursor decomposition at high growth temperatures, thicker SnS films were deposited for further optical and electrical characterization only at substrate temperatures of 200 °C or below. The SEMs of SnS films deposited for 4000 cycles at 120 °C (~370 nm) and 200 °C (~330 nm) are shown in Figure 2.5. From the plane-view, the grain shapes of thicker SnS films are elongated platelets oriented perpendicular to the substrate surface. From the cross-sectional view, the films have a columnar structure with grain boundaries perpendicular to the substrate. The grain size in the elongated direction is about the same size as the film thickness.

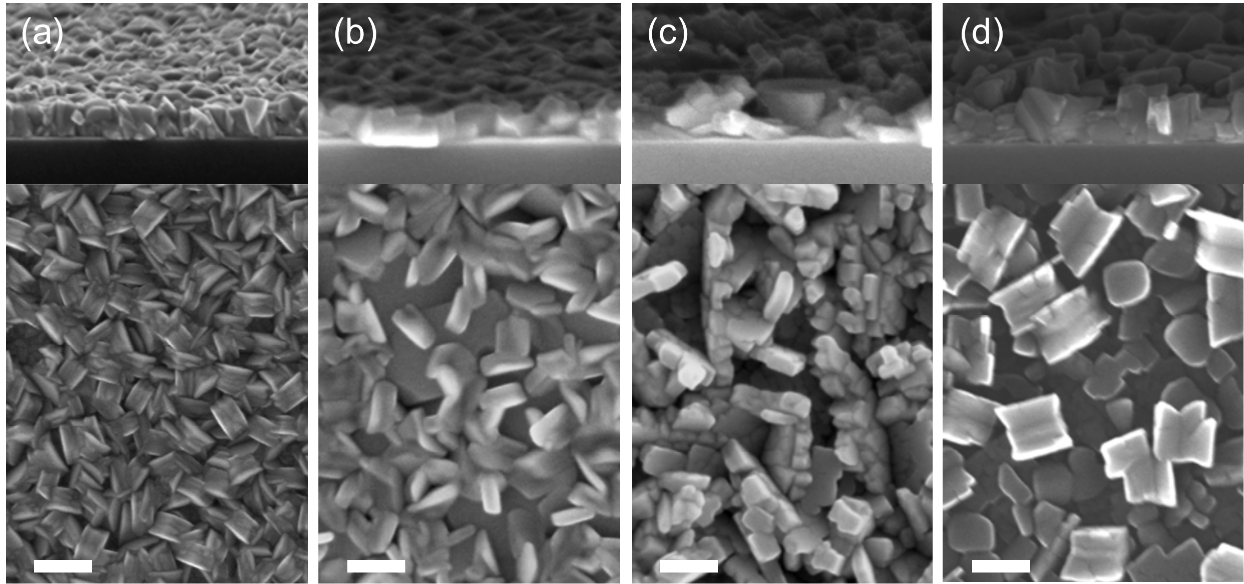

Figure 2.4: Plane-view and cross-sectional (12° tilt) SEM images of SnS films deposited on thermal oxide (SiO_2) for 1000 ALD cycles at **(a)** 120 °C, **(b)** 200 °C, **(c)** 250 °C, and **(d)** 300 °C. The scale bar is 200 nm.

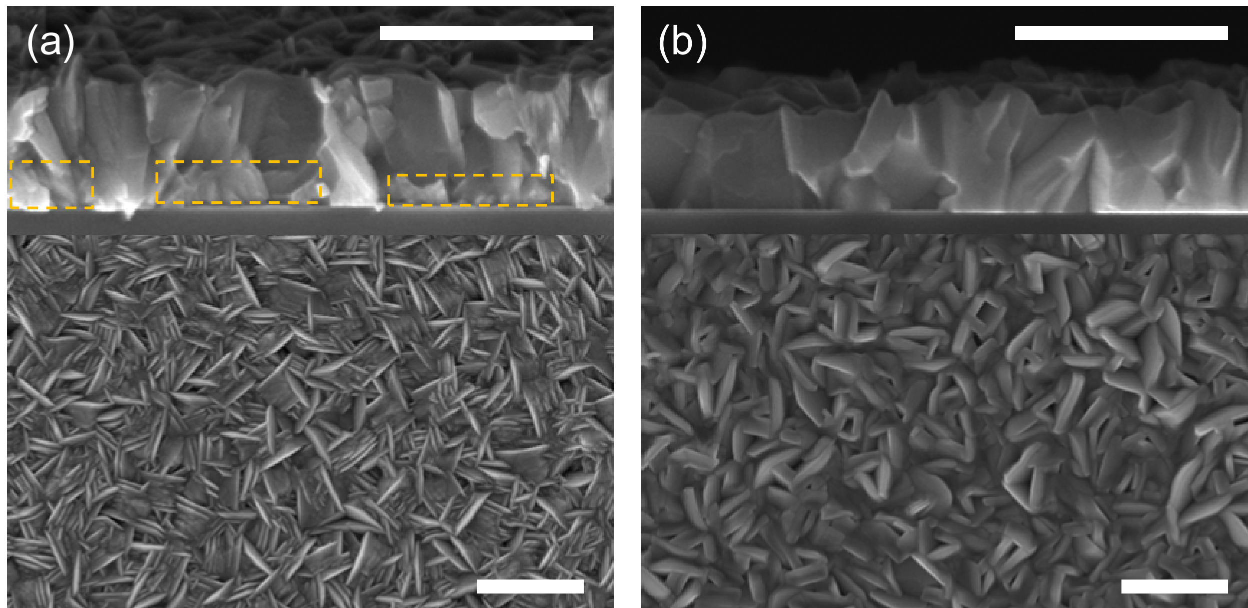

Figure 2.5: Plane-view and cross-sectional (12° tilt) SEM images of SnS films deposited on thermal oxide (SiO_2) for 4000 ALD cycles at **(a)** 120 °C and **(b)** 200 °C. The boxes in the cross-sectional SEM of **(a)** indicate the smaller grains formed during the initial film growth. The scale bar is 500 nm.

2.4.3 Crystal structure

Figure 2.6 shows the XRD patterns of SnS films deposited at 120 and 200 °C and at two different film thicknesses for each substrate temperature. These XRD spectra correspond to the known orthorhombic structure of SnS with the average lattice parameters of a = 4.30 Å, b = 11.20 Å, and c = 3.99 Å, calculated from least square fitting to the Bragg peaks. The crystal lattice parameters of the SnS films match well with Herzenbergite SnS (*JCPDS* No. *39-0354, a* = 4.3291 Å*, b* = 11.1923 Å*, c* = 3.9838 Å*).* Table 2.1b summarizes the main Bragg peaks of SnS and the average grain size calculated from the Scherrer formula.[59] The Bragg angle θ and full width at half maximum (FWHM) of each XRD peak were determined by fitting a Gaussian distribution to the experimental values. The shape factor used for the calculation is 0.9 (spherical grain shape). Since the grain shape is not exactly spherical, the calculated values only present a rough estimation for comparison.

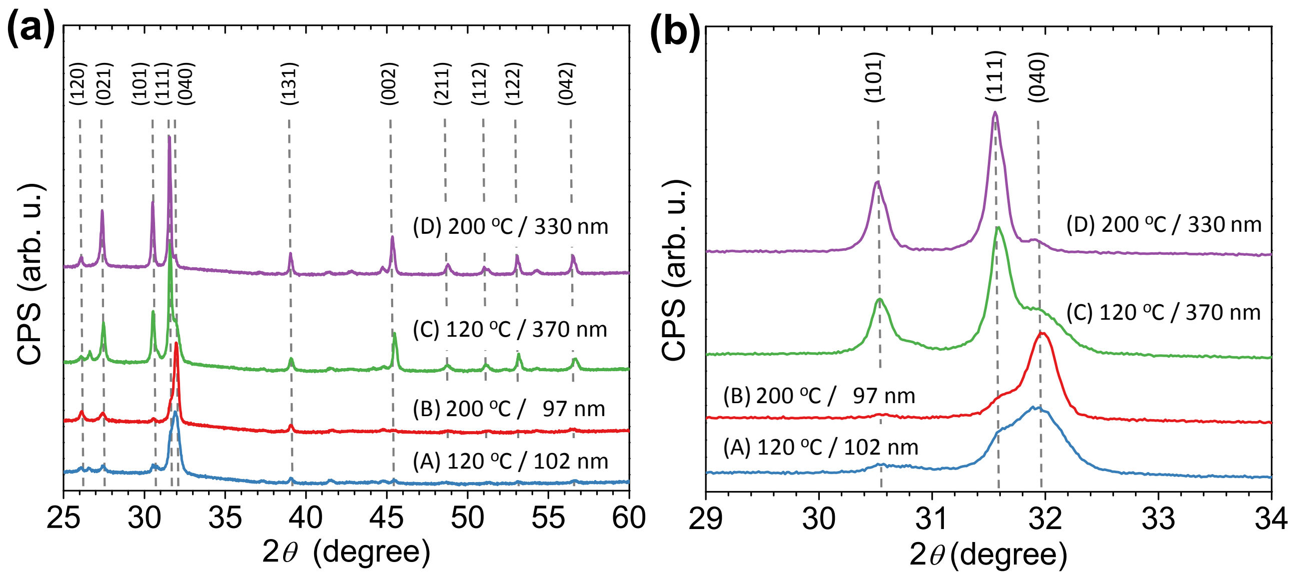

Figure 2.6: XRD spectra of SnS films deposited at 120 °C and 200 °C and at two different film thicknesses for each substrate temperature. **(b)** is the expansion of **(a)** to clearly show (111) and (040) peaks.

Table 2.1: Properties of SnS films deposited at **(a)** two different temperatures and thicknesses, compared to JCPDS card #039-0354; (b) Bragg angle θ and calculated grain size τ for each {*hkl*} plane; **(c)** the ratio of intensities of (111), (101), and (002) peaks normalized by (040) peak; **(d)** optical energy gap; **(e)** lateral resistivity ρ, hole density, and hole mobility μ_p.

	Sample	**A**	**B**	**C**	**D**	039-0354
(a)	T_{sub} (°C)	120	200	120	200	-
	Film Thickness (nm)	102	97	370	330	-
(b)	*hkl*	2θ , τ (nm)				
	120	26.08 , 31	26.11 , 29	-	26.09 , 46	26.0094
	021	27.46 , 29	27.42 , 29	27.27 , 40	27.40 , 46	27.4719
	101	-	-	30.53 , 41	30.53 , 49	30.4731
	111	31.57 , 32	31.65 , 28	31.59 , 41	31.58 , 50	31.5313
	040	31.94 , 17	31.98 , 29	31.90 , 17	31.90 , 50	31.9711
	131	39.07 , 32	39.08 , 30	39.08 , 37	39.06 , 47	39.3292
	002	-	-	45.52 , 40	45.46 , 43	45.4946
(c)	$I(111)/I(040)$	0.38	0.28	2.83	12.5	2.00
	$I(101)/I(040)$	0.15	0.06	1.19	6.25	1.40
	$I(002)/I(040)$	~0	~0	0.97	3.44	1.00
(d)	E_g [eV]	1.42	1.42	1.30	1.30	-
(e)	ρ [Ω cm]	692	62	172	59	-
	Hole density [cm^{-3}]	1.1×10^{16}	7.3×10^{15}	1.5×10^{16}	6.9×10^{15}	-
	μ_p [$cm^2V^{-1}s^{-1}$]	0.8	13.8	2.4	15.3	-

From the intensity ratios shown in Table 2.1c, the change in preferred crystal orientation from the (040) plane to the (111) plane is observed as the film thickness increases. Moreover, the intensities of the (101) and (002) planes significantly increase, while that of the (040) plane noticeably decreases. This result indicates that when the films grow thicker, the {010} layer planes switch from parallel to perpendicular to the substrate surface. This switching of crystal orientation with increasing film thickness agrees well with the observed grain size variations in the films deposited at 120 °C shown in Table 2.1b; the average grain size determined from (040) peaks is much smaller than those from other peaks since only during the initial growth does this crystallographic plane lie parallel to the substrate surface. The smaller grains in the initial film growth at 120 °C can be seen visually from the cross-sectional SEM of Figure 2.5a, as indicated in the boxes. At 200 °C, the thermal energy is high enough to merge these initially nucleated grains with the grains grown later, so that all the Bragg peaks show the same FWHM.

The observed switching of crystal orientation can be explained by considering the surface energies of SnS crystal planes. Since SnS is a layered compound with the layer plane perpendicular to the *b* crystallographic axis, the {010} planes have much lower surface energy than {100} and {001} planes at the surface boundary. When SnS starts to nucleate on the substrate surface, {010} planes would be preferred to align parallel to the substrate to minimize the surface energy. Once the film grows thicker, the surface areas (plane defects) are mainly from the grain boundaries within the film rather than from the top surface. Thus, the minimum surface energy is to have {010} planes parallel to the grain boundaries, which is perpendicular to the substrate surface due to the nature of the columnar structure in this case. In single crystals, the hole mobility along the layer direction is about 10 times higher than that in the perpendicular

direction.[60] Therefore, this preferred orientation of having layer planes perpendicular to the substrate is desirable in solar cells since the carrier transport occurs within the layer plane which has higher mobility and is also along the defect tolerant surfaces.

2.4.4 Film composition and purity

2.4.4.1 Phase purity

Mathew *et al.* reported traces of Sn_2S_3 and SnS_2 in the SnS films grown by pulsed electrodeposition that cannot be detected by XRD but can be observed by Raman spectroscopy.[21] To confirm the phase purity, Raman spectra were taken of the ALD SnS films grown at between 120 and 300 °C. Figure 2.7 shows the Raman peaks of ALD SnS detected at 68, 94, 162, 191, 219, and 288 cm^{-1}, all of which match well with those from single crystal SnS observed at 40, 49, 70, 85, 95, 164, 192, 218, and 290 cm^{-1}.[61] This result confirms that the films grown at 120-300 °C are pure SnS without any contamination from SnS_2 and Sn_2S_3, which have their strongest Raman peaks at around 312 and 307 cm^{-1}, respectively. Due to the insensitivity of XRD and Raman spectroscopy to amorphous phases, transmission electron microscopy (TEM) was used to look for an amorphous phase between crystallite grains. Figure 2.8 shows TEM micrograph and selected area electron diffraction (SAED) of a 25 nm-thick SnS film deposited at 120 ^{o}C. These results show that ALD SnS films do not contain significant amounts of amorphous phase despite being deposited at a relatively low temperature. The utilization of a Sn(II) precursor rather than a Sn(IV) precursor[23,40,43,44] broadens the narrow substrate temperature window reported previously and provides only pure SnS over a wider range of temperature.

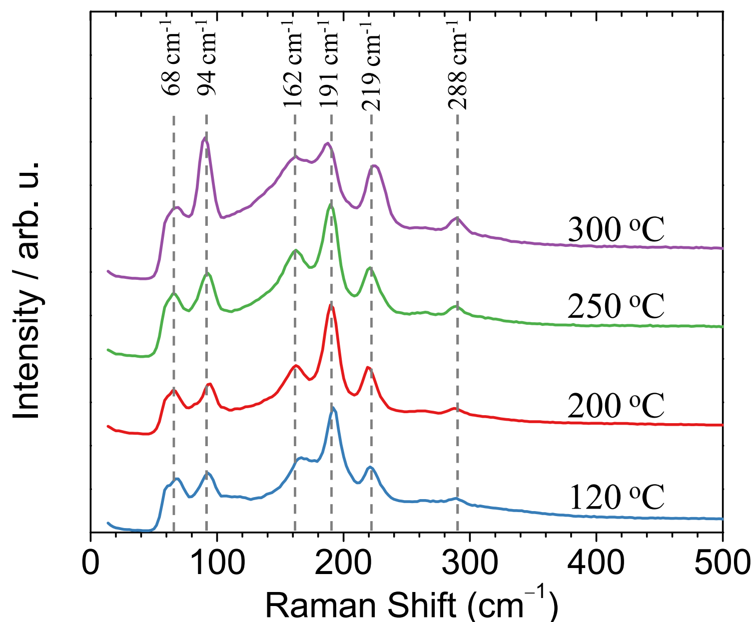

Figure 2.7: Raman spectra of ALD SnS films deposited between 120 and 300 °C, indicating pure Herzenbergite SnS phase.

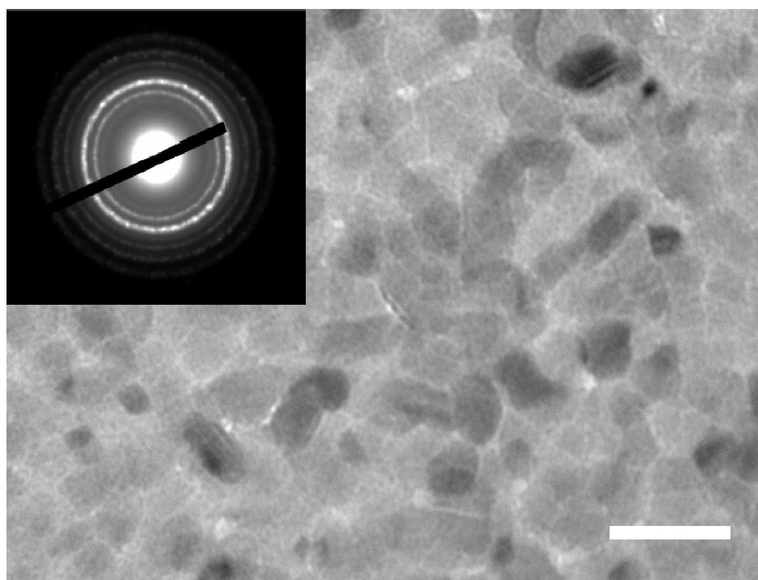

Figure 2.8: Plane-view TEM micrograph of a 25 nm-thick SnS film deposited at 120 °C. The inset is a SAED pattern indicating a polycrystalline structure of the film. The scale bar is 50 nm.

2.4.4.2 Stoichiometry

All the as-deposited films grown between 100 and 200 ^{o}C were measured to be stoichiometric SnS (Figure 2.9) to within the sensitivity limit of the RBS analysis (±1%). The atomic ratio of tin to sulfur deviates from 1.00 to 1.04 and 1.09 at the deposition temperature of 250 and 300 °C, respectively. This change in atomic ratio happens in the same temperature range as the decomposition of the tin precursor, above 250 °C. Reddy *et al.* reported a stoichiometric SnS obtained from thermal evaporation technique at the substrate temperature of 300 °C.[16] However, using the same deposition condition, stoichiometric SnS can be obtained only for films thicker than 1 µm; the atomic ratio of Sn to S increases almost linearly from 1.0 at 1.2 µm-thick to 1.1 at 100 nm-thick.[15] Such a thickness effect on film composition has not been observed in our ALD SnS films; all ALD SnS films deposited below 200 ^{o}C in the thickness range of 50-370 nm are stoichiometric SnS with tin to sulfur atomic ratio of 1.00 ± 0.01. This

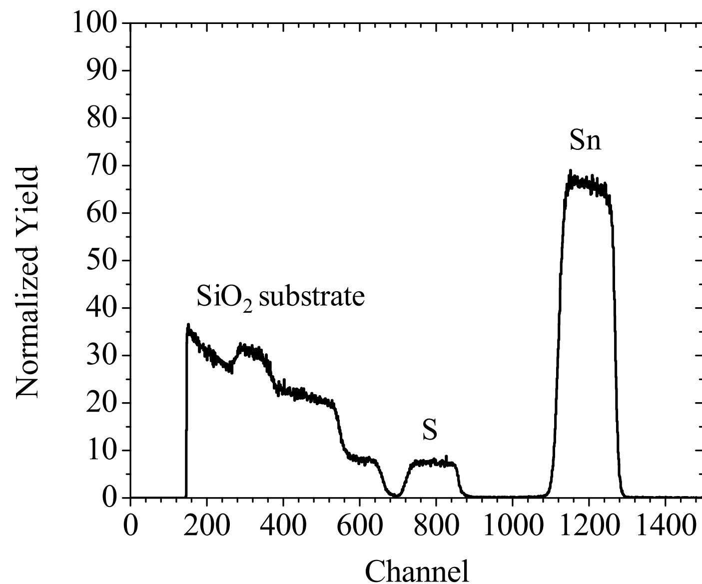

Figure 2.9: A typical RBS spectrum of ALD films deposited at between 100 and 200 °C, indicating stoichiometric SnS to within ±1%.

stoichiometric SnS is expected to provide a low density of native point defects and Sn^{2+} vacancies in the material. The density of the ALD film, calculated from atomic area density (by RBS) and film thickness (by SEM), is about 4.6 g cm^{-3}. This value is 88% of the bulk density of SnS (5.2 g cm^{-3}), which is relatively high for thin polycrystalline films.

2.4.4.3 Elemental purity

The incorporation of carbon is sometimes found in films deposited from a metal organic precursor due to incomplete dissociation of organic ligands from the metal center at low growth temperature or precursor decomposition at high growth temperature. Figure 2.10a shows a representative XPS spectrum of ALD SnS films deposited at 100-200 °C. Oxygen and carbon *1s* peaks were observed only at the surface of the SnS film due to ambient contamination. After Ar sputtering for 5 min, O*1s*, N*1s*, and C*1s* peaks were not detected. Time-of-flight secondary ion mass spectroscopy (TOF-SIMS) analyses of films deposited at 120 and 200 °C also did not

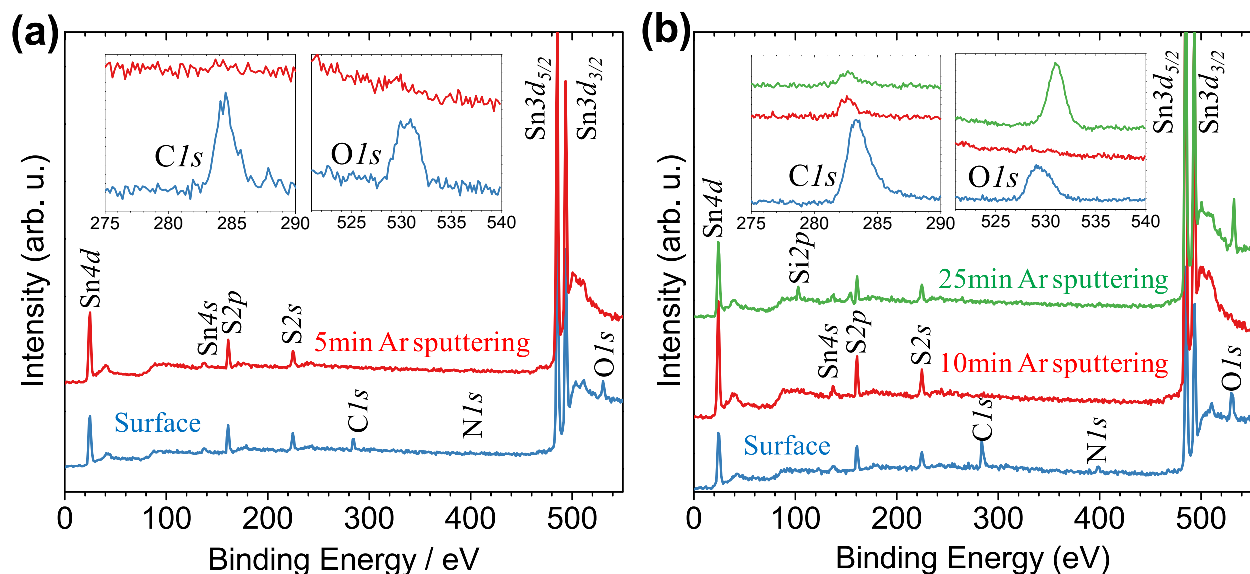

Figure 2.10: XPS depth-profiling of a typical ALD SnS film deposited between **(a)** 100-200 °C and **(b)** 250-300 °C.

detect any oxygen, nitrogen or carbon within the films. These results indicate that ALD SnS has high purity due to the clean reaction between $Sn(amd)_2$ and H_2S. However, for depositions above 250 °C, ~1-2% of carbon can be observed in the films. Figure 2.10b shows XPS depth profiling of ~94 nm-thick SnS film deposited at 250 °C detecting at the film surface, inside the SnS film (10min Ar sputtering), and at the interface between the film and a SiO_2 substrate (25 min Ar sputtering). Upon Ar sputtering, the O*1s* peak disappears inside the SnS film and reappears again at the film-substrate interface. In contrast, the C*1s* peak remains throughout the film up to the interface. The peak positions of C*1s* and O*1s* after Ar sputtering are shifted from those at the surface, which reveals that both carbon and oxygen detected after sputtering are not from atmospheric contamination. Consequently, SnS film grown above 250 °C is free of oxygen and nitrogen but has ~1-2% carbon incorporation into the film. This carbon contamination results from the decomposition of the tin precursor which is also indicated by the increase of the growth rate and non-stoichiometry of SnS film as mentioned earlier. In conclusion, ALD SnS films can be deposited at relatively low temperature in the range of 100-200 °C with precisely controlled thickness and the obtained films are phase-pure, stoichiometric SnS without any other elemental impurity.

2.4.5 Optical properties

The absorption coefficient (α) and the optical band gap (E_g) of the film were determined from the transmittance (T) and reflectance (R) measurements. The absorption coefficient was determined based on the following formula to minimize the interference effects in the absorption of the film:[62]

$$\alpha = \frac{1}{d} ln\left(\frac{1}{2}\left\{(1-R')(\frac{1-R}{T}) + \sqrt{\left[(1-R')^2\left(\frac{1-R}{T}\right)^2 + 4R'\right]}\right\}\right) \quad (2.1)$$

where d is film thickness, T is total transmittance, R is total reflectance, and R' is a single reflectance from the film-substrate interface. Due to an unknown refractive index of SnS film in the absorbing region, R' cannot be determined. However, a good estimation of α can be obtained from the following approximation;

$$\alpha \approx \frac{1}{d}\ln\left\{(1-R')(\frac{1-R}{T})\right\} \approx \frac{1}{d}\ln\left\{(\frac{1-R}{T})\right\} \quad (2.2)$$

This approximation is valid and converges to the correct value in the high absorption region, where $(1\text{-}R)/T >> 1$. The absorption coefficients of SnS films (Figure 2.11a) remain over 10^4 cm^{-1} in the infrared region above the band edge and over 10^5 cm^{-1} in the visible region. The absorption coefficients of the 330 nm-thick sample (blue diamonds) above 2.25 eV cannot be determined accurately since the transmittance T in this energy range becomes close to 0. With α = 5×10^4 cm^{-1}, just above the band gap, the thickness of the film required to absorb ~ 90% of the the optical band gap of the film as determined from the absorption coefficient using photons is only 0.5 μm. The strong optical absorption of SnS above the band edge is comparable to or higher than other well-developed absorber materials, as shown in Figure 2.12. $(\alpha \cdot hv)^n = A(hv - E_g \pm E_{ph})$, where A is a constant, n is the transition probability, E_g is the optical band gap of the film as determined from the absorption coefficient using $(\alpha \cdot hv)^n = A(hv - E_g \pm E_{ph})$, where A is a constant, n is the transition probability, E_g is the optical band gap, and E_{ph} is the phonon energy. For direct transitions (E_{ph} = 0), n = 2 for allowed and n = 2/3 for forbidden transitions. For indirect transitions, n = 1/2 for allowed and n = 1/3 for forbidden

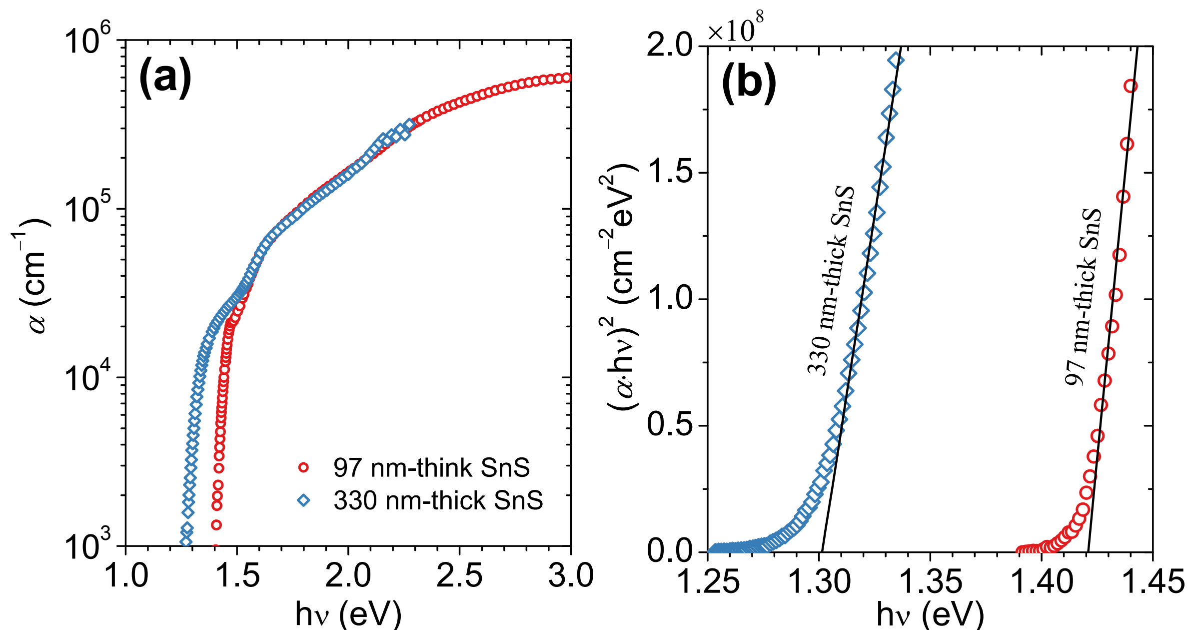

Figure 2.11: Optical properties of SnS films deposited at 200 °C at two different thicknesses. **(a)** absorption coefficient α and **(b)** a plot of $(\alpha \cdot h\nu)^2$ as a function of photon energy, indicating direct transition with the optical band gap E_g at x-interception.

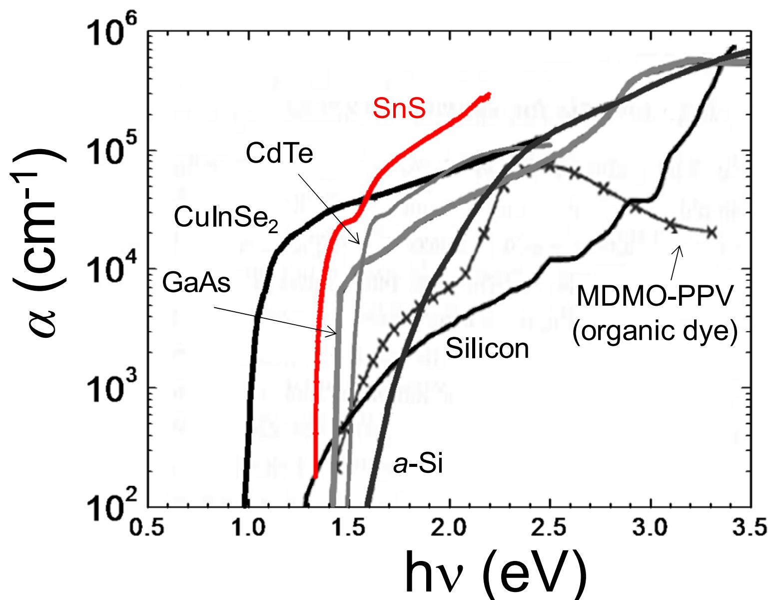

Figure 2.12: Absorption-coefficient of SnS (330 nm) compared to other absorber materials used in current technologies. [Adapted from Nelson, J., *The Physics of Solar Cells*. Imperial College Press: London, 2003.]

transitions. *α(λ)* near the band edge is best fitted to $n = 2$, which indicates a direct allowed transition for all the samples as illustrated in Figure 2.11b. The band gap of the films is determined from the plot of $(\alpha \cdot h\nu)^2$ versus photon energy by extrapolating to $\alpha \cdot h\nu = 0$. It is worthwhile to note that without taking the interference effect into account, the determined band gap in these particular samples can be shifted as far as ±0.3 eV.

The band gap of SnS deposited at 200 °C decreases from 1.42 to 1.30 eV when the film thickness increases from 97 to 330 nm. Based on these results, the optical band gap of SnS films appears to decrease with increasing film thickness. The dependence of the optical band gap of SnS on film thickness has been previously reported by Devika and Ristov and this phenomenon has been assigned to the effect of the degree of the film crystallinity.[15,45,63] In addition to the degree of crystallinity, the band gap shift can also stem from the change in the crystal orientation. In principle, layered structure compounds are highly anisotropic and thus can have different optical properties in different crystallographic orientations. HgI_2 film has been shown to switch its preferred crystal plane parallel to the substrate from (102) to (002) when the film thickness reaches ~1.45 μm while its optical band gap shifts from 1.94 to 2.25 eV for the directions perpendicular to the (102) and (002) planes, respectively.[64]

In single crystal SnS, the lowest allowed optical energy gaps along the *a* and *c* crystallographic axes are 1.60 and 1.34 eV respectively, as determined by electroreflectance and optical transmission.[65] The smallest energy gap is, however, reported to be an indirect transition at 1.07 eV.[66] Makinistian and Albanesi employed an *ab initio* density-functional theory with an FP-LAPW method to calculate the electronic band structure and the optical spectra of SnS. They

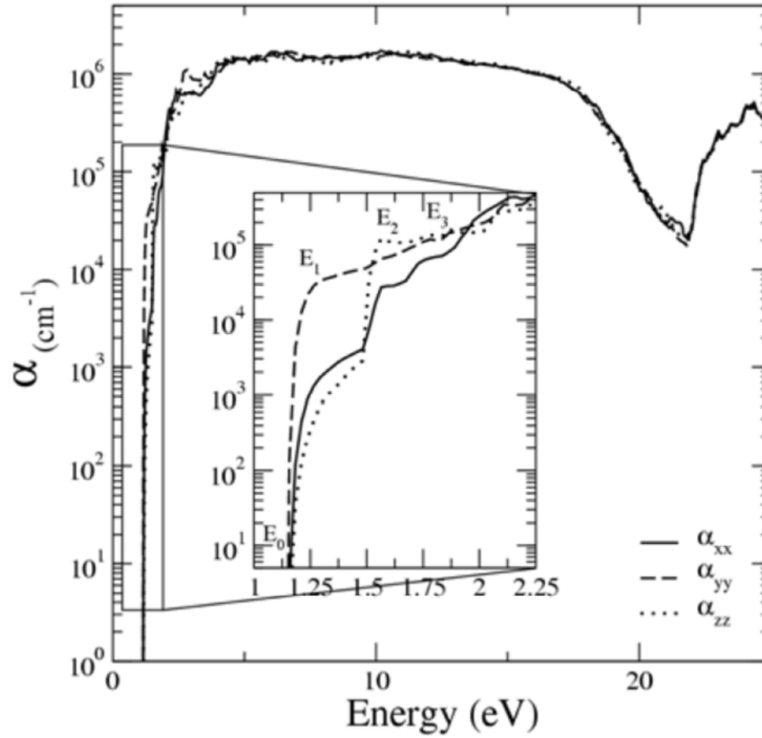

Figure 2.13: Calculated absorption coefficient of SnS along three principal crystallographic axes, as taken from Ref. [67]. Due to a different notation, α_{xx}, α_{yy}, and α_{zz} here correspond to the absorption in the directions through *b*, *c*, and *a* axes of SnS in this work, respectively.

reported that although SnS has an isotropic indirect energy band gap at 1.16 eV, the absorption coefficients along three principal crystallographic axes (Figure 2.13) are highly anisotropic;[67] the absorption coefficient along the *c* axis has a sharp increase from 10^1 to 10^4 cm^{-1} at 1.21 eV. In contrast, the absorption coefficient along the *a* and *b* axes are quite similar and they have one sharp increase from 10^1 to 10^3 cm^{-1} at 1.20 eV and another sudden rise from 10^3 to 10^5 cm^{-1} at 1.54 eV.

The smallest absorption coefficient that *T* and *R* measurements can detect from the films with thickness less than 500 nm is around 10^2 cm^{-1}. Below this α value, the absorption for a film with thickness below 500 nm is less than ~0.005 = $(1 - e^{-1E2\times 500E-7})$ and therefore reliable

measurement is difficult to achieve. Since the absorption coefficient close to the optical band gap E_g at 1.1-1.2 eV is below 10^2 cm^{-1},[66,67] it may not be detected from our samples with T and R measurements. Also, interference effects must be included to analyze optical data for these nearly transparent regions of the spectrum. The optical band gaps that are detected at absorption coefficients above 10^3 cm^{-1} are probably from other inter-band transitions, which are not the lowest energy transition. They are different depending on sample thickness, since these transitions at higher energy gaps depend on the direction of the crystallographic orientation which changes when the film grows thicker. The change in preferred crystal orientation from {010} to {111} planes can be correlated to the change in the optical energy gap of the film; the detected optical band gap of SnS film changes from 1.42 to 1.30 eV when most of the crystallite grains change (040) plane orientation from parallel to perpendicular to the substrate surface with increasing film thickness.

2.4.6 Electrical properties

Electrical properties of SnS films were determined by Hall measurement using the Van der Pauw method and are summarized in Table 2.1e. Resistivity of the films deposited below 200 °C is roughly in the range of 50-700 Ω cm and correlates strongly with the grain size, crystallinity and morphology of the films. Compared to the samples of the same average film thickness (~90-100 nm), SnS films show lower resistivity as the growth temperature increases. Interestingly, the resistivity of the films deposited at 200 °C does not change as the film thickness increases from 97 (sample **B**) to 330 nm (sample **D**). Normally, the resistivity decreases as the film gets thicker, due to less carrier scattering at the grain boundaries as the

grain size increases. However, SnS is a highly anisotropic material. As mentioned earlier, the hole mobility along the layer direction is about 10 times higher than that in the perpendicular direction in single crystals.[60] Thus, in addition to grain boundary scattering, the crystal orientation is also an important factor that contributes to the electrical properties of the films. From XRD, most of the (040) plane crystallite grains change orientation from parallel to perpendicular to the substrate surface with increasing film thickness. As a result of this crystal orientation change, the resistivity of the films deposited at 200 °C does not change significantly as the film thickness increases from 97 to 330 nm. In the case of the film deposited at 120 °C, the grain boundary scattering is expected to dominate the crystal orientation effect since the nucleation layer which favors (040) preferred orientation is also observed in the thicker film.

Hall measurement revealed that SnS films have p-type conductivity with hole concentrations between 1×10^{16} and 3×10^{16} cm^{-3} and hole mobilities in the range of 1-4 $cm^2V^{-1}s^{-1}$. These low carrier concentrations may arise from slight deviations from stoichiometry leading to native point defects such as Sn^{+2} vacancies. A low carrier concentration facilitates charge separation at the p-n junction in solar cells since the depletion width, covered by a built-in electric field, extends through most of the absorber layer.

Interestingly, in a Au/SnS/Au structure, the resistivity of a 370 nm-thick SnS film deposited at 120 °C (sample **C** in Table 2.1) measured in vertical direction through the film was 60 **Ω** cm, which is roughly three times lower than that in the lateral direction (176 **Ω**·cm). This anisotropic resistivity of ALD SnS mainly arises from the combination of columnar structure (grain boundaries) and preferred crystal orientation discussed earlier. At 200 °C, the Au substrate

has a significant effect on the growth of SnS, yielding grain sizes enlarged as much as 10 times compared to films grown on SiO_2 substrates. Therefore, SnS films deposited at 200 °C on Au substrates cannot be used for a similar estimate of the anisotropy of the mobility in different directions in the film.

2.5 Conclusions

Tin monosulfide thin films were deposited by ALD using the reaction of bis(*N*,*N'*-diisopropylacetamidinato)tin(II) and hydrogen sulfide at substrate temperatures between 100 and 200 °C. Minimum exposures of 1.5 Torr·s of tin precursor and 1.1 Torr·s of H_2S were required to saturate the surface reactions and obtain growth at 0.86-0.90 Å/cycle. The films are polycrystalline and crystallized in a pure single orthorhombic phase of SnS with a = 4.30 Å, b = 11.20 Å, and c = 3.99 Å. Neither SnS_2 nor Sn_2S_3 was detected by Raman spectroscopy or XRD. TEM analysis showed that the film contains a negligible amorphous phase despite the relatively low temperature deposition. All the films below 200 °C were measured to be stoichiometric SnS to within RBS sensitivity (±1%). No C, N, or O impurities were detected by XPS or TOF-SIMS. The films have a dense, polycrystalline columnar structure. The optical band gap of the films decreased from 1.42 to 1.30 eV when the preferred crystal orientation changed from (040) to (111) as the thickness of the films increased from 100 to 330 nm. Their optical absorption coefficients are over 10^4 cm^{-1} in the infrared above the band edge, and over 10^5 cm^{-1} in the visible region. The lateral resistivity of the films is between 50 and 700 Ω cm depending on film thickness and growth temperature. Hall measurements showed that the SnS films have p-type conductivity with hole concentrations between 1×10^{16} and 3×10^{16} cm^{-3} and hole mobility in the

range of 0.8-15 $cm^2V^{-1}s^{-1}$ in the plane of the films. In the direction through the film, the mobility and conductivity are roughly three times higher, because of the preferred orientation of the (040) layer planes perpendicular to the surface of thicker films and the columnar structure of the films. These suitable optical and electrical properties of ALD SnS films, coupled with inexpensive, non-toxic and earth-abundant constituent elements, make this material a promising candidate for an absorber layer in thin film solar cells.

Chapter 3

SnS/Zn(O,S) Heterojunction Solar Cells

3.1 Chapter Abstract

SnS is a promising Earth-abundant material for photovoltaic applications. Heterojunction solar cells were made by vapor deposition of *p*–type tin(II) sulfide, SnS, and *n*-type zinc oxysulfide, Zn(O,S), using a device structure of soda-lime glass/Mo/SnS/Zn(O,S)/ZnO/ITO. A record high efficiency was achieved for SnS-based thin film solar cells by varying the oxygen-to-sulfur ratio in Zn(O,S). Increasing the sulfur content in Zn(O,S) raises the conduction band offset between Zn(O,S) and SnS to an optimum slightly positive value. A record SnS/Zn(O,S) solar cell with a S/Zn ratio of 0.37 exhibits short circuit current density (J_{sc}), open circuit voltage (V_{oc}) and fill factor (FF) of 19.4 mA/cm^2, 0.244 V and 42.97%, respectively, as well as an NREL-certified total area power conversion efficiency of 2.04% and an uncertified active-area efficiency of 2.46%.

3.2 Introduction

The toxicity of Cd and the scarcity of Te, In, and Ga used in CdTe and $Cu(In,Ga)S_2$ (CIGS) thin film solar cells have motivated a search for alternative non-toxic, earth abundant and inexpensive materials.[7] Tin(II) sulfide (SnS) is among the ongoing investigated materials such as Cu_2O,[8] Cu_2S,[9] FeS_2,[10,11] $Cu_2ZnSn(S_xSe_{1-x})_4$,[12] and $ZnSnP_2$.[13] SnS has a suitable band gap (E_g ~ 1.1 - 1.5 eV),[14,15] strong optical absorption ($\alpha > 10^4$ cm^{-1}),[16] and proper carrier concentration ([*p*] ~ 10^{14} - 10^{17} cm^{-3}).[17] Recently, a record-high efficiency SnS solar cell of 1.95% (active area) was fabricated from *p-n* homojunction nanowires using boron and phosphorus as dopants.[68] In addition, SnS-based solar cells have been reported using different *n*-type partners such as ZnO,[69] CdS,[19,70] $Cd_{1-x}Zn_xS$,[71] SnS_2,[72] TiO_2,[46] and *a*-Si.[73] So far, the best SnS planar heterojunction device was fabricated with SnS/CdS, achieving a power conversion efficiency (η) of 1.3%.[19] The efficiencies achieved using heterojunctions of SnS with *n*-type materials other than CdS are extremely low (< 0.1%), mainly limited by low short-circuit current density (J_{sc} < 1.5 mA/cm^2). This poor J_{sc} is likely a result of bulk recombination in SnS because of defects, *e.g.*, grain boundaries, intrinsic point defects such as sulfur vacancies[17] and/or impurities that arise from the preparation methods used to make the films.

In addition to the quality of SnS, other main contributors to this poor efficiency are believed to be an unfavorable conduction band offset (CBO) and rapid carrier recombination at trap states near the interface between SnS and the *n*-type buffer layer. SnS/CdS forms a type-II heterojunction with the CBO ($\Delta E_c = \chi_{SnS} - \chi_{CdS}$, where χ is electron affinity) of −0.4 eV, which is an unfavorable band alignment for making efficient solar cells.[74] According to device

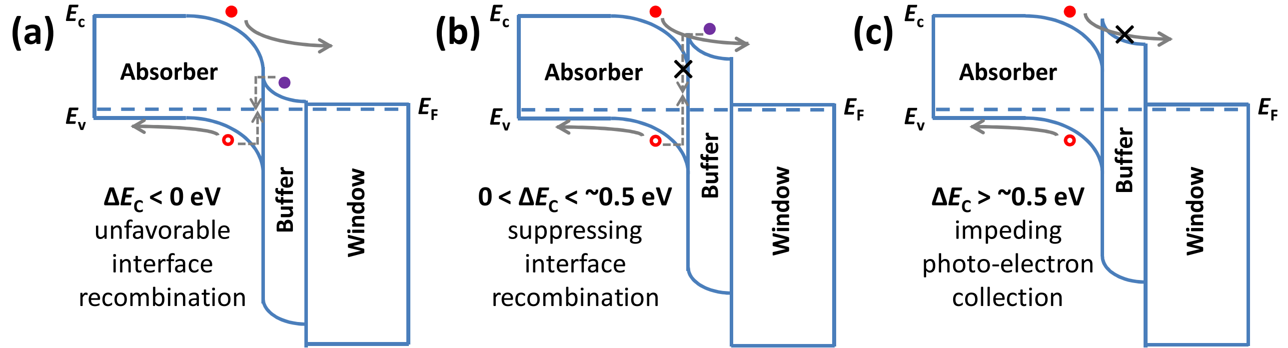

Figure 3.1: Energy band diagrams illustrating the effect of the conduction band offset (ΔE_c) between absorber layer and buffer layer on the electrical transport of the devices.

simulations, a large negative CBO (Figure 3.1a) gives rise to an increase in the interface recombination, while a large positive CBO greater than +0.5 eV (Figure 3.1c) creates a barrier in the conduction band that impedes the collection of photo-generated electrons.[75,76] Thus, a small positive CBO (Figure 3.1b) is desirable to reduce interface recombination without any loss in photo-current collection.[75,76] One of the approaches to adjusting the CBO is to vary the constituent elements in the semiconductor alloy buffer layer. For example, (Zn,Cd)S,[77] (Zn,Mg)O,[78] $(Zn,Sn)O_x$,[79] and Zn(O,S)[80] were used in an attempt to replace CdS in CIGS solar cells. This chapter presents a SnS device with a record high power conversion efficiency of 2.04% (total area) / 2.46% (active-area) using Zn(O,S) as an *n*-type buffer layer, and evaluates the effect of CBO on device performance.

3.3 Experiment Section

A device structure of soda-lime glass/Mo/SnS/Zn(O,S)/ZnO/ITO/Al, as shown in Figure 3.2, was used in this study. SnS thin films were deposited on Mo-coated (450 nm) soda-lime

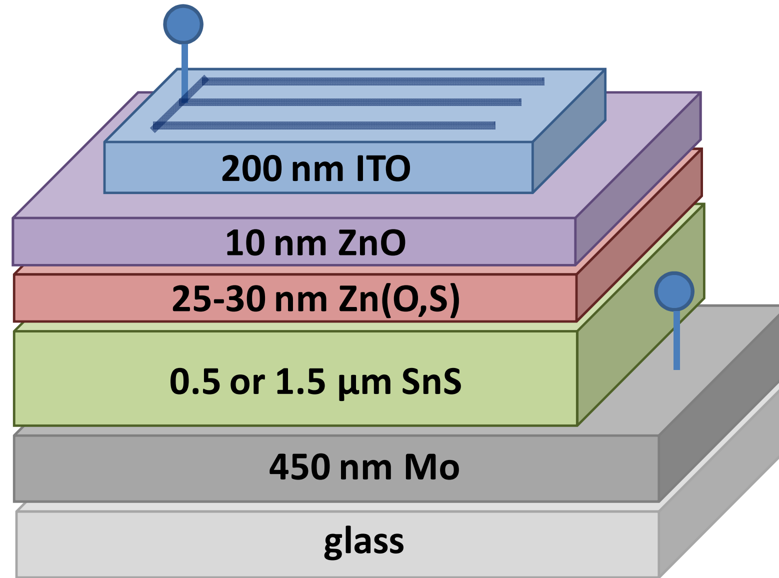

Figure 3.2: A SnS-based solar cell comprises soda-lime glass, molybdenum (200nm), pulsed-CVD SnS (0.5 or 1.5µm), ALD Zn(O,S) (25-30 nm), ALD ZnO (10 nm), sputtering ITO (200 nm), and aluminum grids (500 nm).

glass substrates using a pulsed chemical vapor deposition (pulsed-CVD) process from the reaction of bis(*N*,*N'*-diisopropylacetamidinato)tin(II) ($Sn(MeC(N\text{-}iPr)_2)_2$) and hydrogen sulfide ($H_2S$).[81] The sequence of one cycle of a pulsed-CVD is composed of (i) injection of a tin precursor vapor using N_2 assistance, (ii) injection of H_2S gas to mix and react with the tin precursor vapor trapped inside the deposition zone for 1 s, and (iii) evacuation of the gas mixture and by-products for 2 s. Compared to a conventional atomic layer deposition (ALD) of SnS,[81] the pulsed-CVD process omits some purge steps, thereby increasing the deposition rate by more than an order of magnitude at the cost of some non-uniformity in the film thickness along the length of the reactor. The purity and optoelectrical properties of the obtained SnS films are the same as those grown from the ALD process reported in Chapter 2.[81] The substrate temperature was set to 200 °C. The tin precursor source was kept at 95 °C. A gas mixture of 4% H_2S in N_2

(Airgas Inc.) was used as the source of sulfur. H_2S is a toxic, corrosive and flammable gas (lower flammable limit of 4%).[53] Thus, it should be handled with caution. An appropriate reactor design for H_2S compatibility can be found elsewhere.[54] The partial pressures of the tin precursor and H_2S after injecting into the deposition zone for each cycle are approximately 100 and 240 mTorr, respectively. Zn(O,S) (25-30 nm) and ZnO (10 nm) were prepared by ALD at 120 °C from the reaction of diethylzinc ($Zn(C_2H_5)_2$) (Sigma-Aldrich) with deionized water (H_2O) and hydrogen sulfide (H_2S). To ensure the quality of the interface, Zn(O,S) and ZnO layers were deposited immediately after the growth of SnS absorber layers without breaking vacuum. Indium tin oxide (ITO) (200 nm) was deposited at room temperature by RF magnetron sputtering through a shadow mask to define the cell area (0.031 or 0.71 cm^2). Additional electron-beam evaporated Al (500 nm) metal grids were used for the 0.71 cm^2 devices to further reduce the series resistance.

Device morphology was characterized using field-emission scanning electron microscopy (FESEM, Zeiss, Ultra-55). Rutherford backscattering spectrometry (RBS, Ionex 1.7 MV Tandetron) was performed to determine the elemental composition of Zn(O,S). The grain orientations of SnS films on Mo substrates were examined by X-ray diffraction (XRD, PANalytical X'Pert Pro) with Cu K_α radiation (λ = 1.542 Å) using θ-2θ scan. External quantum efficiency (EQE) measurements were made at room temperature, using a PV Measurements Model QEX7 tool. Transmittance (T) and reflectance (R) measurements were taken on a Hitachi U-4100 UV-Vis-NIR Spectrophotometer. Internal quantum efficiency (IQE) was calculated from IQE = EQE/(1−R). J-V measurements were made using a Keithley 2400 sourcemeter. The standard 1000 W/m^2 illumination was generated by a Newport Oriel 91194 solar simulator with a 1300 W Xe-lamp, an AM1.5G filter, and a Newport Oriel 68951 flux controller calibrated by an

NREL-certified Si reference cell equipped with a BK-7 window. SunsV_{oc} measurements were made using a Suns-V_{oc}-150 Illumination Voltage Tester from Sinton Consulting Inc.[82]

3.4 Results and discussion

To determine the optimum composition of the Zn(O,S) buffer layer for SnS, small devices with an active area of 0.031 cm^2 were fabricated using 500 nm-thick SnS with Zn(O,S) of different oxygen-to-sulfur ratios. By varying the cycle ratio of ZnO to ZnS during the ALD process, the elemental composition of Zn(O,S) can be adjusted.[83] ZnO:ZnS cycle ratios of 4:1, 5.5:1 (which alternates 5:1 and 6:1), 6:1, and 7:1, which correspond to Zn(O,S) of O:S:Zn ratios = 0.42:0.73:1, 0.56:0.58:1, 0.64:0.50:1, and 0.72:0.37:1, respectively, were used to fabricate the devices. Figure 3.3 shows current density-voltage (*J*-*V*) characteristics under dark and

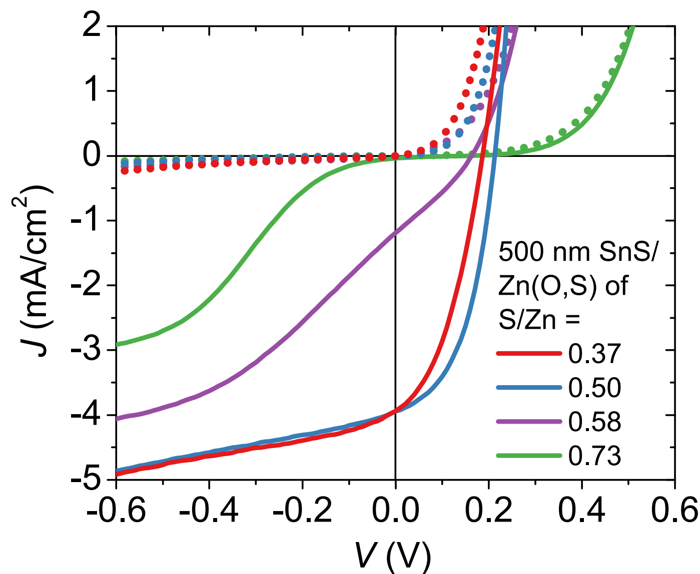

Figure 3.3: Current density-voltage characteristics of Mo/500 nm-SnS/Zn(O,S)/ZnO/ITO devices at different Zn(O,S) compositions (0.35 < S/Zn < 0.75) under dark (dotted line) and ~10 mW/cm^2 illumination (solid line).

illumination (~ 10 mW/cm^2) from a microscope halogen lamp (color temperature = 3300 K). This illumination condition, although different from the AM1.5 solar spectrum, is sufficient to test for junction character. Measured *J-V* characteristics suggest that for S/Zn > ~0.6, the SnS/Zn(O,S) junction exhibits type-I behavior with ΔE_c > +0.5 eV, *i.e.*, an energy barrier impedes photo-generated electron flow, resulting in a very low J_{sc}. For S/Zn ≤ ~0.5, the devices do not exhibit such a carrier collection problem and are thus believed to have ΔE_c < +0.5 eV. This trend corresponds well with the reported conduction band position of Zn(O,S), which is raised (lower χ) when the sulfur concentration in the film increases.[84]

After the optimum oxygen-to-sulfur ratios were determined for the Zn(O,S) buffer layer, larger-area devices (total area of 0.71 cm^2) were fabricated using 1.5 μm-thick SnS absorber layers with Zn(O,S) of S/Zn = 0.37 and 0.50. Figure 3.4 shows cross-sectional and plan-view SEM images of a device after Zn(O,S)/ZnO deposition. The SnS surface was covered uniformly by the buffer layer even at 25-30 nm thickness because of the conformal coating by ALD. The SnS film is columnar and composed of platelet-shaped grains. The observed cross-sectional grain size of SnS can be different (arrows in Figure 3.4a) depending on the cleaving direction with respect to these platelet grains. Figure 3.5a displays *J-V* characteristics of these devices under dark and AM1.5 illumination. For S/Zn = 0.50, the device shows J_{sc} = 9.1 mA/cm^2, V_{oc} = 0.28 V, FF = 29.9%, and η = 0.74%. Surprisingly, unlike the 500 nm-SnS device (Figure 3.1), the junction in this thicker SnS solar cell shows some signs of a large positive CBO including a dark/light *J-V* cross-over, higher diode voltage (*i.e.* V_{oc}), small FF, and low J_{sc}.[85] This CBO discrepancy may be because of a variation of the SnS surface condition for different film

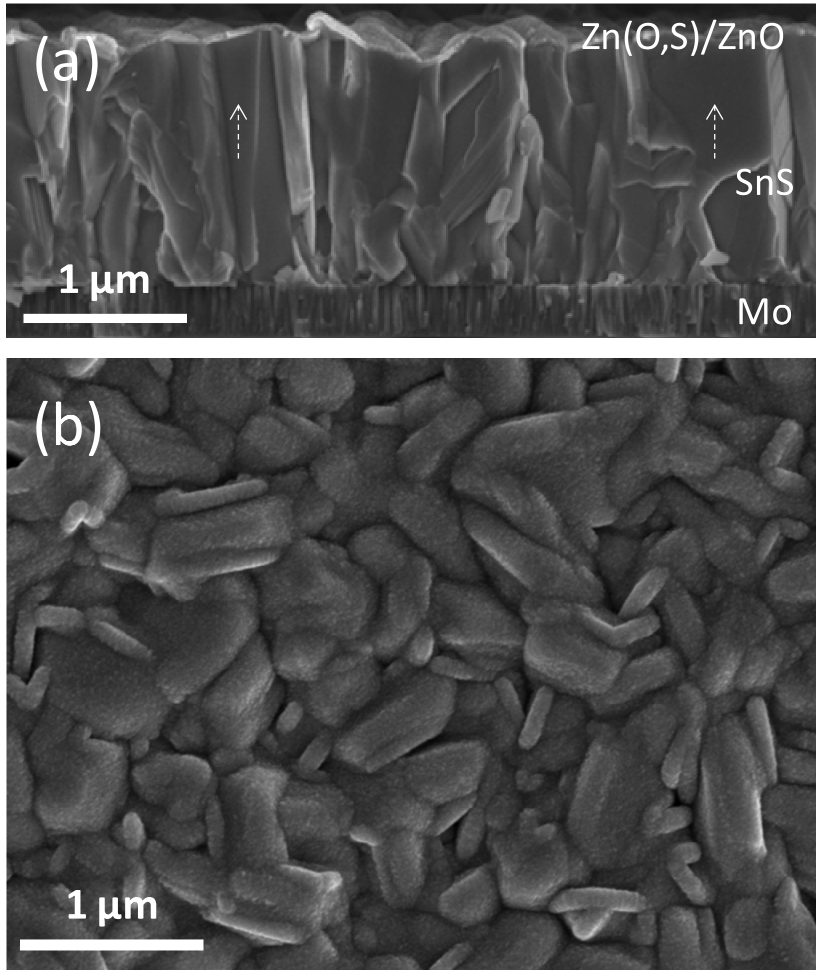

Figure 3.4: SEM images of **(a)** cross-sectional and **(b)** plan-view of Mo/SnS/Zn(O,S)/ZnO before top contact fabrication, showing a dense and conformal coverage of the Zn(O,S) and ZnO layers grown via ALD.

thicknesses. Figure 3.5b shows the XRD spectra of SnS films grown on Mo layers as a function of SnS film thickness. The preferred crystal orientation of SnS film clearly shifts from (111) to (101) when the film thickness increases from 0.3 to 1.5 µm. Because of the anisotropic nature of the layered SnS compound,[17,25] such a change in crystallographic orientation can strongly affect the surface conduction band position of SnS, and consequently its CBO with Zn(O,S).

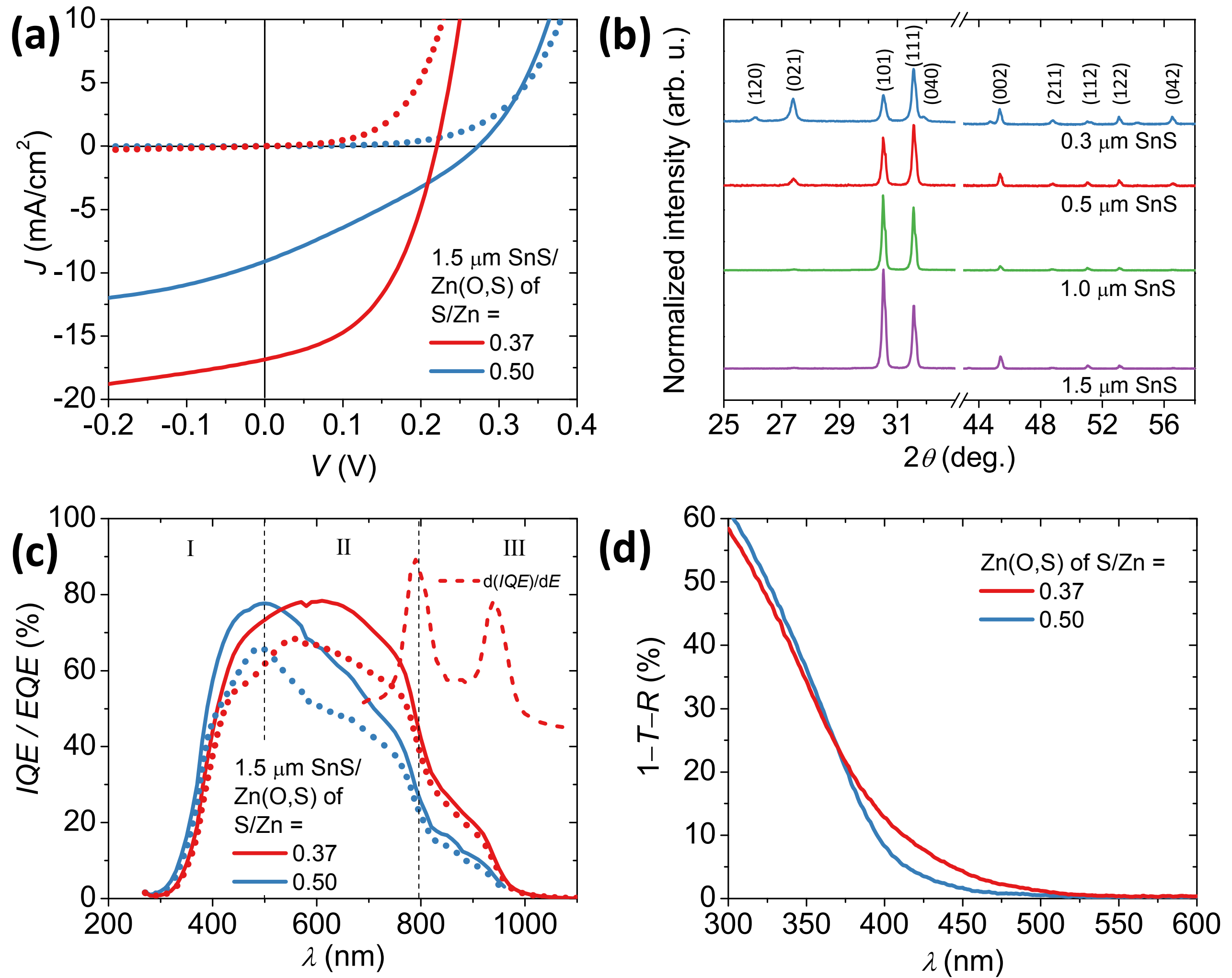

Figure 3.5: **(a)** *J-V* characteristic of 1.5 μm-thick SnS devices with Zn(O,S) of S/Zn = 0.37 and 0.50 under dark (dotted line) and approximately 1 sun illumination (solid line). **(b)** XRD spectra of SnS at the film thicknesses of 0.3, 0.5, 1.0, and 1.5 μm. The intensity was normalized by the (111) peak. **(c)** IQE (solid line) and EQE (dotted line) of the same devices. The peaks of the IQE derivatives in the S/Zn = 0.37 device correspond to the strong absorption edges of SnS at 1.32 and 1.55 eV. **(d)** Effective absorption (1−*T*−*R*) of 60 nm-thick Zn(O,S) of S/Zn = 0.37 and 0.50.

The internal quantum efficiency (IQE) (Figure 3.5c, solid line) of the 1.5 μm-thick SnS devices with Zn(O,S) of S/Zn = 0.37 and 0.50 shows three distinct regions of carrier collection. Above 800 nm, the IQE is relatively low and limited by the low absorption coefficient and bulk

recombination in SnS. The peaks of the IQE derivative (d(IQE)/dE) at 800 and 940 nm (1.55 and 1.32 eV, respectively) correspond well to the sharp rise in absorption coefficient of SnS (Figure 2.11a) at these two wavelengths. Between 500 and 800 nm, compared to the S/Zn = 0.37 device, a significant drop in IQE of the S/Zn = 0.50 device is observed because of the large positive CBO. Below 500 nm, the S/Zn = 0.50 composition provides a better carrier collection despite having the large conduction band energy barrier. This improved IQE at smaller wavelength can happen from photo-doping in the buffer layer, which results in a downward shift in the conduction band and thus reduces the CBO barrier.[86] In addition, Zn(O,S) of S/Zn = 0.50 also has a lower absorption tail as shown in Figure 3.5d and thus exhibits a better blue response.

The S/Zn = 0.37 device (Figure 3.5a) exhibits the best performance with J_{sc} = 16.8 mA/cm^2, V_{oc} = 0.22 V, FF = 47.7%, and η = 1.8%. The same device was characterized independently at the National Renewable Energy Laboratory (NREL), exhibiting an improved cell performance of J_{sc} = 19.4 mA/cm^2, V_{oc} = 0.244 V, FF = 42.97%, and η = 2.04%, as shown in Figure 3.6. We suspect that the discrepancy between NREL and our in-house measurements arises from lower illumination of our solar simulator. This device shows the highest recorded and independently verified efficiency of a planar SnS-based solar cell to date. This result demonstrates the flexibility of Zn(O,S) as an adjustable-CBO buffer layer for different surfaces or materials, which cannot be achieved in binary compounds (*e.g.,* CdS, ZnO, ZnS, TiO_2, or In_2S_3). The short-circuit current density of 19.4 mA/cm^2 is significantly higher than all previously reported SnS solar cells (9.6 mA/cm^2). This result is probably because of a better interface junction with Zn(O,S) and/or fewer defects in our SnS films, compared to other previously reported deposition

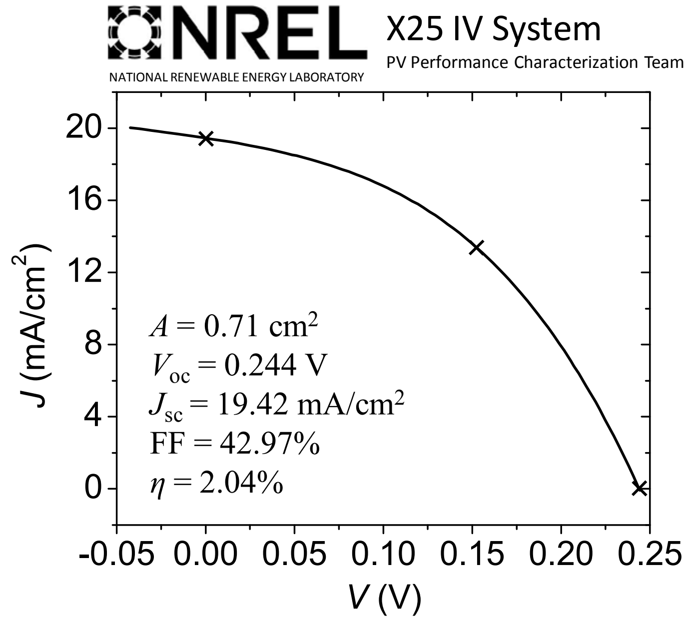

Figure 3.6: A champion SnS/Zn(O,S) solar cell with a record-high efficiency of 2.04% (total area), as certified by NREL.

techniques. The minority-carrier collection length (defined as depletion width + minority-carrier diffusion length) is roughly estimated from the IQE data of S/Zn = 0.37 device fitted with a combined space charge and minority carrier diffusion length collection model

$$\text{IQE} \cong 1 - [\exp(-\alpha \times W)]/[\alpha \times L + 1] \tag{3.1}$$

where α is the optical absorption coefficient, L is the minority-carrier diffusion length and W is the width of the depletion region, primarily used for absorbers such as CIGS and CdTe.[87,88] This approximation assumes that all carriers generated in the space-charge region are collected without recombination loss and those generated in the neutral bulk diffuse to the depletion edge.[87,88] Nonetheless, the maximum IQE in the SnS device does not reach 100%, indicating some loss in the space charge region or at the junction interface. To the first approximation, IQE was modeled by normalizing it to the maximum IQE of the device. The fit (Fig 3.7) suggests a

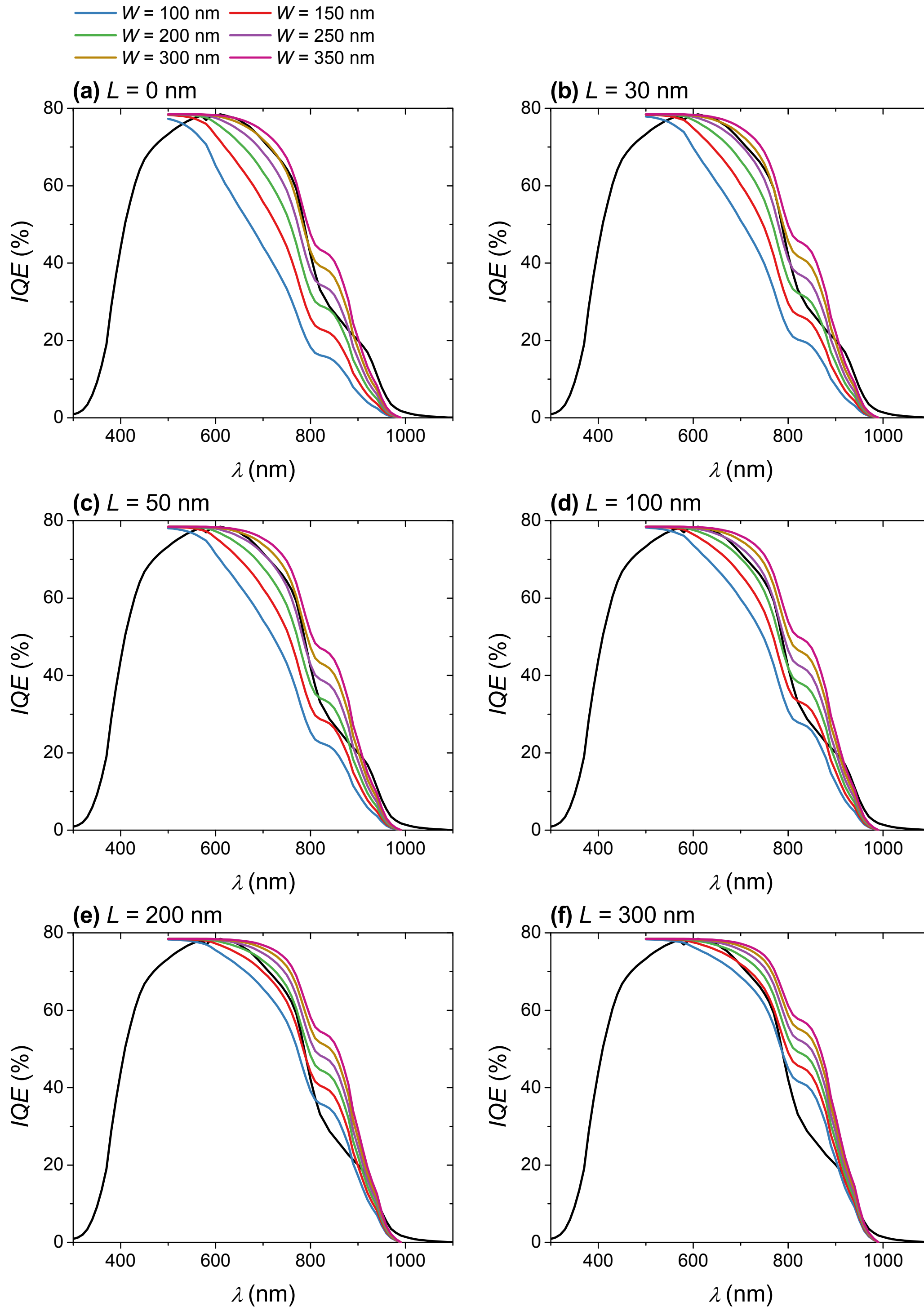

Figure 3.7: A modeling showing the effect of the minority carrier diffusion length (*L*) and the width of the space charge region (*W*) on the IQE, compared to the observed IQE of SnS/Zn(O,S) of S/Zn = 0.37.

minority carrier collection length range of 0.2-0.4 μm. For further improvement, a heat treatment of SnS may be required to increase the grain size and reduce defects in the material.

It is worthwhile to note that additional improvements of FF can be made on current devices by optimizing the device structure alone; the Al metal grid used in these devices was too thin (500 nm), and the series resistance (estimated to be 6.0 Ω cm^2 from fitted *J-V* curves) notably reduced the FF of the device. Using $SunsV_{oc}$,[82,89] the FF without the effect of series resistance is estimated to be 60%. This improvement in FF alone would yield a device with a pseudo-efficiency of 2.9%. In addition, the metal contact grid also covered 17% of the total cell area and created a significant shadowing loss. Adjusting the NREL-certified efficiency for this shadowing loss, the active-area efficiency is estimated to be 2.46%. The addition of an antireflection coating should help reduce the reflectance loss (~15% from reflectance measurements).

3.5 Conclusions

A SnS-based device (total area of 0.71 cm^2) comprising an *n*-type Zn(O,S) buffer layer achieved an NREL-certified full area solar cell efficiency of 2.04%, and an uncertified active area efficiency of 2.46%. The *p*-type SnS absorber layer was deposited via pulsed-CVD, followed by an ALD of the buffer layer without breaking vacuum. The full device structure is soda-lime glass/Mo/SnS/Zn(O,S)/ZnO/ITO/Al. The optimum oxygen-to-sulfur ratio was found to vary depending on the absorber layer thickness (*i.e.*, SnS preferred grain orientation), between S/Zn = 0.50 and 0.37 for 500 nm and 1.5 μm, respectively. The versatility of Zn(O,S) for CBO

tuning was demonstrated, which could be utilized for a systematic study in other absorber materials as well. The fundamental limit of the current device is a relatively small minority-carrier diffusion length in SnS. We expect that efficiencies can be further improved by optimizing contact geometry (shading losses, series resistance), adding an antireflection coating, improving bulk minority-carrier diffusion length, reducing absorber thickness, and eliminating edge shunting; efficiencies can be improved by an order of magnitude or more, considering the Shockley-Queisser efficiency limit for SnS of 32%.

3.6 Acknowledgements

Several people contributed to the work in this chapter. The author developed, fabricated and characterized the devices as well as analyzed and interpreted the data. Katy Hartman characterized the devices and analyzed and interpreted the data. Sang Bok Kim synthesized the tin(II) precursor. Roy Gordon and Tonio Buonassisi supervised the research and guided the manuscript preparation. I acknowledge Sarah Kurtz and Paul Ciszek along with the NREL cell measurement team for their assistance with certified cell testing. This work was supported by the U.S. National Science Foundation under NSF Award No. CBET-1032955, the U.S. Department of Energy SunShot Initiative under Contract No. DE-EE0005329, and by Saint Gobain S. A. which also supplied Mo-coated glass slides.

Chapter 4

Antimony-Doped SnS Thin Films

4.1 Chapter abstract

Thin film solar cells made from earth-abundant, inexpensive and non-toxic materials are needed to replace the current technologies whose widespread use is limited by their use of scarce, costly and toxic elements. Tin monosulfide (SnS) is a promising candidate for making absorber layers in scalable, inexpensive and non-toxic solar cells. SnS has always been observed to be a *p*-type semiconductor. Doping SnS to form an *n*-type semiconductor would permit the construction of solar cells with *p-n* homojunctions. This paper reports doping SnS films with antimony, a potential *n*-type dopant. Small amounts of antimony (~1%) were found to greatly

increase the electrical resistance of the SnS. The resulting intrinsic SnS(Sb) films could be used for the insulating layer in a *p-i-n* design for solar cells. Higher concentrations (~5%) of antimony did not convert the SnS(Sb) to low resistivity *n*-type conductivity, but instead the films retain such a high resistance that the conductivity type could not be determined. Extended x-ray absorption fine structure analysis reveals that the highly doped films contain precipitates of a secondary phase that has chemical bonds characteristic of metallic antimony, rather than the antimony-sulfur bonds found in films with lower concentrations of antimony.

4.2 Introduction

In the past few decades, tin(II) sulfide (SnS) has gained much attention as a possible alternative absorber material for the next generation of thin film solar cells to replace the current best developed technology based on $Cu(In,Ga)Se_2$ and CdTe, which involve toxic Cd and the rare elements In, Ga, and Te. In addition to low toxicity, low cost and the natural abundance of its constituent elements, SnS has a high optical absorption (α > 10^4 cm^{-1}) above the direct absorption edge at 1.3-1.5 eV.[21,81] It has native *p*-type conduction due to the small enthalpy of the formation of tin vacancies, which generate shallow acceptors.[17] SnS-based heterojunction solar cells have been reported using different *n*-type partners such as ZnO,[69] CdS,[19] $Cd_{1-x}Zn_xS$,[71] SnS_2,[72] TiO_2,[46] and *a*-Si.[73] The power conversion efficiencies (η) achieved so far on these planar heterojunction devices are still rather low (< 1.3%).[19] Some of the main contributors to this poor efficiency could be an unfavorable band offset and rapid carrier recombination at trap states near the interface between SnS and the *n*-type buffer layers.[74] In this aspect, a homojunction might

provide a better device performance, provided that *n*-type SnS can be produced. In addition to the homojunction approach, improved SnS-based solar cells might have a *p*-*i*(SnS)-*n* structure, similar to a strategy proposed by Sites *et al*. for CdTe.[90] This approach requires SnS to have a low carrier concentration on the order of 10^{13} cm^{-3}, which is lower than the typical undoped SnS values of 10^{15}-10^{18} cm^{-3}.[17,19,25,81] Therefore, the ability to control the carrier concentration and conduction type of SnS could improve SnS-based thin film solar cells and, in general, could broaden the utility of SnS as an optoelectronic semiconductor outside the field of photovoltaics.

SnS can be doped by Ag[25,91] and Cu[92] to increase its hole concentration to around 10^{19} cm^{-3}. Dussan *et al.* attempted to use Bi to substitute Sn in SnS to provide *n*-type conduction, but the material remains *p*-type below a 50% Bi concentration.[93] Sajeesh *et al.* reported *n*-type SnS thin films obtained by chemical spray pyrolysis, but this result is probably due to a significant *n*-type Sn_2S_3 impurity phase in the films.[35] One promising *n*-type substitution dopant is antimony(III), Sb^{3+}, due to the similarity of its ionic radius to Sn^{2+}. Albers *et al.* reported the use of Sb as a dopant that lowers the hole concentration of SnS to be less than 10^{14} cm^{-3}.[25] Nonetheless, the specific Sb concentration and detailed studies of its effect on the electrical properties of SnS were not reported. By increasing the Sb concentration further, it might be possible to convert SnS to an *n*-type semiconductor. Here, we report the preparation of Sb-doped SnS thin films, SnS(Sb), from the reaction of bis(*N*,*N'*-diisopropylacetamidinato)tin(II) [$Sn(MeC(N\text{-}iPr)_2)_2$] and tris(dimethylamido)-antimony(III) [$Sb(NMe_2)_3$] with hydrogen sulfide (H_2S). We identify the dopant chemical state, and report the effect of Sb dopant concentration on the crystal structure and electrical properties of the material.

4.3 Experiment section

Sb-doped SnS thin film. Pure, stoichiometric, single phase SnS thin films can be obtained by ALD from the reaction of bis(*N*,*N'*-diisopropylacetamidinato)-tin(II) [Sn(MeC(N-*i*Pr)$_2$)$_2$, referred to here as Sn(amd)$_2$] and hydrogen sulfide (H_2S), as shown in chapter 2.[81] Rather than using ALD as previously reported,[81] SnS thin films were deposited using a modified chemical vapor deposition (CVD) process, referred here as a pulsed-CVD, to speed up the deposit rate to ~15 times higher than that of ALD. The sequence of one cycle of a pulsed-CVD is composed of *(i)* injection of Sn(amd)$_2$ vapor using N_2 assistance, *(ii)* injection of H_2S gas to mix and react with the Sn(amd)$_2$ vapor trapped inside the deposition zone, and *(iii)* evacuation of the gas mixture and by-products. Unlike conventional ALD, there is no purging of excess Sn(amd)$_2$ before H_2S injection, thereby increasing the deposition rate at the cost of some non-uniformity in the film thickness along the length of the reactor. The substrate temperature was set to 200 °C. The tin precursor source was kept at 95 °C. A gas mixture of 4% H_2S in N_2 (Airgas Inc.) was used as the source of sulfur. An appropriate reactor design for H_2S compatibility can be found elsewhere.[54] The partial pressures of Sn(amd)$_2$ and H_2S after injection into the deposition zone for each pulsed-CVD cycle are approximately 100 mTorr and 240 mTorr, respectively.

Sb_2S_3 thin films can be prepared from ALD using the reaction of tris(dimethylamido)antimony(III) [Sb(NMe$_2$)$_3$] (Sigma-Aldrich) and hydrogen sulfide (H_2S).[94] The stop-flow ALD mode[55,56] was used for the deposition. The antimony source was kept at room temperature (25 °C). The total exposure of Sb(NMe$_2$)$_3$ and H_2S for each ALD cycle were approximately 0.7 and 1.1 Torr·s, respectively. Sb-doped SnS thin films were deposited by

inserting cycles of ALD Sb_2S_3 into the deposition of SnS. By varying the ratio between the numbers of Sb_2S_3 and SnS cycles, controlled concentrations of Sb^{3+} in SnS can be obtained. For example, a 1% cycle ratio film, SnS(1% Sb) was prepared by alternating between 99 cycles of SnS and 1 cycle of Sb_2S_3. Three samples were deposited using 1%, 2%, and 5% Sb cycles to determine the effect of Sb concentration on the crystal structure and electrical properties of the films.

Material characterization. Film morphology was characterized using field-emission scanning electron microscopy (FESEM, Zeiss, Ultra-55). The film thickness was determined from cross-sectional SEM. The elemental composition of the films was determined by Rutherford backscattering spectroscopy (RBS, Ionex 1.7 MV Tandetron) and time-of-flight secondary ion mass spectroscopy (TOF-SIMS). X-ray photoelectron spectroscopy (XPS, Surface Science, SSX-100) was used to detect possible carbon, nitrogen and oxygen contamination in the films. The crystal structures of SnS and Sb-doped SnS thin films were examined by x-ray diffraction (XRD, PANalytical X'Pert Pro) with Cu Kα radiation (λ = 1.542 Å) using θ-2θ scan. The lattice parameters were calculated from a least square fitting to the position of the Bragg peaks determined by Gaussian fit. Electrical properties of the films were characterized by Hall measurement (MMR technologies K2500) using the Van der Pauw method at 300 K. Synchrotron-based extended X-ray absorption fine structure (EXAFS) was used to study the local atomic environment of the antimony dopant. Synchrotron measurements were conducted at beamline 20-BM at the Advanced Photon Source of the Argonne National Laboratory.[95]

4.4 Results and discussion

4.4.1 SnS(Sb) film properties

The obtained SnS and Sb-doped SnS films appeared smooth, pin-hole free and adhered well to the substrate (a-SiO_2). Figure 4.1 shows the surface morphology of an undoped SnS film and a SnS(5% Sb) film grown by pulsed-CVD at 200 °C, as observed by SEM. Because of the low level of doping, the surface morphology of undoped SnS and all of the Sb-doped SnS samples are not significantly different. The film thicknesses of all the samples are approximately 500 nm, as determined from cross-sectional SEM. The chemical composition of the undoped SnS film was measured using RBS to be stoichiometric SnS to within the detection limit (±1%). As in ALD SnS[81] and ALD Sb_2S_3,[94] XPS does not detect any carbon or nitrogen contamination in the Sb-doped SnS films deposited at this particular temperature.

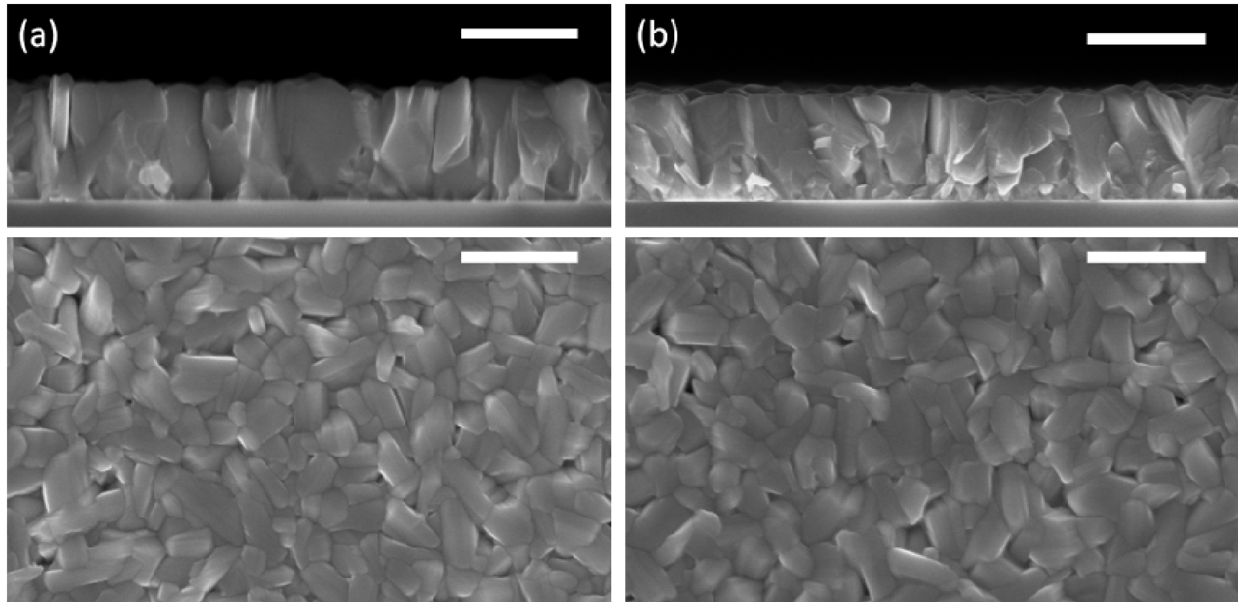

Figure 4.1: Cross-sectional and plan-viewed SEM images of **(a)** an undoped SnS film and **(b)** a SnS(5% Sb) film. The scale bar is 500 nm.

The atomic concentration of Sb in SnS was estimated by TOF-SIMS (Figure 4.2a) from the average intensity of Sb^+ and Sn^+ using a Cs^+ sputter source. If the efficiencies of generating Sb^+ and Sn^+ ions are assumed to be the same, then the Sb concentrations in SnS(1% Sb), SnS(2%

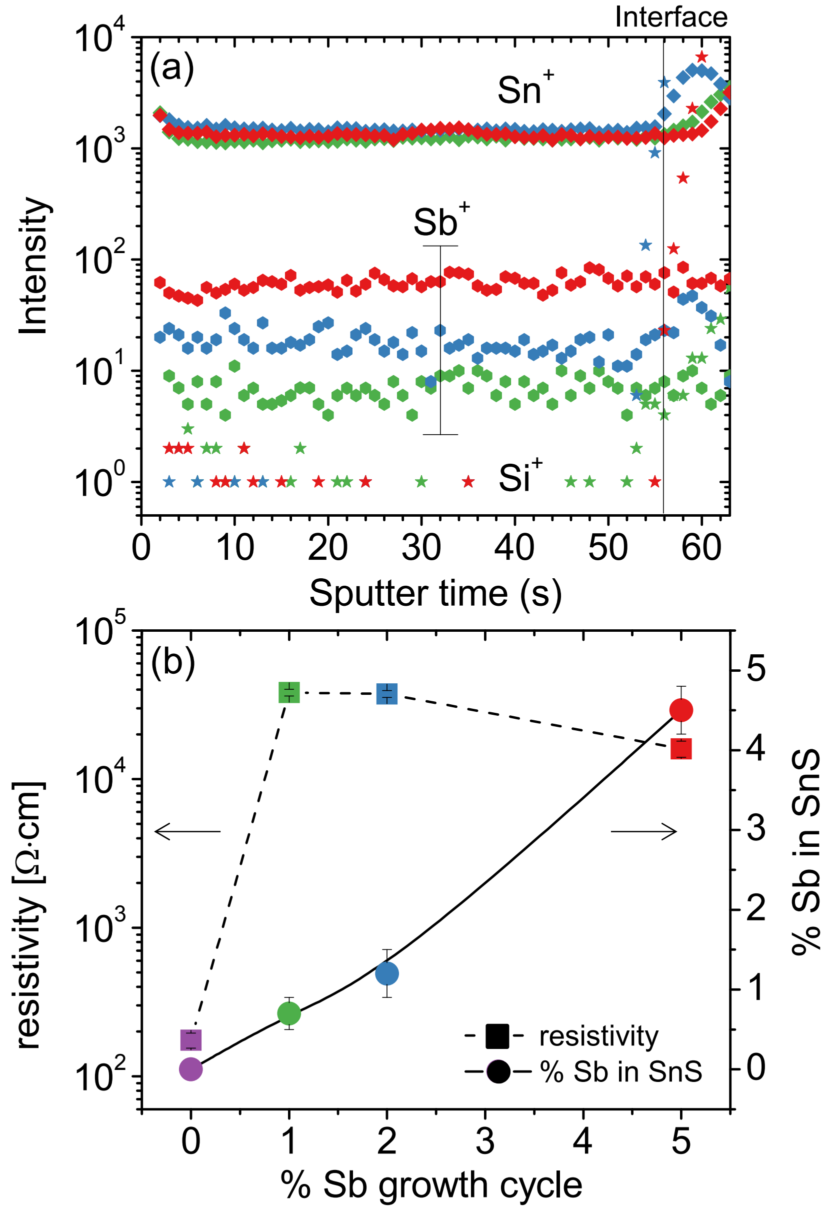

Figure 4.2: **(a)** TOF-SIMS of Sb-doped SnS films at 1%, 2%, and 5% Sb growth cycle. **(b)** Film resistivity and Sb concentration in SnS determined from TOF-SIMS as a function of the % Sb growth cycle.

Sb), and SnS(5% Sb) are determined to be 0.7 ± 0.2%, 1.2 ± 0.3%, and 4.5 ± 0.3%, respectively. Because we lack absolute concentration standards for SIMS analysis of dilute Sb in Sn, these concentrations could be in error by a constant calibration factor. As well, there is a chemical similarity between tin and antimony metals, so it is expected that the calibration factor should not deviate significantly from unity.

From Figure 4.2b, a slight deviation from linearity between the Sb concentration and Sb growth cycle percentage was observed in the SnS(5% Sb) sample. If the reactivity of the Sb(III) precursor and H_2S was identical on SnS and SnS(x% Sb) surfaces, then the atomic concentrations of Sb would be linearly proportional to their respective cycle percentages. However, the reactivities and chemisorptions on different surfaces, in general, are not the same. Thus, the actual Sb concentrations may not be exactly proportional to the cycle ratios, as observed in this case. This phenomenon was also observed in other doping systems, such as Al doped into ZnO,[96] TiO_2,[97] and SnO_2.[98]

Figure 4.3a shows the x-ray diffraction (XRD) patterns of SnS and Sb-doped SnS films, which correspond to the orthorhombic structure of Herzenbergite SnS (PDF No. 00-039-0354, a = 4.3291 Å , b = 11.1923 Å , c = 3.9838 Å). Other impurity phases (*i.e.*, Sn_2S_3 and SnS_2) were not detected in the deposited films. At 4.5% Sb-concentration, one Bragg peak at $2\theta = 28.7°$ was observed, but this peak does not belong to the known SnS or Sb_2S_3 phases. The peak could be assigned to the (040) plane of Valentinite Sb_2O_3 (PDF No. 01-072-2738) or the (012) plane of rhombohedral Sb (PDF No. 00-035-0732). However, depth profiling XPS reveals no oxygen contamination in this sample. Thus, this Bragg peak is most likely due to Sb; presumably, the

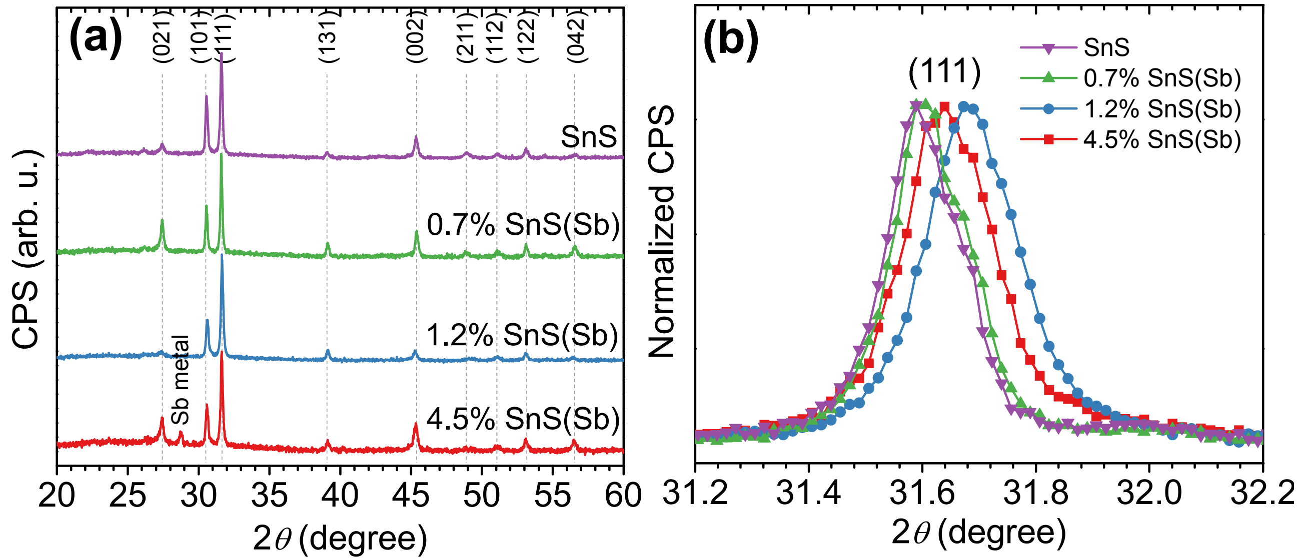

Figure 4.3: **(a)** XRD spectra of SnS and 0.7%, 1.2%, and 4.5% Sb-doped SnS. **(b)** An expansion around (111) lattice plane showing changes in lattice constants after Sb-doping.

concentration of Sb in this sample exceeded the solid solubility at the deposition temperature (or upon cooling); the resulting supersaturation was relieved via precipitation of a secondary phase. Figure 4.3b presents the XRD in the region near the (111) lattice plane. Since Bragg angle θ is inversely proportional to the lattice spacing d, which for (111) plane is equal to $[abc][(ab)^2+(bc)^2+(ac)^2]^{-1/2}$ where a, b, and c are lattice constants, the shift of the (111) peak position to the higher θ value indicates the crystal lattice shrinkage after Sb-doping. This unit cell volume decreases with an increasing Sb concentration from 0.7% to 1.2% probably due to substitution of smaller Sb^{3+} for Sn^{2+}, but increases less with higher (4.5%) doping because of the precipitation of the secondary phase, as we shall see by correlating these results with EXAFS.

Table 4.1 shows some electrical properties of SnS and Sb-doped SnS thin films at 300 K. The undoped SnS thin film shows resistivity of 175 Ω cm, hole concentration of 4.4×10^{15} cm^{-3},

Table 4.1: Summary of Sb concentrations, lattice constants and electrical properties of undoped and Sb-doped SnS films.

sample	cycle ratio Sn:Sb	%Sb in SnS (SIMS)	lattice constant (Å)			resistivity (Ω cm)	carrier density (cm^{-3})	mobility (cm^2/Vs)
			a	b	c			
SnS	1:0	0	4.30 ± 0.01	11.19 ± 0.02	3.99 ± 0.01	175	$+4.4\times10^{15}$	8
SnS(1% Sb)	99:1	0.7 ± 0.2	4.30 ± 0.01	11.19 ± 0.02	3.99 ± 0.01	3.82×10^4	below measurement sensitivity	
SnS(2% Sb)	49:1	1.2 ± 0.3	4.27 ± 0.01	11.17 ± 0.02	3.99 ± 0.01	3.74×10^4		
SnS(5% Sb)	19:1	4.5 ± 0.3	4.28 ± 0.01	11.19 ± 0.02	3.99 ± 0.01	1.60×10^4		

and mobility of 8 $cm^2V^{-1}s^{-1}$. The addition of small amounts of Sb, even at 0.7% concentration, effectively produces an insulating film with resistivity increased to 3.82×10^4 Ω cm, more than two orders of magnitude higher than the undoped film. Upon increasing Sb concentration up to 1.2%, the resistivity of Sb-doped SnS film remains roughly the same, 3.74×10^4 Ω cm. However, the film resistivity drops by half to 1.60×10^4 Ω cm when the Sb concentration increases up to 4.5%. Unfortunately, the carrier concentration and conductivity type of the Sb-doped SnS films cannot be measured from the current Hall setup because of their high resistivities.

4.4.2 EXAFS measurements on SnS(Sb)

To clarify the mechanism behind the anomalous rise and fall of SnS film resistivity with increasing Sb doping concentration, we performed Extended X-ray Absorption Fine Structure

(EXAFS) measurements at the Sb edge. The EXAFS technique is sensitive to the local atomic environment surrounding the dopant atoms, elucidating the chemical state of the dopant atoms (*e.g.*, substitutional, interstitial or second-phase particle). EXAFS was performed at the Sb-K_α x-ray absorption edge on the 1.2% SnS(Sb) film, the 4.5% SnS(Sb) film, the Sb_2S_3 film, and an Sb metal reference standard. We also performed EXAFS on the 0.7% SnS(Sb) film, but the signal was too weak to obtain a high-quality EXAFS spectrum. Data were analyzed using standard EXAFS analysis procedures[99] to obtain the Fourier transforms of the EXAFS spectra shown in Figure 4.4. All spectra were k-weighted by 1, and the transform ranges for each of the spectra were 3.15-9, 3-10.6, 3.3-12.2, and 2.75-15 $Å^{-1}$, respectively. In Figure 4.4, the peak at 2 Å of the 1.2% SnS(Sb) Fourier transformed EXAFS spectrum matches well with that of the Sb_2S_3 spectrum. In Sb_2S_3, this peak is due to the sulfur nearest neighbors of antimony, suggesting that the antimony in the 1.2% SnS(Sb) sample may be incorporated into the film in a sulfur environment. In contrast, the Fourier transformed EXAFS spectrum of the 4.5% SnS(Sb) shows close resemblance to that of an Sb metal, implying that the antimony in the 4.5% SnS(Sb) may be present in an antimony environment.

To elucidate the precise chemical states of Sb dopants in SnS films, EXAFS spectra were modeled using the Artemis interface to the IFEFFIT software package.[100] In the 1.2% SnS(Sb) film, antimony may either be incorporated into the film as an Sb_{Sn} substitution as desired, or as Sb_2S_3 second-phase particles. For this reason, we evaluated both structural models: (a) a 6-shell model of SnS with the Sb_{Sn} substitution at the central atom, denoted by SnS(Sb_{Sn}); and (b) a 4-shell model of Sb_2S_3 with the two distinct lattice sites of Sb in Sb_2S_3 weighted equally. For the 4.5% SnS(Sb) film, we evaluated a 2-shell model of Sb metal. Figure 4.5 gives a spatial

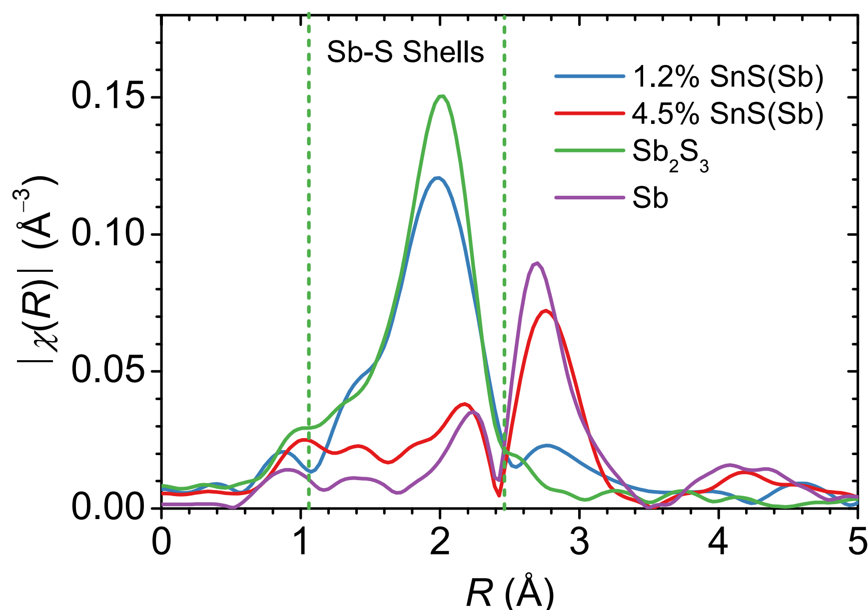

Figure 4.4: Summary of EXAFS measurements: The magnitude of the complex Fourier transform of χ(k) at the Sb edge of the 1.2% SnS(Sb) film, 4.5% SnS(Sb) film, Sb_2S_3 film, and Sb metal standard. The peak at 2 Å in the Sb_2S_3 data is due to sulfur nearest neighbors of antimony.

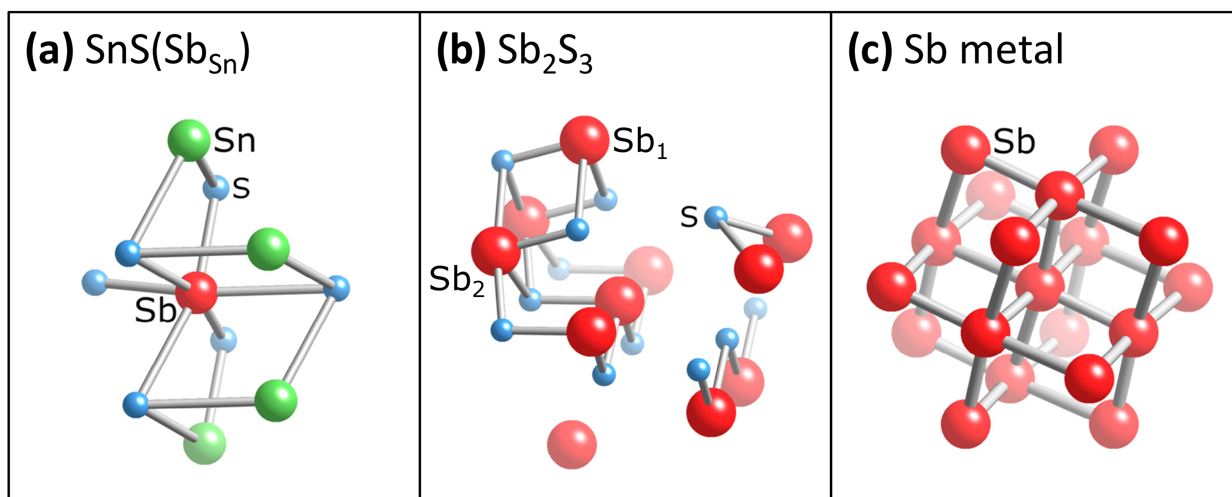

Figure 4.5: Ball-and-stick representation of **(a)** SnS with the Sb_{Sn} substitution at the central atom, **(b)** Sb_2S_3, and **(c)** Sb metal. Green: Sn; Blue: S; Red: Sb. For clarity, the cluster sizes shown are smaller than those used for EXAFS fitting. Note the two distinct lattice sites of Sb in Sb_2S_3, the trivalent Sb_1 and quintvalent Sb_2. Nearest neighbor distances are given in Table 4.2.

representation of each structural model. The paths used in each model are outlined in Table 4.2. The refinements were performed using 6-10 free parameters, including the half-path lengths δR_i, their mean square variation σ_i^2, the relaxation term S_0^2, and energy offset E_0, with 8-12 independent points per dataset.

The refinements of models (a) and (b) achieved good fits (R = 1.5% and R = 1.7%, respectively) for the 1.2% SnS(Sb) data, while the refinement of model (c) achieved a good fit (R= 3.4%) for the 4.5% SnS(Sb) data. Figure 4.6 shows these EXAFS data and fits, and Figure 4.7 shows the real parts and magnitudes of the Fourier transform of these data. Table 4.3 gives the best-fit values of parameters for the fitted spectra. Attempts to refine model (c) for the 1.2% SnS(Sb) data or models (a) and (b) for the 4.5% SnS(Sb) data were not possible with R values

Table 4.2: Path names for each structure model with corresponding half-path lengths and coordination numbers. All paths are single-scattering events with Sb as the atom of origin. For model (b), the atom of origin is shown in brackets to distinguish between the two distinct lattice sites of Sb in Sb_2S_3, denoted by Sb_1 and Sb_2.

Structure model								
$SnS(Sb_{Sn})$ (a)			Sb_2S_3 (b)			Sb metal (c)		
Path	R_{eff} (Å)	N	Path	R_{eff} (Å)	N	Path	R_{eff} (Å)	N
S_1	2.6237	1	$[Sb_1] – S_3$	2.5044	1	Sb_2	2.9063	3
S_2	2.6658	2	$[Sb_1] – S_2$	2.5225	2	Sb_3	3.3513	3
S_3	3.2908	2	$[Sb_2] – S_1$	2.3836	1	-	-	-
S_4	3.3908	1	$[Sb_2] – S_3$	2.6747	2	-	-	-
Sn_1	3.4937	2	-	-	-	-	-	-
Sn_2	3.9870	2	-	-	-	-	-	-

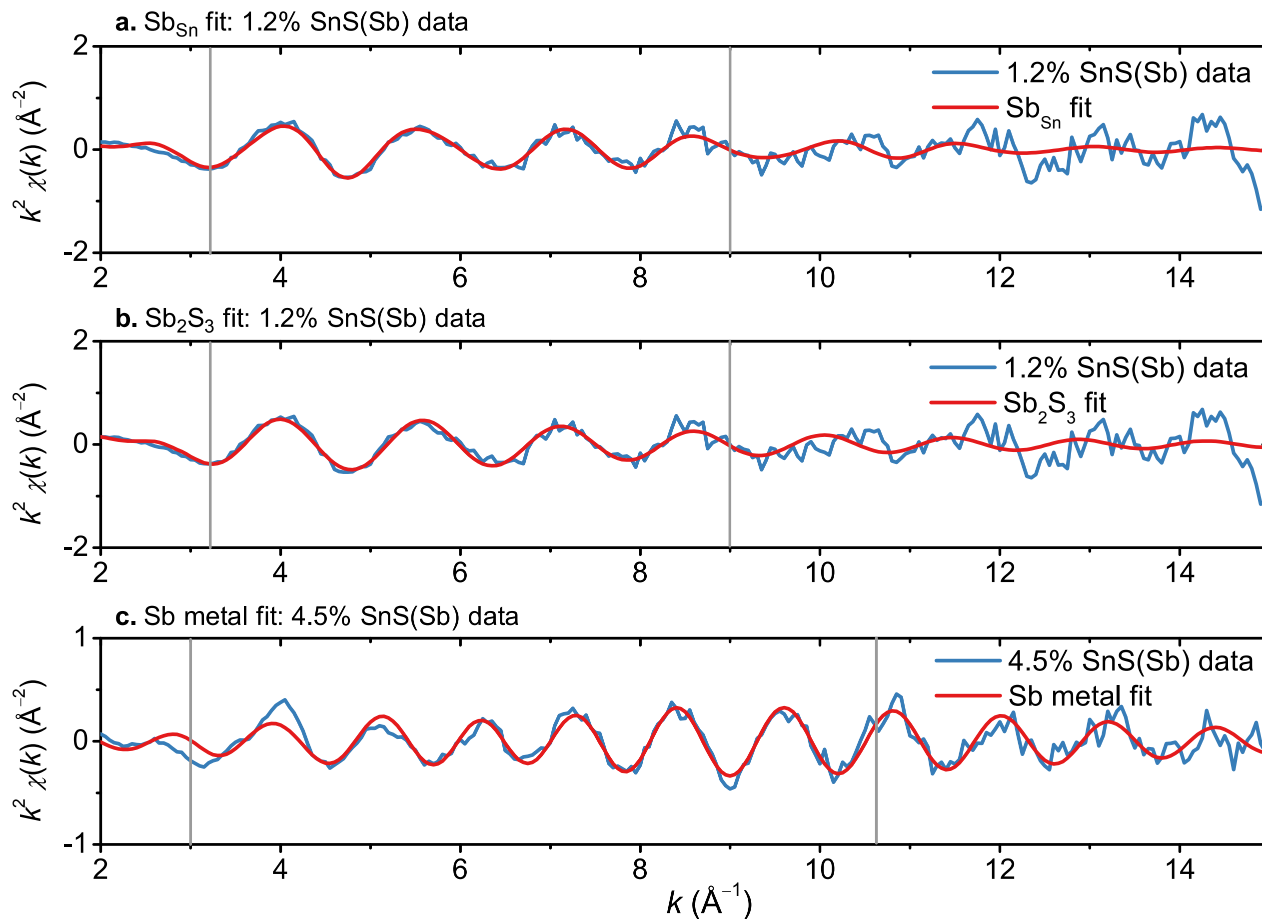

Figure 4.6: EXAFS data and fits for Sb edge: **(a)** 1.2% SnS(Sb) data with SnS(Sb_{Sn}) fit, **(b)** 1.2% SnS(Sb) data with Sb_2S_3 fit, and **(c)** 4.5% SnS(Sb) data with Sb metal fit. The vertical lines denote the range chosen for Fourier transformation.

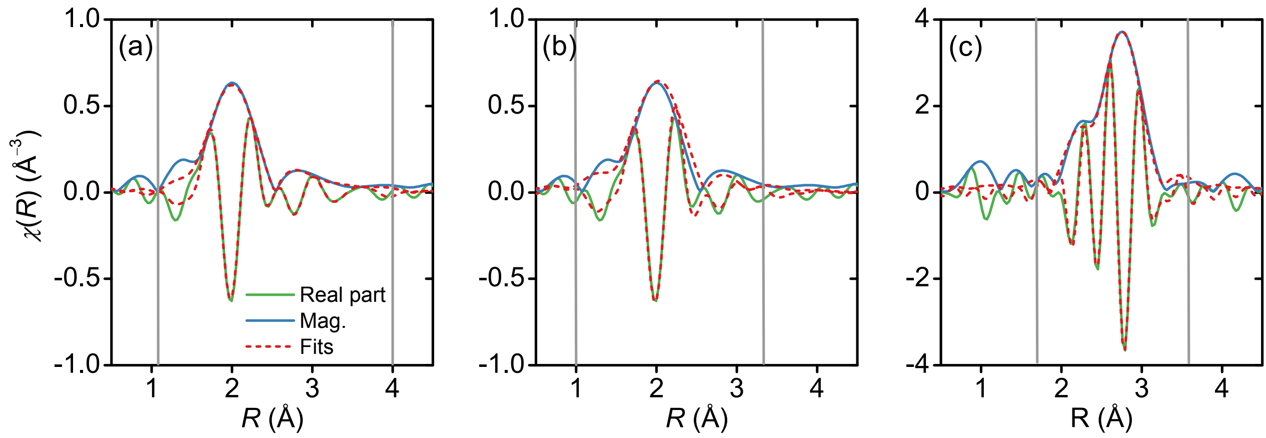

Figure 4.7: Real part and magnitude of Fourier transformed EXAFS data and fits: **(a)** 1.2% SnS(Sb) data with SnS(Sb_{Sn}) fit, **(b)** 1.2% SnS(Sb) data with Sb_2S_3 fit, and **(c)** 4.5% SnS(Sb) data with Sb metal fit. The vertical lines denote the fitting range.

Table 4.3: Best fit EXAFS parameters and corresponding paths for three structure models. Models (a) and (b) are fit to 1.2% SnS(Sb) data, and model (c) is fit to 4. 5% SnS(Sb) data. See Table 1 for path details.

Parameters	Structure model					
	SnS(Sb_{Sn}) [(a)]		Sb_2S_3 [(b)]		Sb [(c)]	
	Values	Path	Values	Path	Values	Path
E_0	10.2 (2.7)	All paths	10.6 (1.0)	All paths	9.9 (2.3)	All paths
S_0^2	0.82 (0.05)	All paths	0.93 (0.10)	All paths	0.77 (0.25)	All paths
δR_1	-0.15 (0.02)	S_1	0.02 (24.7)	$[Sb_1]-S_3$	0.00069 (0.017)	Sb_2
δR_2	δR_1	S_2	0.0002 (2.8)	$[Sb_1]-S_2$	0.0032 (0.060)	Sb_3
δR_3	0.050 (0.089)	S_3	-0.01 (0.07)	$[Sb_2]-S_1$	-	-
δR_4	0.21 (0.35)	S_4	-0.16 (0.36)	$[Sb_2]-S_3$	-	-
δR_5	-0.08 (0.11)	Sn_1	-	-	-	-
δR_6	-0.26 (0.13)	Sn_2	-	-	-	-
σ_1^2	0.0052 (0.0020)	S_1	0.003	$[Sb_1]-S_3$	0.0051 (0.0024)	Sb_2
σ_2^2	σ_1^2	S_2	σ_1^2	$[Sb_1]-S_2$	0.019 (0.011)	Sb_3
σ_3^2	0.011 (0.022)	S_3	0.0063(0.0072)	$[Sb_2]-S_1$	-	-
σ_4^2	σ_3^2	S_4	0.0056 (0.0031)	$[Sb_2]-S_3$	-	-
σ_5^2	0.014 (0.039)	Sn_1	-	-	-	-
σ_6^2	σ_5^2	Sn_2	-	-	-	-

under 60%. The Sb substitutional [SnS(Sb_{Sn})] model qualitatively gives the best fit for the 1.2% SnS(Sb) data, closely matching the phase and amplitude of $\chi(R)$ beyond the sulfur shells. Although the Sb_2S_3 model also fits reasonably well to the data, formation of the Sb_2S_3phase is unsupported by XRD of the 1.2% SnS(Sb) film. Peaks corresponding to Sb_2S_3 were not observed in the XRD pattern, and the SnS lattice constant shift indicates an incorporation of Sb into the SnS lattice. Furthermore, the phase composition of the SnS-Sb system as measured by Kurbanova *et al*. includes only the SnS and Sb phases for temperatures of 30-500 ^{o}C.[101] For these reasons, we believe that antimony is predominantly acting as a substitutional dopant in the 1.2% SnS(Sb), causing the observed increase in resistivity. However, we cannot rule out the possibility that a small fraction of Sb exists in the Sb_2S_3 phase, falling below the sensitivity of XRD.

The Sb metal model matches well with the 4.5% SnS(Sb) EXAFS data. This supports our hypothesis that the antimony in the 4.5% SnS(Sb) is present predominantly in a secondary phase, consistent both with our XRD observation of a new peak emerging with high doping density, and with the aforementioned phase composition study of the SnS-Sb system.[101] The formation of Sb metal observed by EXAFS may underlie the decrease of resistivity at the highest Sb doping level; since the majority of dopant atoms in this film do not occupy substitutional lattice sites, the degree of compensation is reduced, and the free hole concentration is increased. We also note that dopant precipitation into metallic nanoparticles has been observed for other systems such as metal-doped ZnO.[102,103]

4.5 Conclusions

SnS has always been observed to be a *p*-type semiconductor. One promising *n*-type substitutional dopant is antimony(III), Sb^{3+}, due to the similarity of its ionic radius to Sn^{2+}. Sb-doped SnS thin films were deposited by pulsed-CVD using the reaction of $Sn(MeC(N\text{-}i Pr)_2)_2$ and $Sb(NMe_2)_3$ with H_2S. Small amounts of Sb (~1%) in SnS increase the film resistivity by more than two orders of magnitude, most likely due to substitutional doping. Sb addition at low levels is an effective means of producing compensated, insulating SnS films, which could be useful in solar cells with a *p-i-n* heterostructure. The conductivity type of the Sb-doped SnS films could not be determined because of their high resistivity. Increasing the doping level from 1.2% to 4.5% appears to cause clustering of the Sb into metallic precipitates, as confirmed by EXAFS and XRD.

4.6 Acknowledgements

Several people contribute to the work in this chapter. The author developed and prepared antimony-doped SnS films as well as collected, characterized and interpreted their properties. Sang Bok Kim synthesized the tin(II) precursors used in this experiment. Rupak Charkraborty and Steven M. Heald performed EXAFS measurement and analyzed and interpreted the EXAFS data. Roy Gordon and Tonio Buonassisi supervised the research and guided the manuscript preparation. This work was supported by the U.S. Department of Energy SunShot Initiative under Contract No. DE-EE0005329, by the U.S. National Science Foundation under grant No. CBET-1032955, and by Saint Gobain S. A., which also supplied the SIMS analyses.

Chapter 5

Heat Treatment in SnS Thin Films

5.1 Chapter abstract

A post-deposition heat treatment process can be used to improve the quality of absorber materials and thus enhance the device performance of thin film solar cells. ALD SnS films were annealed in N_2, H_2S, or elemental sulfur ambient in the temperature range of 250 – 400 °C for 1 hr. A rapid thermal process was employed when annealing above 500 °C to suppress the mass loss (*e.g.*, evaporation) in SnS films. Temperature and anneal atmosphere have profound impacts on the grain growth, grain orientation and electrical properties of SnS films. Above 350 °C, despite improving film crystallinity, annealing SnS in N_2 substantially lowers film mobility, presumably due to higher scattering from the defects (*i.e.*, sulfur vacancies) caused by desulfurization. A small amount of sulfur vapor can suppress an increase in sulfur vacancies and preserve the film mobility. A H_2S ambient provides the best improvement in grain growth and carrier mobility, as compared to N_2 and sulfur.

5.2 Introduction

Post-deposition annealing in certain conditions is shown to increase the efficiency of thin film solar cells by improving material properties in the absorber layer such as promoting grain growth; passivating and reducing bulk and interface defects; and providing re-crystallization and strain relief. The presence of chlorine can increase grain size and reduce stacking fault density in CdTe films.[104,105] As deposited CSS CdTe devices generally have efficiencies between 6% and 10%, whereas cells with the $CdCl_2$ anneal are generally more than 12% efficient.[106] In addition to chlorine, oxygen also plays an important role in high efficiency CdTe devices. All high efficiency cells ($\eta > 15$ %) are fabricated with oxygen incorporation, but to date it is not clear which effect is actually responsible for the superior device performance.[4] For CIGS and CZTSSe deposited via sulfurization or selenization of alloy layers or compound precursors, sulfur and selenium contents of the films can be adjusted by the final annealing process at elevated temperature in a suitable atmosphere such as elemental sulfur, H_2S, elemental selenium, or H_2Se.[20,107-110]

In the case of SnS, theoretical calculation shows that sulfur vacancy (V_S) has a negatively charge state inside the band gap which could act as electron traps.[17] Due to the high vapor pressure of sulfur, desulfurization from SnS films was also observed after annealing in argon at 400 °C.[111] As a result, H_2S and elemental sulfur were chosen for anneal atmospheres to reduce the density of sulfur vacancies in SnS. The films were also annealed in an inert N_2 atmosphere for a comparison.

5.3 Experiment section

SnS films was prepared by pulsed-CVD from Sn(amd)$_2$ and H_2S (4%, Airgas) at 200 °C on SiO_2/Si wafer substrates, as described in detailed in section 3.3.[112] The film thickness is between 500 and 600 nm. SnS films were annealed in the range of 250 − 400 °C (Figure 5.1a) for 1 hr. in N_2, H_2S, or sulfur atmosphere. Unlike film deposition, the source of H_2S for heat-treatment is a pure gas (99.9% H_2S, Matheson Trigas). The flow rate of N_2 and H_2S gases was kept at 40 sccm. For the sulfur atmosphere, 10 sccm of N_2 was used to carry sulfur vapor from a sulfur source (> 99.5%, Sigma Aldrich) held at 70 °C and mixed with additional 30 sccm of N_2 in the annealing zone. To prevent condensation of sulfur on the surface of the SnS film, sulfur vapor was supplied only when the substrate temperature was above 200 °C. The total pressure was maintained at 10 Torr.

An attempt to anneal at a higher temperature (≥ 500 °C) for 1 hr resulted in an apparent mass loss due to evaporation of SnS films. To overcome this problem, rapid thermal annealing

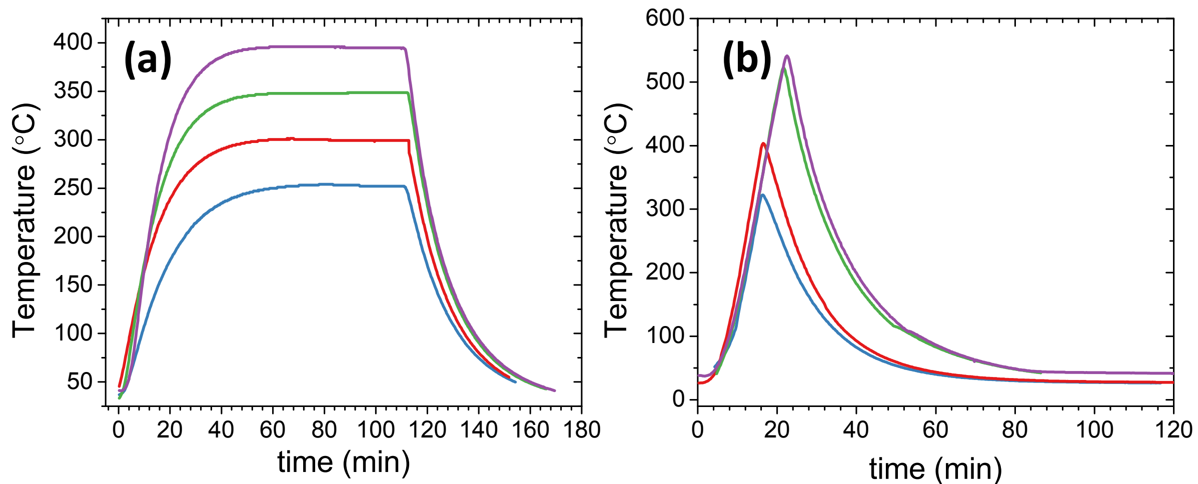

Figure 5.1: Temperature profiles of **(a)** 1 hr and **(b)** RTA annealing at various temperatures.

(RTA) was used for annealing SnS at an elevated temperature. Only annealing in H_2S was performed for this RTA process. The experiment set up follows. Samples were placed inside the reactor tube at room temperature. The flow rate of H_2S and total pressure were maintained at 40 sccm and 10 Torr, respectively. Then, the reactor furnace was set constant at 800 °C. It took *ca.* 15 min for the reactor tube to reach this temperature. The temperature ramp rate of the substrate holder (stainless steel) placed inside the reactor tube was *ca.* 24 °C/min, as shown in Figure 5.1b. Once the temperature of the substrate holder reached the desired annealing temperature (300 – 550 °C), the reactor furnace was turned off and the samples were allowed to cool down to room temperature in the H_2S atmosphere. The annealed films were characterized with SEM (Zeiss, Ultra-55), XRD (PANalytical X'Pert Pro), and Hall measurement (MMR Technologies) using the van der Pauw method.

5.4 Results and discussion

5.4.1 Grain growth in heat-treated SnS films

Temperature and anneal atmosphere strongly influence the morphology and crystallinity of SnS films. SEM images of the annealed films (Figure 5.2 - 5.4) indicate an increase in grain size with annealing temperature, a result of the dependence of the grain boundary scattering on temperature. Morphology and crystallinity of the films start to change noticeably at 300 °C for H_2S and 400 °C for N_2 and sulfur. At the same temperature, annealing in the H_2S atmosphere provides the best grain growth while that in sulfur and nitrogen atmospheres produces comparable grain size and crystallinity, as observed from the cross-section SEM (Figure 5.5). Some of the observed annealing results can be explained by general features of grain growth in

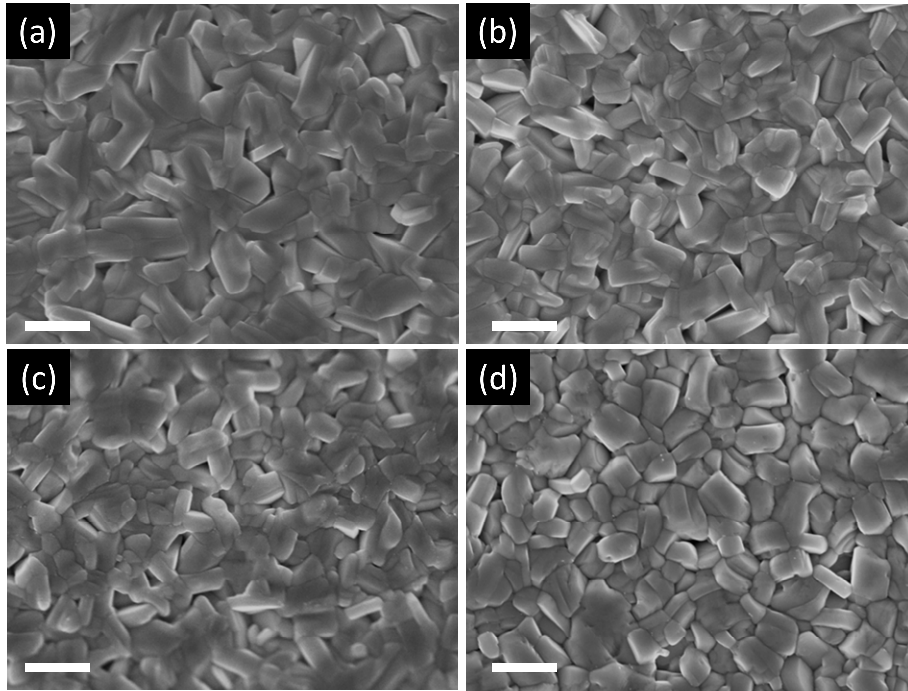

Figure 5.2: SEM images of **(a)** as-deposited and annealed SnS in 10 Torr of N_2 at substrate temperatures of **(b)** 300 °C, **(c)** 350 °C, and **(d)** 400 °C for 1 hr. The scale bar is 500 nm.

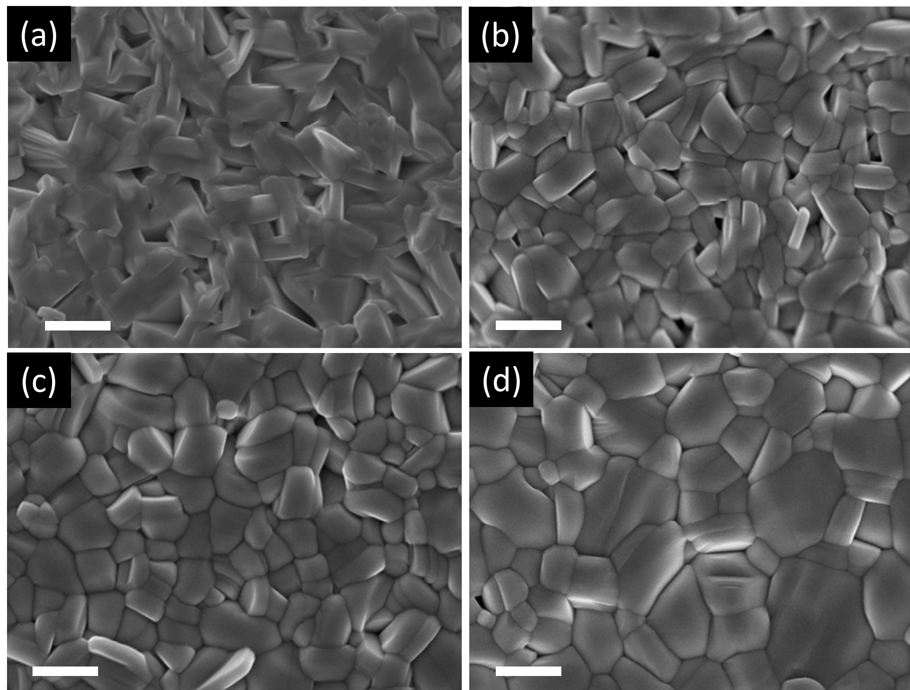

Figure 5.3: SEM images of **(a)** as-deposited and annealed SnS in 10 Torr of H_2S at substrate temperatures of **(b)** 300 °C, **(c)** 350 °C, and **(d)** 400 °C for 1 hr. The scale bar is 500 nm.

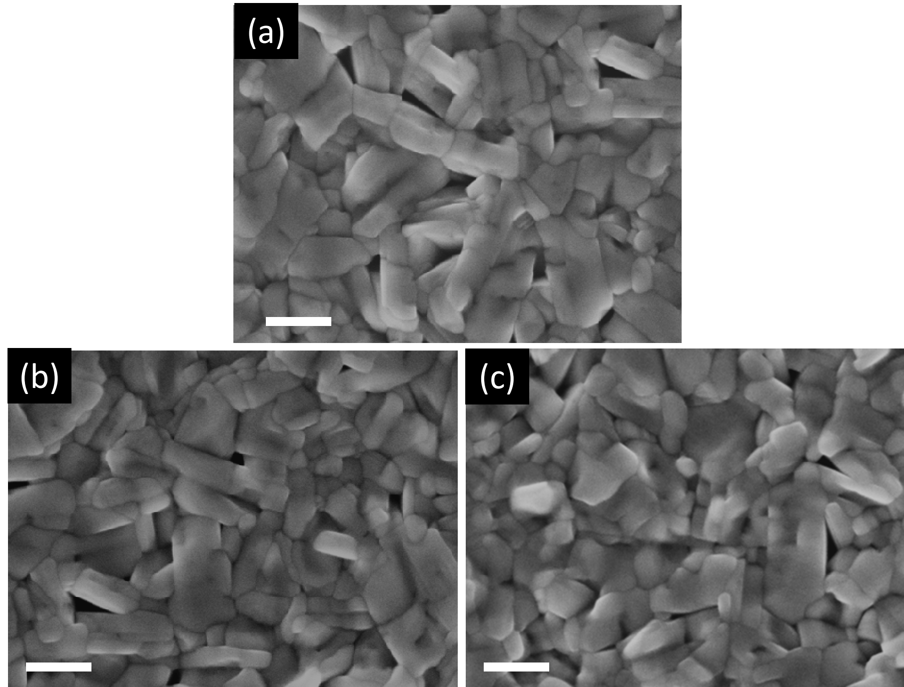

Figure 5.4: SEM images of **(a)** as-deposited and annealed SnS in sulfur at substrate temperatures of **(b)** 300 °C, and **(c)** 400 °C for 1 hr. The scale bar is 500 nm.

thin films as follows: if the grain size is smaller than the film thickness, three-dimensional normal grain growth (an equiaxed structure) occurs.[113] Once three-dimensional grain growth reaches an average grain size that is comparable to the film thickness (a columnar structure, *i.e.*, all grain boundaries intersect the top and bottom surfaces of the film), normal grain growth usually slows and eventually stops.[113] This growth behavior can be seen in Figure 5.5. The as-deposited film has a near-columnar microstructure with grain size, especially at the bottom, smaller than the film thickness. After annealing, these small grains undergo three-dimensional normal grain growth and eventually produce a columnar structure. The next stage of grain growth (referred to as abnormal or secondary grain growth) happens in a way that a small fraction of the population of grains continues to grow while the majority of the grains either do

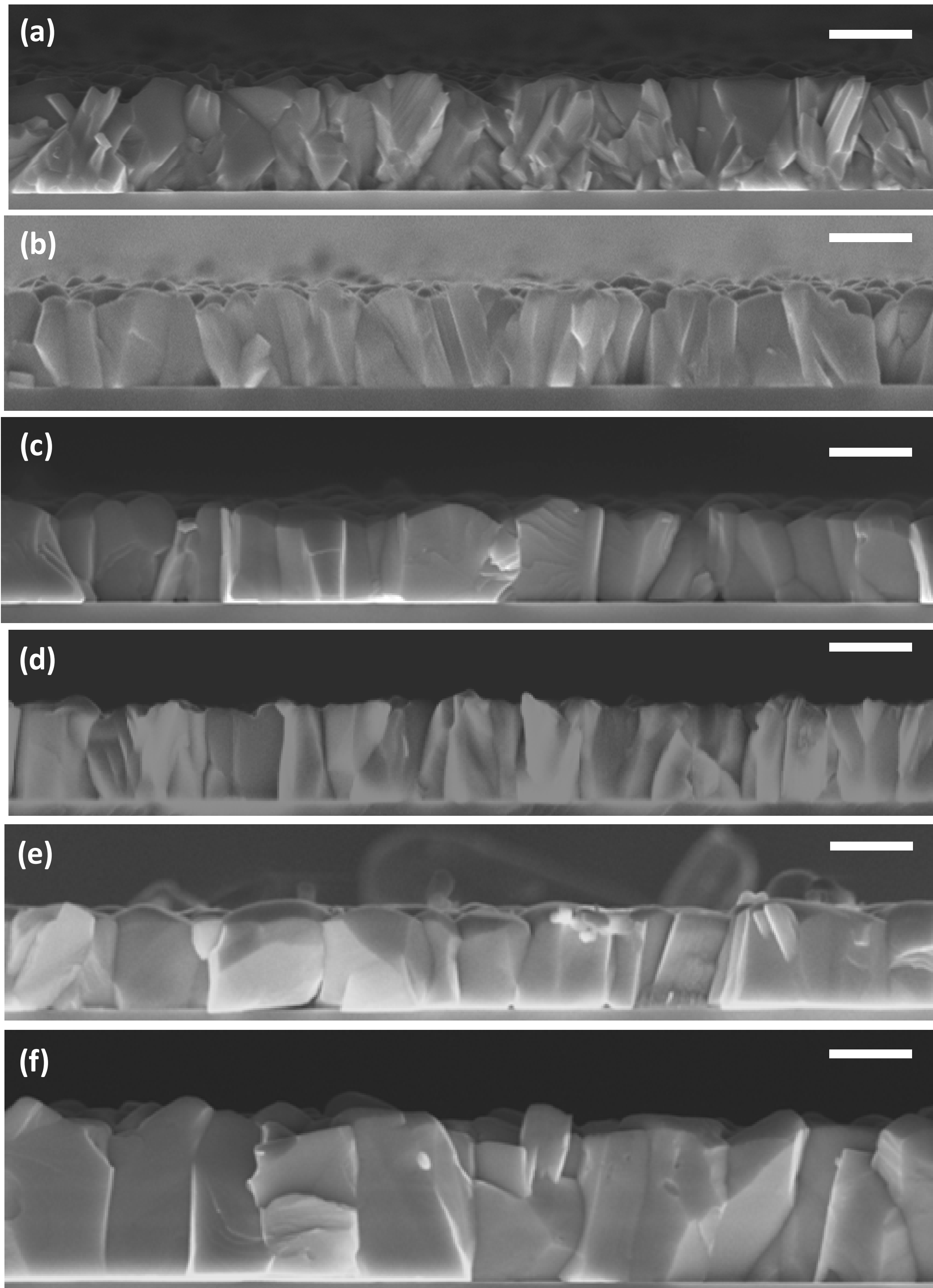

Figure 5.5: Cross-section SEM images of **(a)** as-deposited SnS; annealed SnS films at 400 °C in **(b)** N_2, **(c)** H_2S, **(d)** sulfur for 1 hr; and RTA in H_2S at **(e)** 500 and **(f)** 540 °C. The scale bar is 500 nm. The increase in film thickness of (f) is because of a sublimation of SnS from the hotter reactor wall to the colder substrate.

not grow at all or grow at much lower rates, *i.e.,* a subset of grains growing at a higher rate at the expense of their neighbors.[113] This process was observed when SnS films were annealed in H_2S above 350 °C (Figures 5.3c, 5.3d, and 5.7c).

The crystal structure of SnS films was preserved and no additional phase was detected after the annealing. However, an anneal atmosphere has some effects on the crystallographic orientation of the films. Figure 5.6a shows that annealing SnS in N_2 significantly increases the intensity of the (040) layer-plane peak of the films. Nonetheless, such result is not observed if the starting SnS film does not exhibit a (040) peak before annealing (Figure 5.6b). In contrast to N_2, annealing in H_2S suppresses the intensity of the (040) peak. Because the energy of the surface of a crystal depends on its orientation, anisotropy of the surface free energy plays a very important role in grain growth in thin films.[113] In principle, grains with orientations that have minimum surface energies will grow at higher rates than other grains, resulting in the

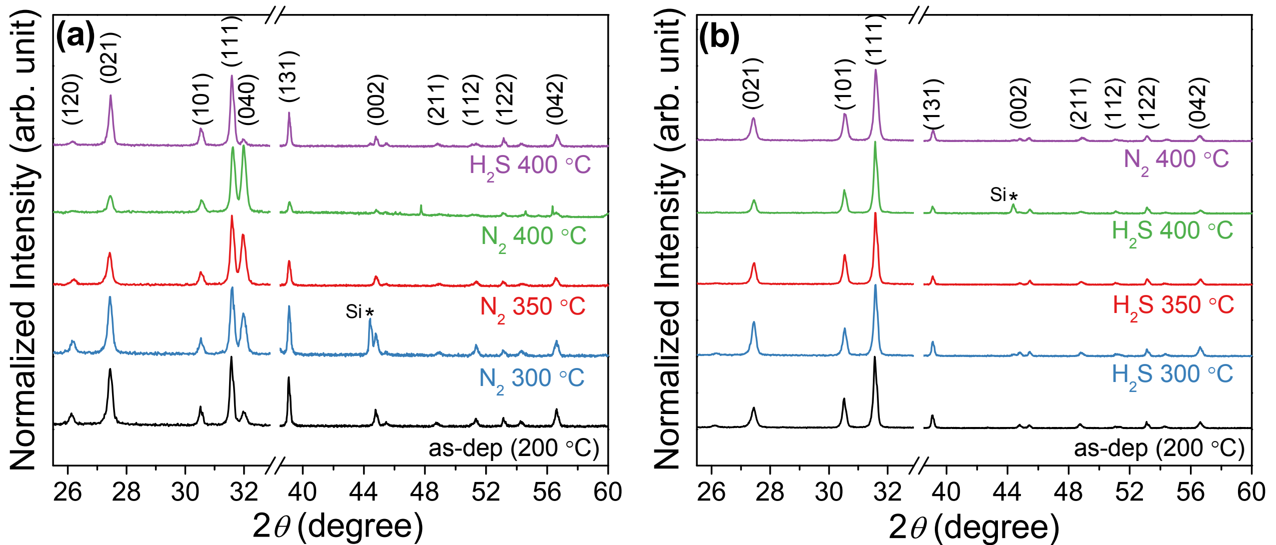

Figure 5.6: XRD spectrum of annealed SnS films in N_2 and H_2S ambients using as-deposit film **(a)** with and **(b)** without (040) layer-plane peak. The intensity was normalized to (111) peak.

abnormal grain growth mentioned previously. Different gaseous ambient may also lead to different surface energy minimization and could therefore affect the orientations and the rate of the grain growth, as observed in this case.

5.4.2 Rapid thermal annealing

To overcome the problem of SnS films evaporated out from substrates at elevated temperature, the RTA process (Fig 5.1b) was used for annealing above 500 °C. Figure 5.7 shows SEM images of the rapid annealed SnS in an H_2S atmosphere. As expected, at the same temperature (400 °C), RTA does not produce a grain size as large as in a 1 hr annealing. At 500 °C, the abnormal grain growth becomes more apparent. In some areas of samples rapidly

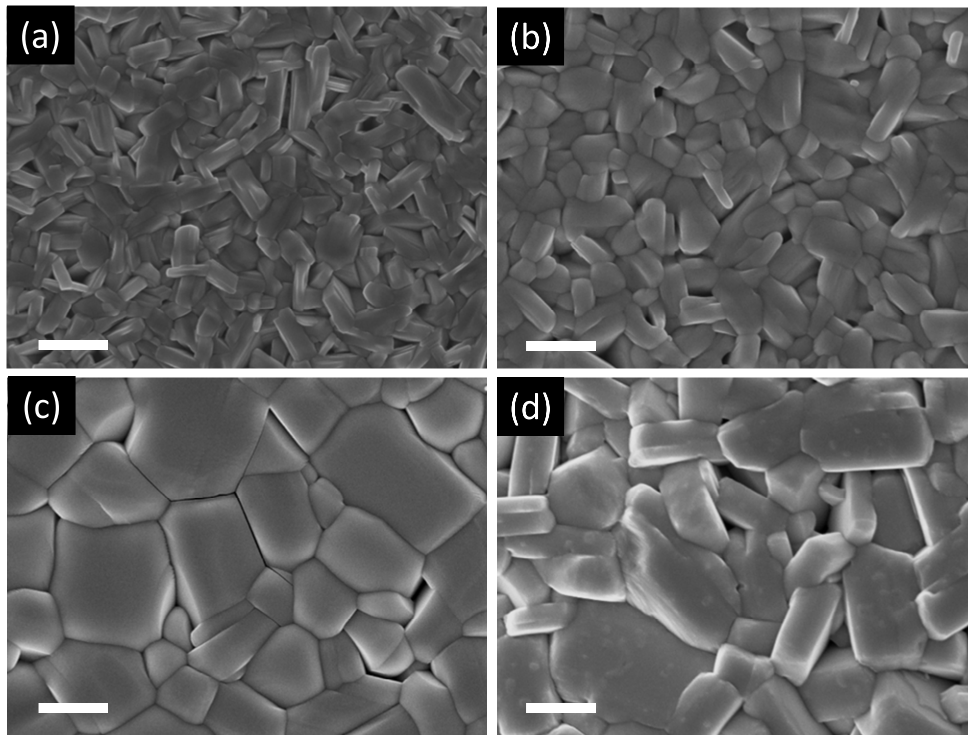

Figure 5.7: SEM images of **(a)** as-deposited and RTA SnS in 10 Torr of H_2S at substrate temperatures of **(b)** 400 °C, **(c)** 500 °C, and **(d)** 540 °C. The scale bar is 500 nm.

annealed above 500 °C, separation between the surfaces of adjacent grains was observed, as shown in Figure 5.8. This grain separation propagated into a film crack in certain areas after cleaving the films (Figure 5.8 inset). This result might be caused by differential thermal expansion or contraction during the annealing process

Interestingly, rather than observing mass loss, the thickness of the films after annealing above 500 °C (Figure 5.5f) increases from 0.6 µm to 1.5 and 1.2 µm at 520 and 540 °C, respectively. This outcome results from the mass transfer of SnS from the film which was previously coated on the reactor wall to the substrate. With the way the experiment was set up, the reactor wall temperature was always at least 100 °C higher than the substrate, resulting in a sublimation of SnS from the hotter reactor wall to the colder substrate provided that the temperature was high enough (~ 500 °C) to evaporate SnS from the reactor wall. The film was thicker at 520 °C because of the order of the annealing. This result demonstrates the possibility of depositing SnS via closed space sublimation (CSS) or thermal evaporation, given that the SnS

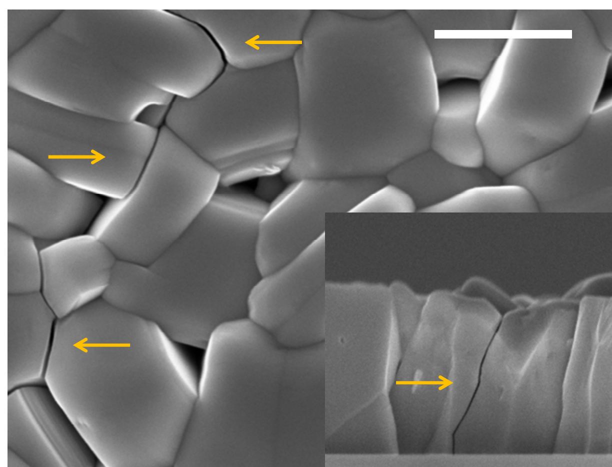

Figure 5.8: a plan-view SEM image of SnS films RTA in H_2S above 500 °C showing separation between the surfaces of adjacent grains which propagates into a small crack after cleaving the films. The scale bar is 500 nm.

target is of good quality. Some advantages of chemical vapor transports over physical vapor deposition for SnS films were discussed in section 2.2.

5.4.3 Electrical properties of heat-treated SnS films

The electrical properties of all annealed SnS films were presented in Figure 5.9. After heat treatment, resistivity of the film decreases from *ca.* 350 to 70 and 200 Ω cm in H_2S and sulfur, respectively, but increases to *ca.* 700 Ω cm in N_2. The carrier concentrations are still in the range of 10^{15} - 10^{16} cm^{-3} after annealing. The trend is an increase of hole density with the annealing temperature, regardless of the annealing atmospheres, and is in the order of $N_2 > H_2S > $ sulfur at 400 °C. Due to the high volatility of sulfur, loss of sulfur from SnS is commonly observed after annealing in an inert atmosphere.[111,114] In a Sn-rich limit, the sulfur vacancy (V_S) has lower formation enthalpy than the tin vacancy (V_{Sn}), but it does not significantly compensate the *p*-type conductivity because the transition level (2+/0) of V_S (Figure 5.10) lies very close to the valence band maximum (VBM).[17] If sulfur loss generated purely the sulfur vacancy, SnS would remain *p*-type with a lower carrier concentration. However, carrier concentration in SnS films was observed to increase with sulfur loss.[111,114] One possible mechanism for carrier concentration to increase with desulfurization is the generation of the tin vacancy thought neutral Sn-on-S antisite ($Sn_S^{\times}$) formation, as shown in the followed equations:

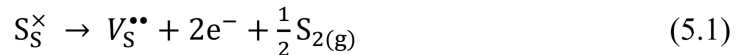

$$S_S^{\times} \rightarrow V_S^{\bullet\bullet} + 2e^- + \frac{1}{2}S_{2(g)} \quad (5.1)$$

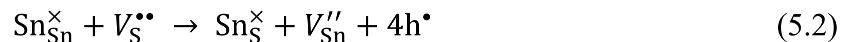

$$Sn_{Sn}^{\times} + V_S^{\bullet\bullet} \rightarrow Sn_S^{\times} + V_{Sn}'' + 4h^{\bullet} \quad (5.2)$$

Upon heating, the end results of desulfurization is given by

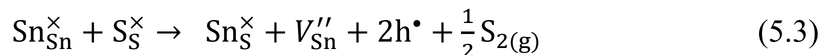

$$Sn_{Sn}^{\times} + S_S^{\times} \rightarrow Sn_S^{\times} + V_{Sn}'' + 2h^{\bullet} + \frac{1}{2}S_{2(g)} \quad (5.3)$$

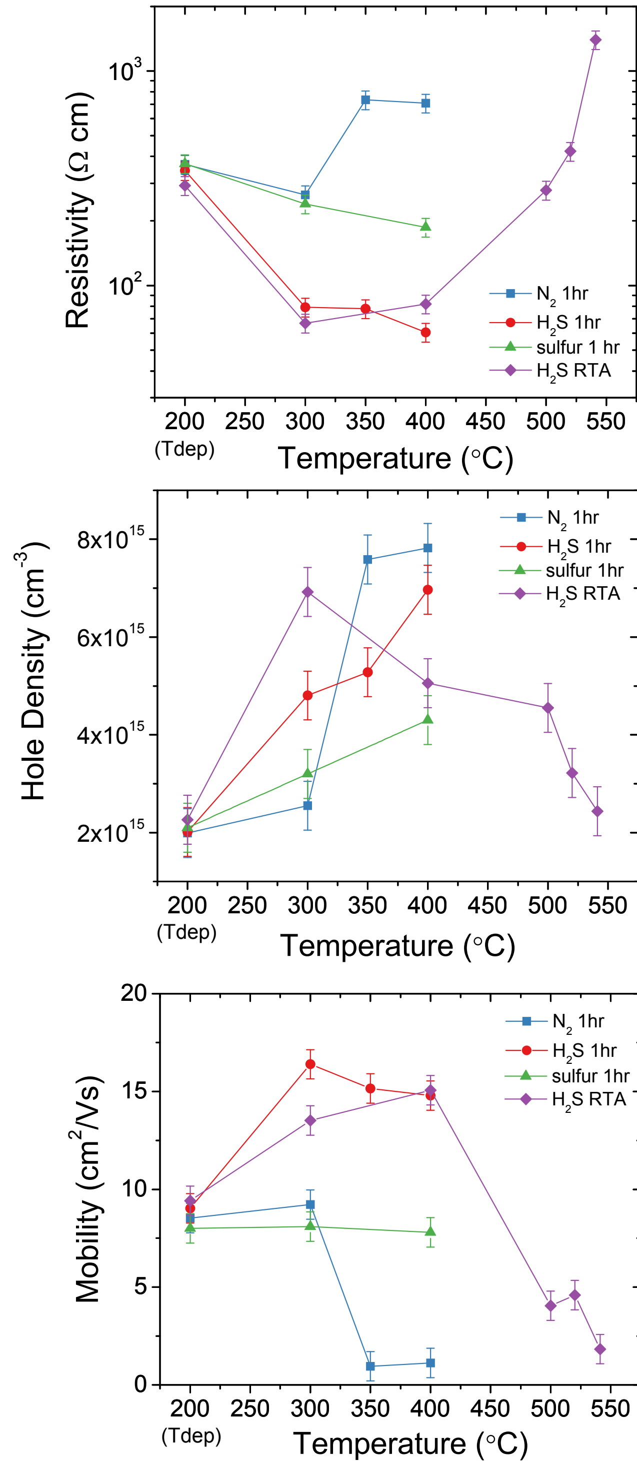

Figure 5.9: Hall measurement results of **(a)** resistivity, **(b)** carrier concentration and **(c)** carrier mobility of heat-treated SnS film in N_2, H_2S, and sulfur atmospheres.

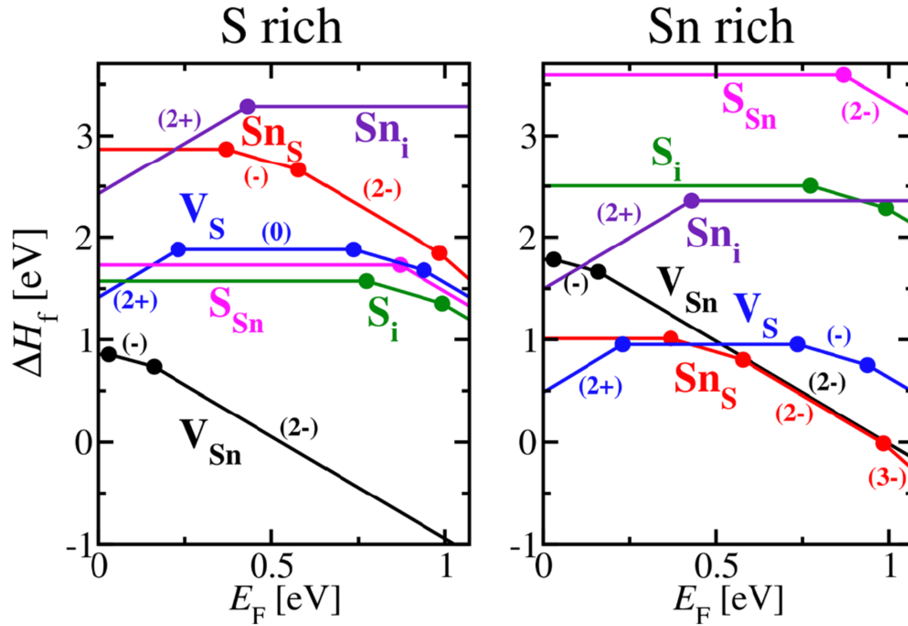

Figure 5.10: Calculated defect formation enthalpies for intrinsic defects in S-rich and Sn-rich limits in SnS, as taken from Ref[17].

In addition to carrier concentration, the annealing ambient also affects the mobility of the SnS films; remaining close to the as-deposited film in sulfur (~8 $cm^2V^{-1}s^{-1}$), decreasing in N_2 (~1 $cm^2V^{-1}s^{-1}$), and increasing in H_2S (~15 $cm^2V^{-1}s^{-1}$) at 400 °C. A significant drop in the mobility of the SnS film after annealing in N_2 ambient above 350 °C can be attributed to an increase in defects due to the loss of sulfur. A similar tread in mobility drop and carrier density increase was also observed by Ghosh *et al.* in SnS films annealed in Ar at 400 °C as well.[111] RTA process in a H_2S atmosphere gives films with comparable electrical properties to 1 hr anneal below 400 °C, *i.e.*, $[p] \sim 4 - 7\times10^{16}$ cm^{-3} and $\mu_p \sim 15$ $cm^2V^{-1}s^{-1}$. Above 500 °C, the carrier concentration remains closer to the as-grown films, but the mobility substantially decreases to be less than 4 $cm^2V^{-1}s^{-1}$, despite a larger grain size. This lower mobility could be from the higher grain boundary scattering because of separation between the surfaces of adjacent grains (Fig 5.8).

5.4.4 Sulfur annealing

Unlike N_2 and H_2S, sulfur has some chemical activity toward SnS, according to the following equilibrium:[115]

$$2SnS(s) + 1/2S_2(g) \rightleftharpoons Sn_2S_3(s) \quad (5.4)$$

During annealing, the sulfur atmosphere should maintain a sulfur activity close to that which is found above the SnS/Sn_2S_3 phase boundary to minimize the sulfur vacancies, but not so high that it converts SnS into Sn_2S_3. The vapor pressure of sulfur in equilibrium with Sn_2S_3 and SnS was measured experimentally and fit in the temperature range of 415 to 547 °C to the following function:[115]

$$\ln P\ (\mathrm{Torr}) = -25860/T(\mathrm{K}) + 29.49 \quad (5.5)$$

Thus, to maintain a pure SnS phase, the S_2 vapor pressure should be below the equilibrium partial pressures of *ca.* 1.6×10^{-7}, 6.1×10^{-6}, and 1.3×10^{-4} Torr at 300, 350, and 400 °C, respectively. The set-up in this experiment was chosen to satisfy this constraint.

The equilibrium vapor pressure of rhombic sulfur (S_8) between solid and gas is given by

$$\ln P\ (\mathrm{Torr}) = -12066/T(\mathrm{K}) + 27.09 \quad (5.6)$$

in the temperature range of 15 – 32.5 °C.[116] The extrapolated value of the S_8 vapor pressure at 70 °C (the source temperature) is calculated to be *ca.* 0.31 mTorr. The S_8 vapor was carried and diluted further by N_2, providing an upper-bound vapor-pressure of 0.078 mTorr above samples. At low temperature, S_8 accounts for over 90% of the vapor, while S_6 and S_7 make up the rest.[117] Once delivered into the annealing zone held at much higher temperatures, it underwent fragmentation into S_n, $2 < n < 8$. The estimated mole fraction of S_2 in a saturated sulfur vapor is less than 0.001 at 300 °C and *ca.*0.02 at 400 °C.[117] As a result, the upper-bound value of S_2 vapor

pressure is in the range of 8×10^{-8} – 1.6×10^{-6} Torr at temperatures between 300 and 400 °C. The partial pressure of an S_2 vapor is extremely low and this might be the reason why the grain growth in sulfur annealing is very similar to that in N_2. Nonetheless, this vapor seems to be high enough to suppress the sulfur loss and preserve the mobility of the films. The carrier concentration of SnS films is also lowest in sulfur ambient. Considering the partial vapor pressure, this result indicates sulfur to be much more active than H_2S in passivating the defects formed during annealing at elevated temperatures.

5.5 Conclusions

SnS films were annealed in N_2, H_2S, or sulfur ambient in the temperature range of 250 – 400 °C for 1 hr. RTA in H_2S was used for an annealing above 500 °C. Temperature and annealing ambient have a substantial effect on the grain growth, grain orientation and electrical properties of SnS films. Grain growth in SnS films can be described by the three-dimensional grain growth to form a columnar structure followed by abnormal grain growth for grain size expansion. Because of desulfurization, the carrier concentration of a SnS film is generally increased with anneal temperature and is in the order of $N_2 > H_2S >$ sulfur. The sulfur loss also creates defects which significantly reduce the mobility of the films annealed in a N_2 atmosphere. A small amount of sulfur vapor can effectively suppress the sulfur loss and preserve the film mobility. A H_2S ambient provides the best grain growth and improves carrier mobility in SnS films the most.

5.6 Acknowledgements

The author acknowledges Annabel Chew and Leizhi Sun for their contribution on Hall measurement and SEM imaging; Sang Woon Lee and Brad Malone for their helpful discussions; and Sang Bok Kim for supplying the tin(II) complex precursor.

Appendix A

Tin(II) complex precursors

This appendix summarizes the synthetic procedures and characterization of tin(II) compounds that can be used as a precursor source for SnS film deposition. The first compound is bis(N,N'-diisopropylacetamidinato)tin(II), referred in this thesis as $Sn(amd)_2$. The second complex is *rac*-1,3-Di-tert-butyl-4,5-dimethyl-1,3-diaza-2-stannacyclopentane-2-ylide, referred in this thesis as cyclic amide of tin(II) (CAT). The deposition of SnS films from these two precursors can be found in chapter 2 and appendix B.

A.1 Experiment Section

A.1.1. Synthesis of tin(II) precursors

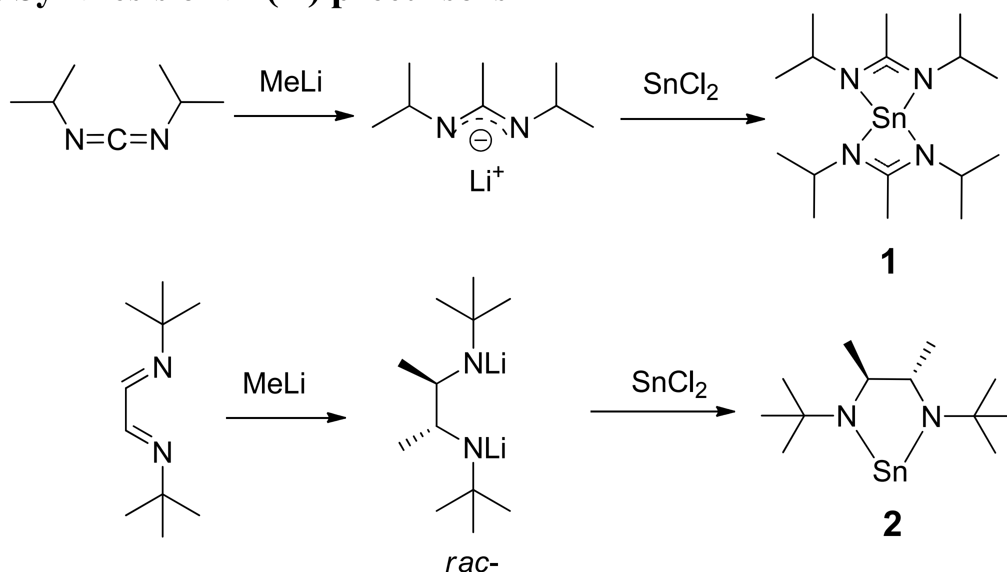

Figure A.1: Syntheses of tin(II) precursors; bis(N,N'-diisopropylacetamidinato)tin(II) (**1**) and *rac*-1,3-Di-tert-butyl-4,5-dimethyl-1,3-diaza-2-stannacyclopentane-2-ylide (**2**).

The whole procedure was performed in the schlenk line under an atmosphere of dry nitrogen or argon inside a hood and a glove box. Tin dichloride (98%, anhydrous), glyoxal solution (40 wt.% in H_2O), methyllithium solution (1.6 M in diethyl ether), THF (anhydrous), pentane (anhydrous), and diethyl ether (anhydrous) were purchased from Sigma-Aldrich. tert-Butylamine was purchased from Acros. All chemicals were used as received. All glassware used in the experiments was dried in the oven at 160 ^{o}C.

Synthesis of Bis(N,N'-diisopropylacetamidinato)tin(II) (1)

1,3–diisopropylcarbodiimide (38.46 g or 47.72 mL, 305 mmol) was added dropwise via syringe to a methyllithium solution (200 mL of 1.6 M, 320 mmol) in anhydrous diethyl ether (250 mL) in a schlenk flask (500 mL) on an ice bath in an argon atmosphere. The ice bath was removed 10 min after the addition and the solution was stirred for 3 hr. The lithium amidinate solution was transferred via cannula to an addition funnel which was connected to a round bottom schlenk flask (1000 mL) containing anhydrous $SnCl_2$ (28.90 g, 152 mmol) and diethyl ether (400 mL) placed on a dry ice – acetone bath (−78 °C). Using an addition funnel, the lithium amidinate was added dropwise to the $SnCl_2$ in diethyl ether over a period of 2 hr under a strong Ar flow. The dry ice-acetone bath was removed 30 min after the complete addition and the reaction mixture was stirred overnight (*ca.* 16 hr). Volatiles were removed under reduced pressure and the yellow colored solid residue was dissolved in pentane (*ca.* 450 mL) for an extraction. Insoluble organic and inorganic salt was filtered on Celite and washes with pentane under an Ar atmosphere. The filtrate was evaporated under reduced pressure. The resulting light yellow colored solid product was transferred to the sublimator inside a glove box. The sublimation was performed at 90-95 °C under vacuum without coolant on the cold finger (air

cooling), yielding a white crystalline solid (42 g, 69%). The dark red residue was observed in the bottom of the sublimator after the sublimation was complete. In case that red color or wet solid product was collected on the cold finger, a second sublimation could be performed for further purification. ^{1}H NMR (C_6D_6, 500 MHz): δ 3.67(sep, J = 6.5, 4H), δ 1.55(s. 6H), δ 1.28(d, J= 6.5, 24H), ^{13}C NMR (C_6D_6, 100 MHz, δ) 165.4, 47.6, 25.5, 12.2 EA: Calcd (%) C 47.90, H 8.54, N 13.97 found (%) C 47.72, H 8.57, N 13.99.

Synthesis of N, N'-di-tert-butyl-2, 3-butylethylenediimine (1,4-diazadiene)[118,119]

Glyoxal solution (75 mL (40 w% in H_2O), 651 mmol,) in distilled water (180 ml) was added dropwise via syringe to a solution of t-butylamine (180 ml,1698 mmol) in distilled water (150 ml) placed inside a round bottom schlenk flask (1000 mL) at room temperature. During the reaction, a solidified white product was observed in the reaction mixture. After 3 hr of the reaction under nitrogen, an additional 50 mL of distilled water was added to the flask. The reaction mixture was stirred for 10 min and filtered on a fritted glass filter. The filter cake was washed three times with distilled water and air-dried with an aspirator. The crude product was dissolved in diethyl ether and then the diethyl ether layer was decanted and evaporated. The lachrymatory white solid was dissolved in a minimum amount of diethyl ether and recrystallized on dry ice twice. The recrystallized solid product was dissolved in diethyl ether and the solution was dried on magnesium sulfate. Afterward, magnesium sulfate was filtered out and the filtrate was evaporated which resulted in a white solid. The solid product was additionally purified by sublimation at 40 ^{o}C under vacuum to yield a white crystalline solid (75 g, 68%) ^{1}H NMR ($CDCl_3$, 500 MHz): δ 7.95(s, 18H), δ 1.27(s. 2H).

Synthesis of *rac*-1,3-Di-tert-butyl-4,5-dimethyl-1,3-diaza-2-stannacyclopentane-2-ylide (2)

MeLi (100 mL of 1.6 M, 160 mmol) was added to anhydrous diethyl ether (150 mL) in a round bottom schlenk flask (500 mL) under an Ar atmosphere. The solution was cooled to 0 °C in an ice bath. To the solution, solid N, N'-di-tert-butyl-2, 3-butylethylenediimine (12.7 g, 75.5 mmol, homemade) was added portion-wise while stirring under a strong Ar flow over a period of 20 min. The ice bath was then removed and the reaction mixture was stirred at room temperature for 1 hr. The diethyl ether solution of the lithiated ligand was transferred via cannula to an addition funnel which was connected to the round bottom schlenk flask (1000 mL) containing anhydrous $SnCl_2$ (14.3 g, 75.5 mmol) and diethyl ether (250 mL) (Figure A.1). Then, the round bottom schlenk flask was immersed in the dry ice-acetone bath under strong Ar flow. After the flask was cooled down, the rate of Ar flow was reduced. Using the addition funnel, addition of the lithiated ligand solution to the $SnCl_2$ in diethyl ether was performed over a period of 4 hr. After the addition was completed, the reaction mixture was kept at −78 °C for 4 hr and then left on the dry ice-acetone bath without adding dry ice until the temperature of the bath reached room temperature. The reaction mixture was additionally stirred at room temperature overnight. The diethyl ether was removed on ice bath under reduced pressure and the crude product was extracted with pentane. The residue was washed two times with fresh anhydrous pentane. The pentane extract was evaporated under reduced pressure resulting in orange colored solids. The obtained crude product was dried at room temperature under vacuum overnight. The solids in the schlenk flask were transferred to the sublimator inside a glove box. The sublimation for the crude product was performed. The temperature of the oil bath was kept between 45 and 50 °C and water was used as the coolant for the cold finger. Light-orange crystalline solids (17.8 g, 74%)

were obtained. ^{1}H NMR (C_6D_6, 500 MHz): δ 3.32(q, J = 6.0, 2H), δ 1.25(s. 18H) 4H), δ 1.20 (d, J= 6.0, 6H), ^{13}C NMR (C_6D_6, 100 MHz, δ) 64.38, 55.99, 34.13, 28.64, EA: Calcd (%) C 45.46, H 8.27, N 8.84 found (%) C 45.35, H 8.17, N 8.66.

A.1.2 Characterization

X-ray structure determination. Diffraction quality crystals were obtained by sublimation. Crystal mounting and data collections were performed on a Siemens (Bruker) SMART CCD diffractometer using Mo Kα radiation. Data reductions were performed with SAINT, which corrects for Lorentz polarization and decay. Space groups were assigned by an analysis of symmetry. Systematic absences were determined by XPREP and were further checked by PLATON. Structures were solved by direct methods and refined against all data in the 2θ ranges by full-matrix least squares on F^2 using SHELXS-97 and SHELXL-97. Hydrogen atoms at idealized positions were included in the final refinements. Refinement details and explanations are included in the individual CIF files. Crystallographic data and final agreement factors are given in the Table.

Thermal Gravimetric Analysis (TGA). A TGA experiment was performed by TA Instruments Model Q50 system in the glove box. N_2 was used as a flow gas. The heating rate and mass of samples used in this experiment were set at 10 °C/min and *ca.* 40 mg, respectively.

A.2 Results

A.2.1 Pictures of tin(II) precursors

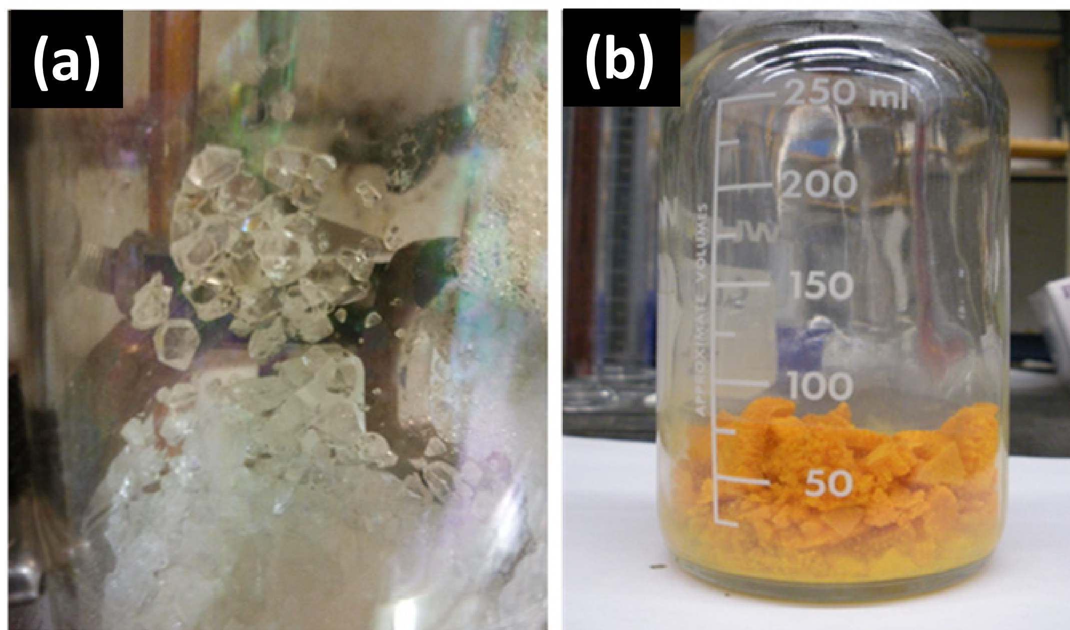

Figure A.2: Pictures of complexes; **(a)** bis(N,N’-diisopropylacetamidinato)tin(II), **(b)** *rac*-1,3-Di-tert-butyl-4,5-dimethyl-1,3-diaza-2-stannacyclopentane-2-ylide.

A.2.2 ^{1}H and ^{13}C NMR spectrum

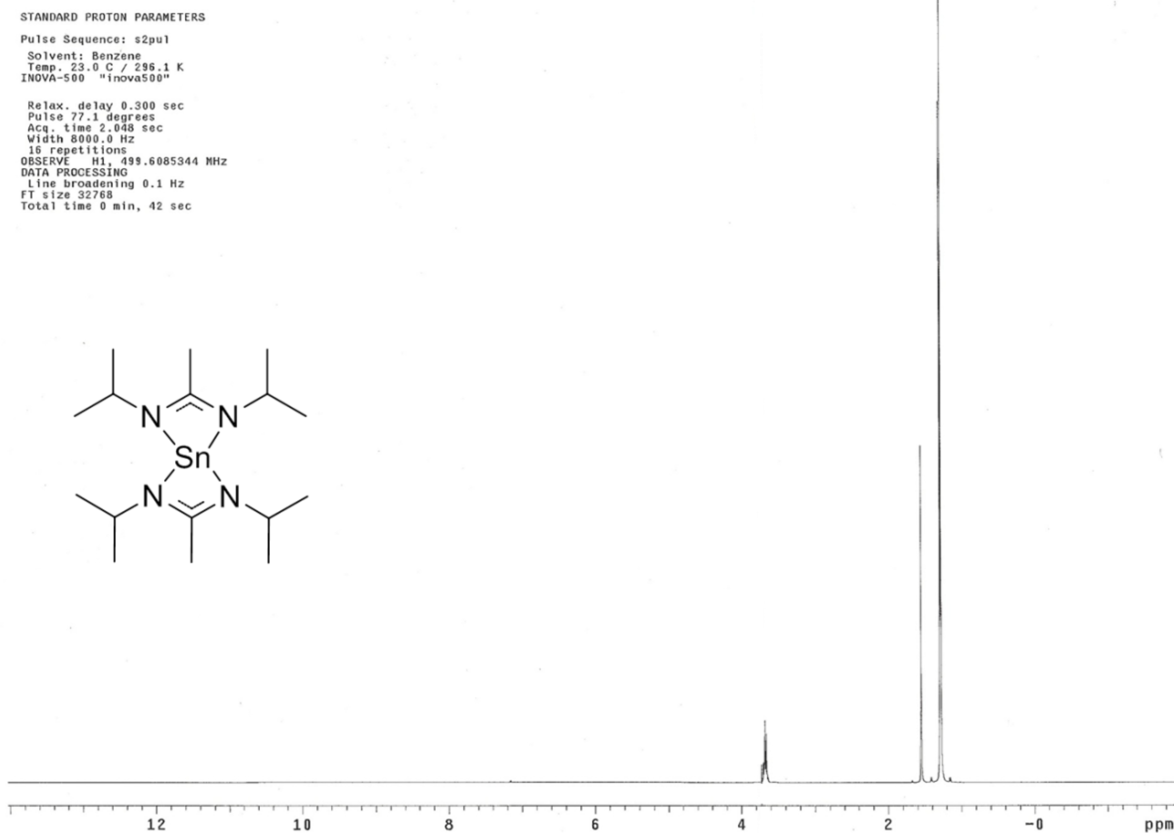

Figure A.3: NMR Spectra (500MHz , C_6D_6) of bis(N,N'-diisopropylacetamidi-nato)tin(II): **(a)** ^{1}H NMR spectrum.

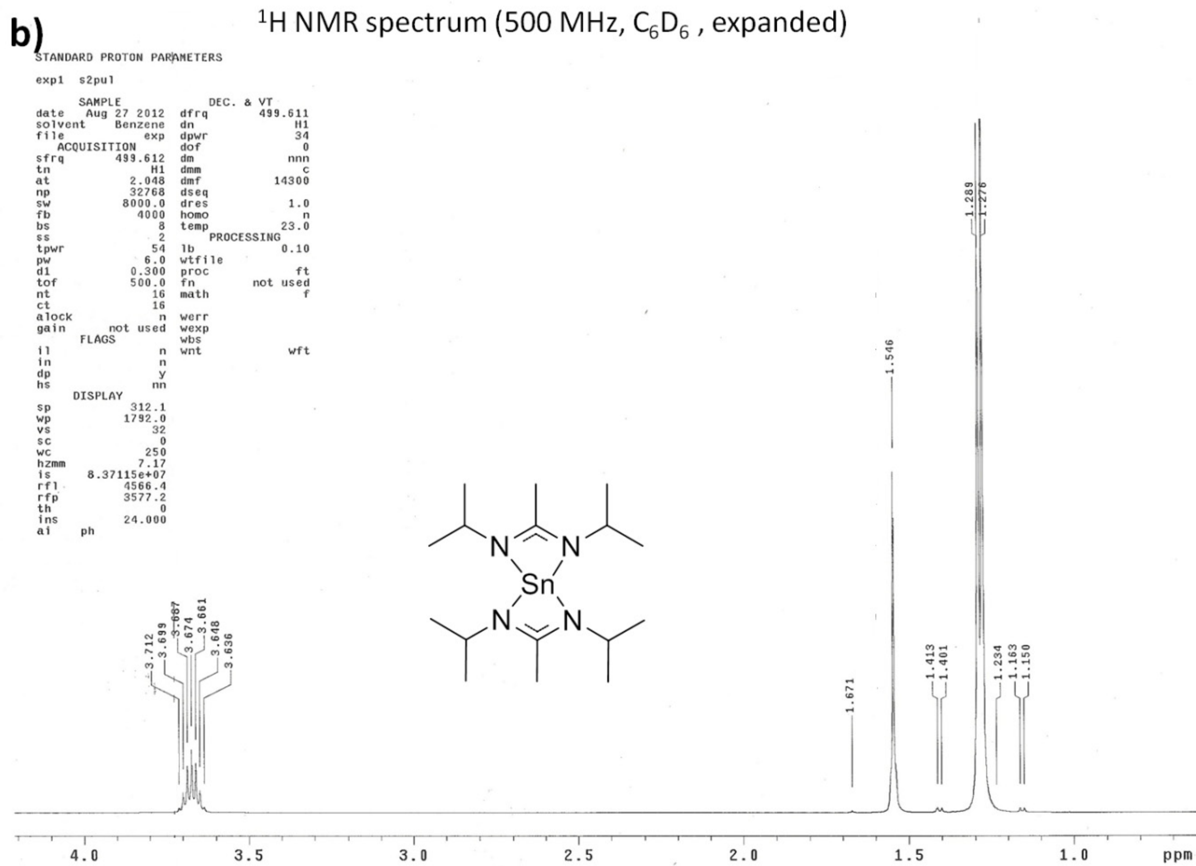

Figure A.3 (Continued): NMR Spectra (500MHz , C_6D_6) of bis(N,N'-diisopropylacetamidinato)tin(II): **(b)** ^{1}H NMR spectrum (expanded).

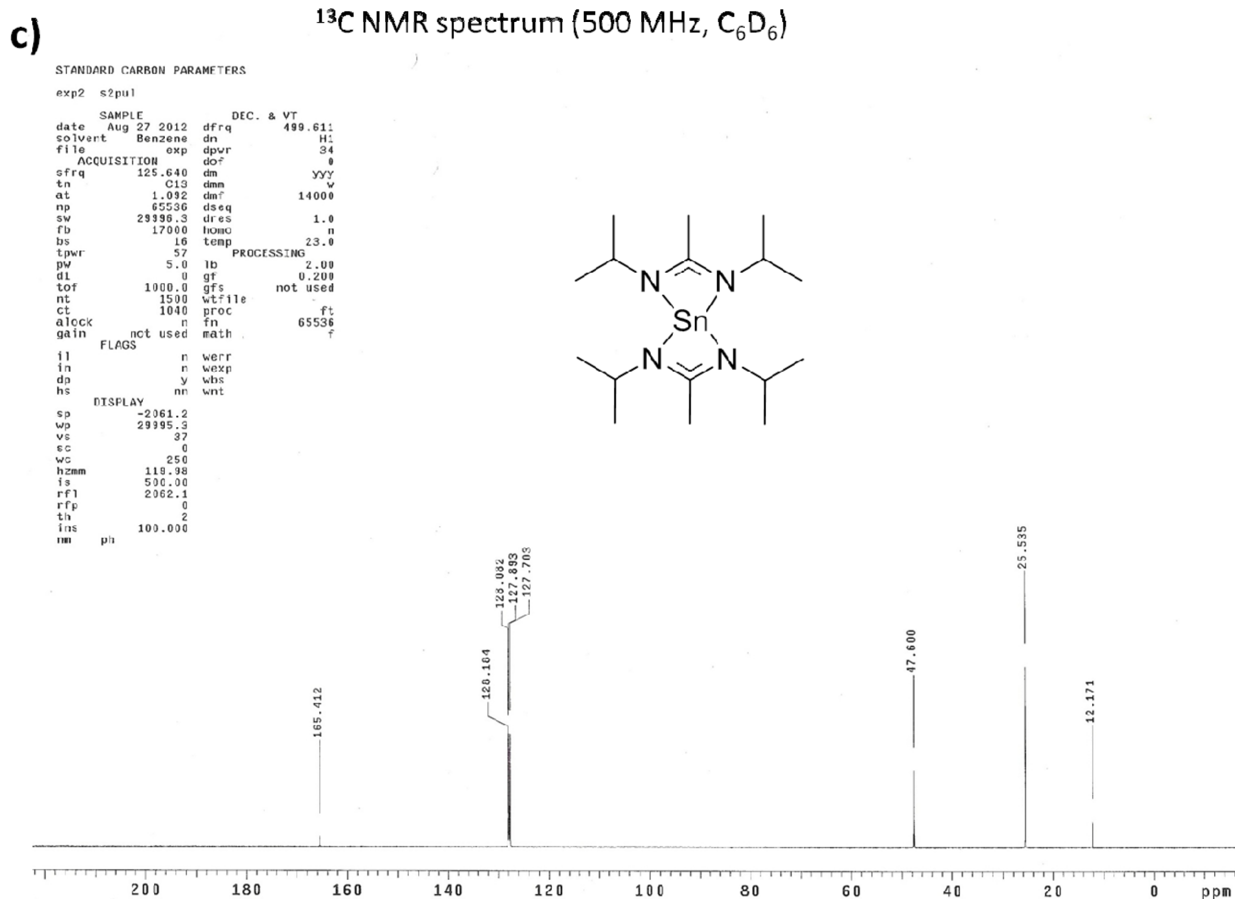

Figure A.3 (Continued): NMR Spectra (500MHz , C_6D_6) of bis(N,N'-diisopropylacetamidinato)tin(II): **(c)** ^{13}C NMR spectrum.

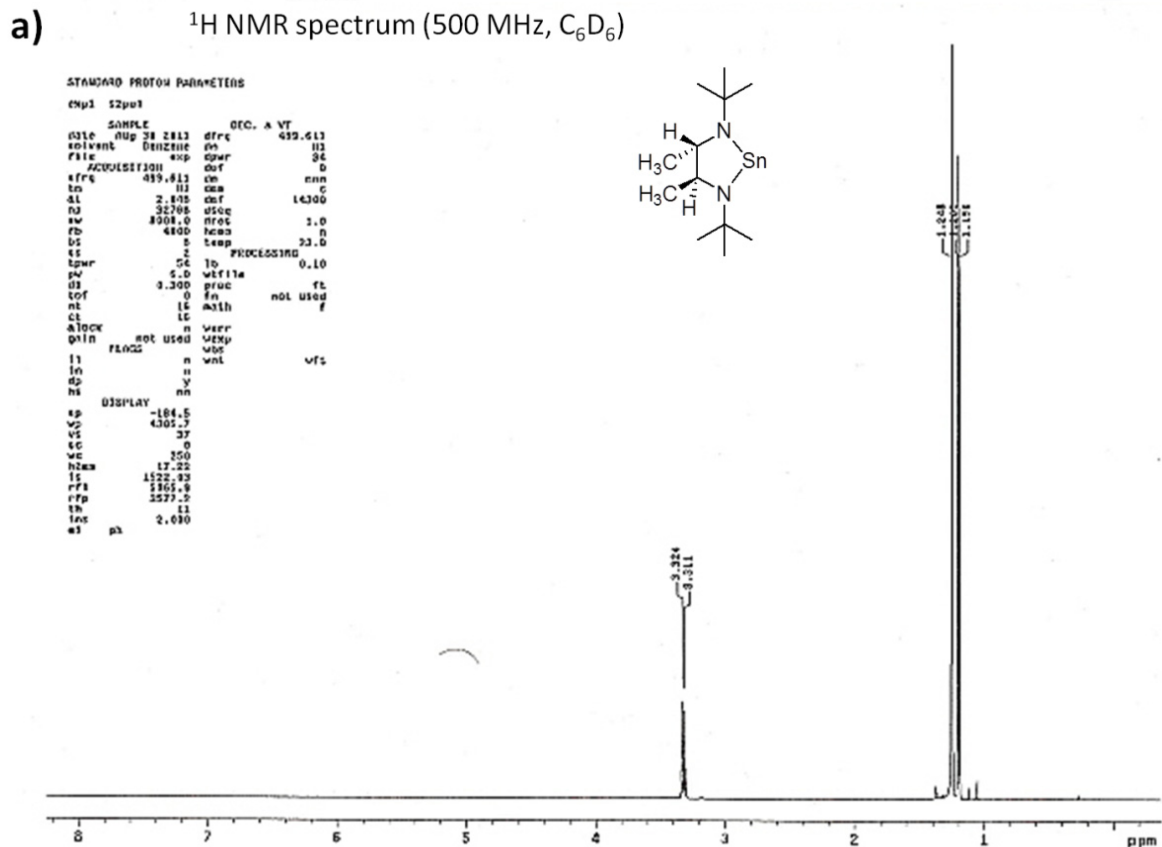

Figure A.4: NMR Spectra (500MHz , C_6D_6) of *rac*-1,3-Di-tert-butyl-4,5-dimethyl-1,3-diaza-2-stannacyclopentane-2-ylide: **(a)** ^{1}H NMR spectrum.

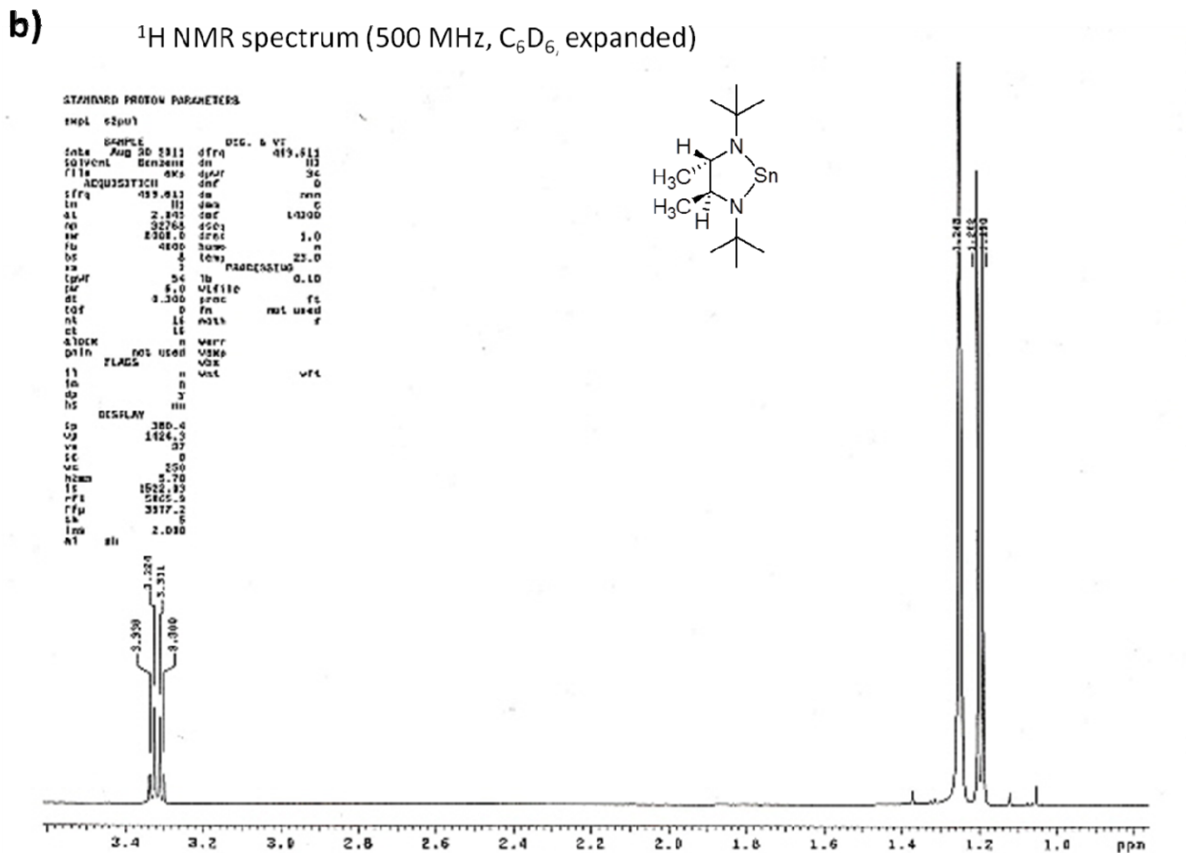

Figure A.4 (Continued): NMR Spectra (500MHz , C_6D_6) of *rac*-1,3-Di-tert-butyl-4,5-dimethyl-1,3-diaza-2-stannacyclopentane-2-ylide: **(b)** ^{1}H NMR spectrum (expanded).

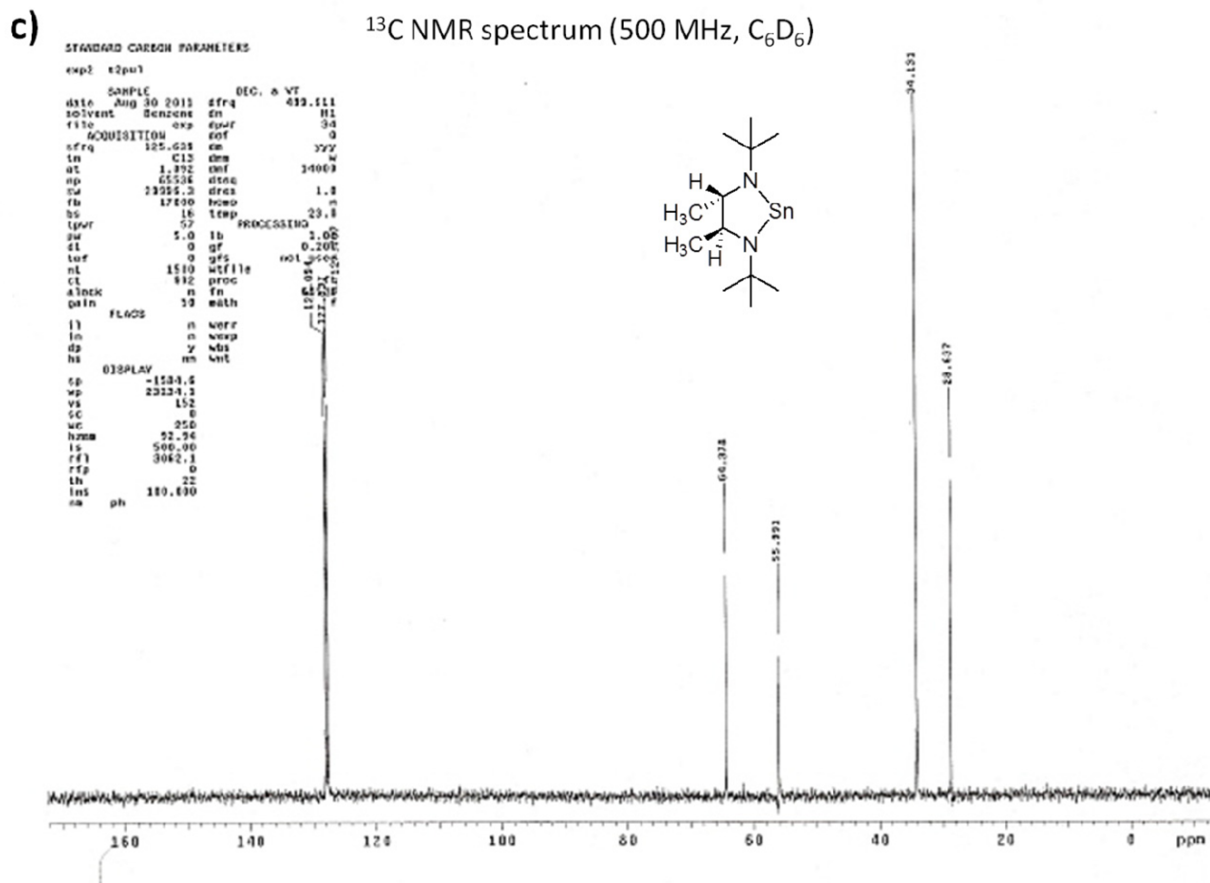

Figure A.4 (Continued): NMR Spectra (500MHz , C_6D_6) of *rac*-1,3-Di-tert-butyl-4,5-dimethyl-1,3-diaza-2-stannacyclopentane-2-ylide: **(c)** ^{13}C NMR spectrum.

A.2.3 X-ray crystal structures

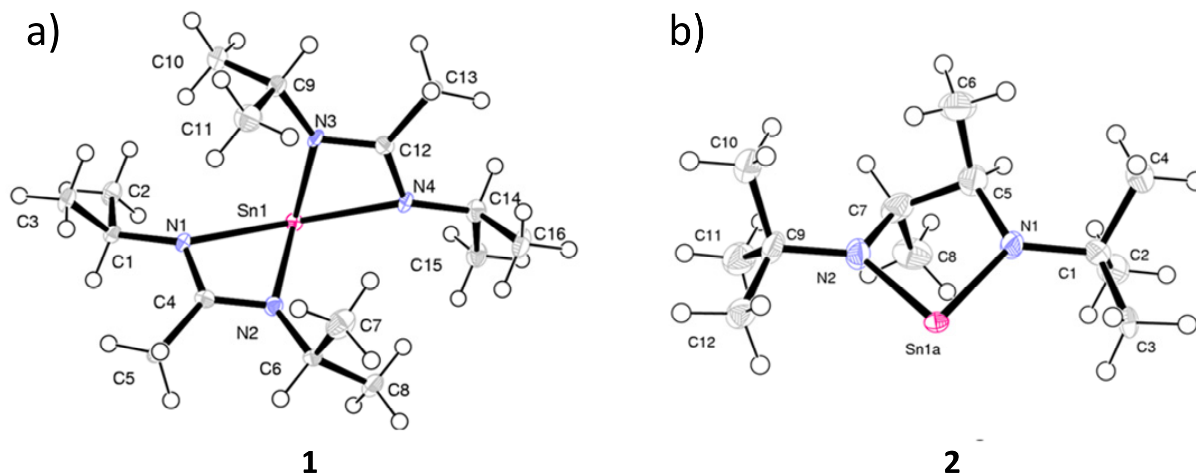

Figure A.5. ORTEP plots (50% thermal ellipsoids) of the X-ray crystal structures of compounds **1** and **2**. **(a)** Selected bond lengths (Å) and angles (deg) for **1**. Sn(1)-N(3) = 2.192(3), Sn(1)-N(2) = 2.195(2), Sn(1)-N(1) = 2.386(3), Sn(1)-N(4) =2.388(3), N(1)-C(4) = 1.325(4), N(2)-C(4) = 1.331(4), N(3)-C(12) =1.333(4), N(4)-C(12) =1.324(4), N(3)-Sn(1)-N(2) = 98.12(9), N(3)-Sn(1)-N(1) =92.88(9), N(2)-Sn(1)-N(1) = 57.82(9), N(1)-Sn(1)-N(4) =136.40(8), C(4)-N(1)-Sn(1) = 89.80(18), C(4)-N(2)-Sn(1) = 98.24(18), N(1)-C(4)-N(2) = 113.5(3). **(b)** Selected bond lengths (Å) and angles (deg) for **2**. Sn(1A)-N(1) = 2.026(7), Sn(1A)-N(2) = 2.055(8), N(1)-C(5) = 1.484(12), N(2)-C(7) = 1.492(12), C(5)-C(7) = 1.520(14), N(1)-Sn(1A)-N(2) = 81.8(3), C(5)-N(1)-Sn(1A) = 113.6(6), C(1)-N(1)-Sn(1A) = 127.6(6), C(9)-N(2)-Sn(1A) = 129.1(6), C(7)-N(2)-Sn(1A) = 111.7(6), N(1)-C(5)-C(7) = 108.7(8), N(1)-C(5)-C(6) =113.6(9), N(2)-C(7)-C(5) =108.2(8), N(2)-C(7)-C(8) = 112.0(8).

Table A.1: Crystallographic Data for **1** and **2**.[a]

Parameter	**1**: Sn(amd)$_2$	**2**: CAT
empirical formular	$C_{12}H_{34}N_4Sn$	$C_{12}H_{26}N_2Sn$
formular weight	401.16	317.04
crystal system	orthorhombic	monoclinic
space group	Pbca	P2(1)/c
Z	8	8
a, Å	12.6029(10)	23.3846(11)
b, Å	15.0179(12)	6.4294(3)
c, Å	20.6246(15)	21.7422(10)
α, deg	90	90
β, deg	90	117.5560
γ, deg	90	90
V, Å^3	3903.6(5)	2898.4(2)
d_{calcd}, g/cm^3	1.365	1.453
μ, mm^{-1}	1.310	1.740
2θ range, deg	2.33-25.65	1.87-25.87
R$_1$[b] (wR$_2$[c])	0.0266 (0.0598)	0.0644 (0.1733)
GOF (F^2)	1.001	1.292
Largest diff. peak and hole (e·Å^{-3})	0.368 and -0.395	1.724 and -1.849

[a]Mo Kα radiation (λ= 0.71073 Å) [b] $R_1 = \sum||F_o| - |F_c|| / \sum |F_o|$. [c] $wR_2 = \{\frac{\sum w(F_o{}^2 - F_c{}^2)^2}{\sum w(F_o{}^2)^2}\}^{1/2}$.

A.2.4 Thermal Gravimetric Analysis

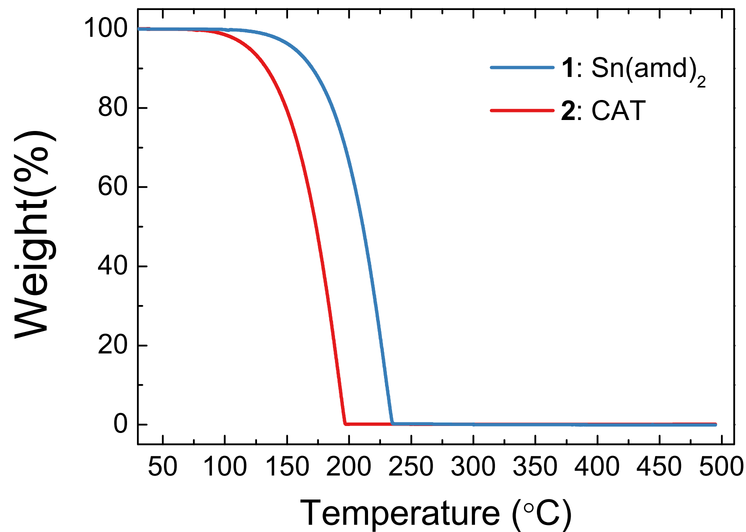

Figure A.6: Thermal Gravimetric Analysis (TGA) curves of **1** and **2**.

A.3 Acknowledgements

The data and results presented in this appendix were collected by Sang Bok Kim with help from the author.

Appendix B

ALD SnS Films from Cyclic Amide of Tin(II)

In addition to bis(N,N'-diisopropylacetamidinato)tin(II), SnS films can be deposited from *rac*-1,3-Di-tert-butyl-4,5-dimethyl-1,3-diaza-2-stannacyclopentane-2-ylide [Sn(II)(μ-NBu^t)CH(CH$_3$)CH(CH$_3$)(μ-NBu^t)], an alternative tin(II) precursor referred to here as cyclic amide of tin(II) or CAT. The synthesis and characterization of CAT are reported in Appendix A. This appendix summarizes the ALD process and the results of SnS films deposited from CAT and H_2S.

B.1 Experiment section

SnS thin films were deposited by atomic layer deposition (ALD) in a custom-built hot-wall ALD reactor from the reaction of CAT with H_2S, respectively. The growth temperature was

between 50 and 200 °C. The temperatures of the tin(II) precursor sources were kept at 45 °C, which give vapor pressures of 0.52 Torr. A gas mixture of 4% H_2S in N_2 (Airgas Inc.) was used as the source of sulfur. H_2S is a toxic, corrosive, and flammable gas (lower flammable limit of 4%) and it should be handled with caution.[53] Purified N_2 gas was used for assisting in the delivery of the tin(II) vapor from the precursor container to the deposition zone and also for purging between each precursor pulse. The precursor vapor and H_2S gas were injected sequentially into the deposition chamber to allow chemical reactions to occur successively on the substrate surface. The purge time after precursor vapor and H_2S exposure was set at 10 s to completely remove unreacted and by-product species and prevent reaction in the vapor phase. The deposition processes were done using the stop-flow ALD mode, reported in detailed elsewhere.[55, 56]

Thin film characterization. Surface morphology of the films was examined by using field-emission scanning electron microscopy (FESEM, Zeiss, Ultra-55). The film thickness was determined using a combination of cross-sectional SEM and x-ray fluorescence spectroscopy (XRF, Spectro, Xepos-III); the average thickness of rough films was determined by XRF utilizing a calibration curve of Sn $L_{\alpha 1}$ line intensity (count min^{-1}) versus the film thickness of smooth films measured by cross-sectional SEM. The elemental compositions of the films were determined by Rutherford backscattering spectrometry (RBS, Charles Evans RBS and Ionex 1.7 MV Tandetron). The crystal structures of SnS and GeS films were examined by x-ray diffraction (XRD, PANalytical X'Pert Pro) with Cu Kα radiation (λ = 1.542 Å) using θ-2θ scan.

B.2 Results

B.2.1 ALD growth behavior

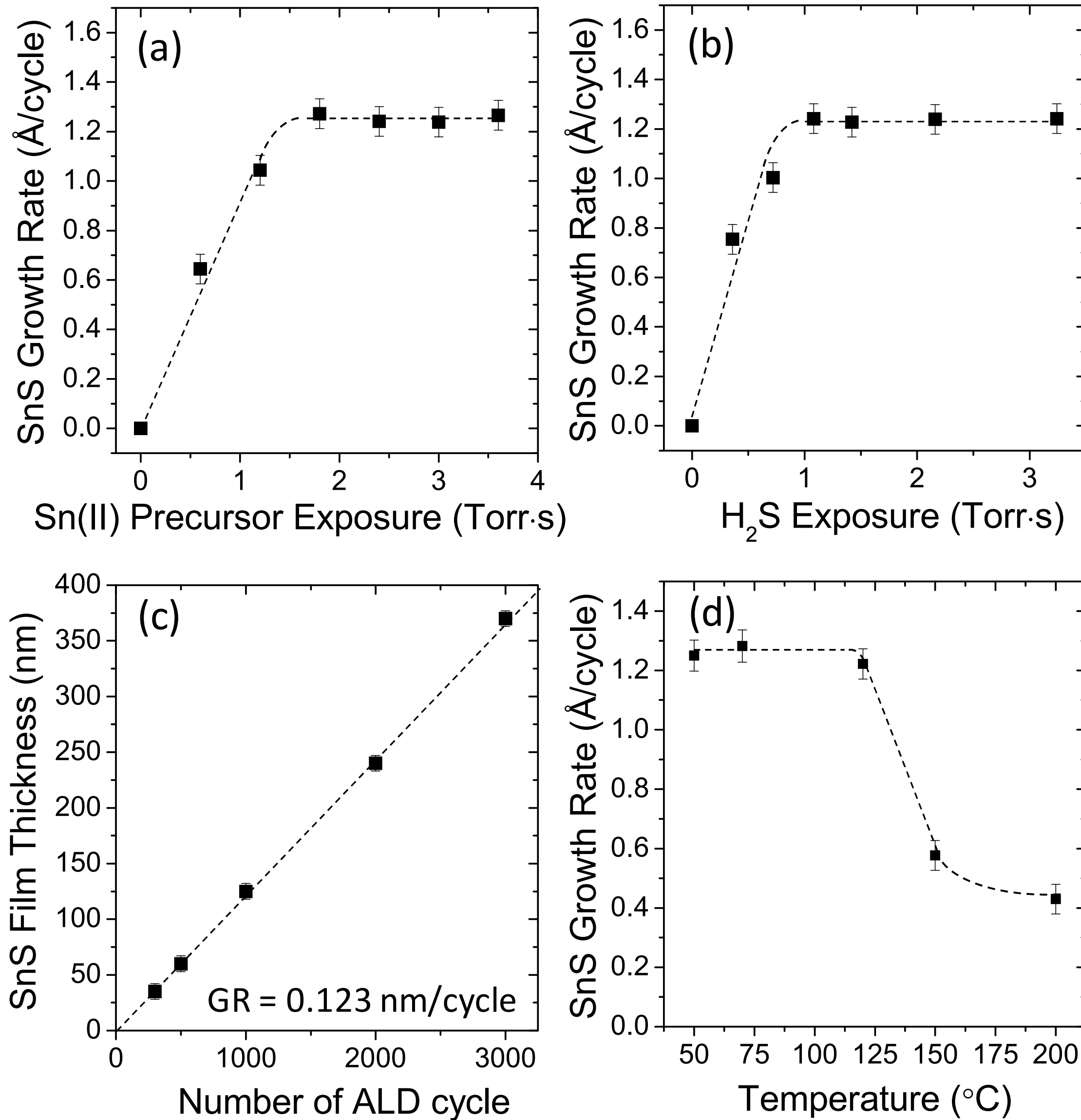

Figure B.1: The growth rate of SnS films at a deposition temperature of 70 °C for difference exposures of **(a)** CAT precursor at fixed H_2S exposure of 2.2 Torr·s and of **(b)** H_2S at fixed CAT exposure of 2.4 Torr·s. **(c)** thickness of SnS film on SiO_2 substrates using 1.8 Torr·s of CAT and 1.1 Torr·s of H_2S exposure as a function of the number of ALD growth cycles at 70 °C. **(d)** The growth rate of SnS films deposited between 50 and 200 °C.

B.2.2 Surface morphology and topography

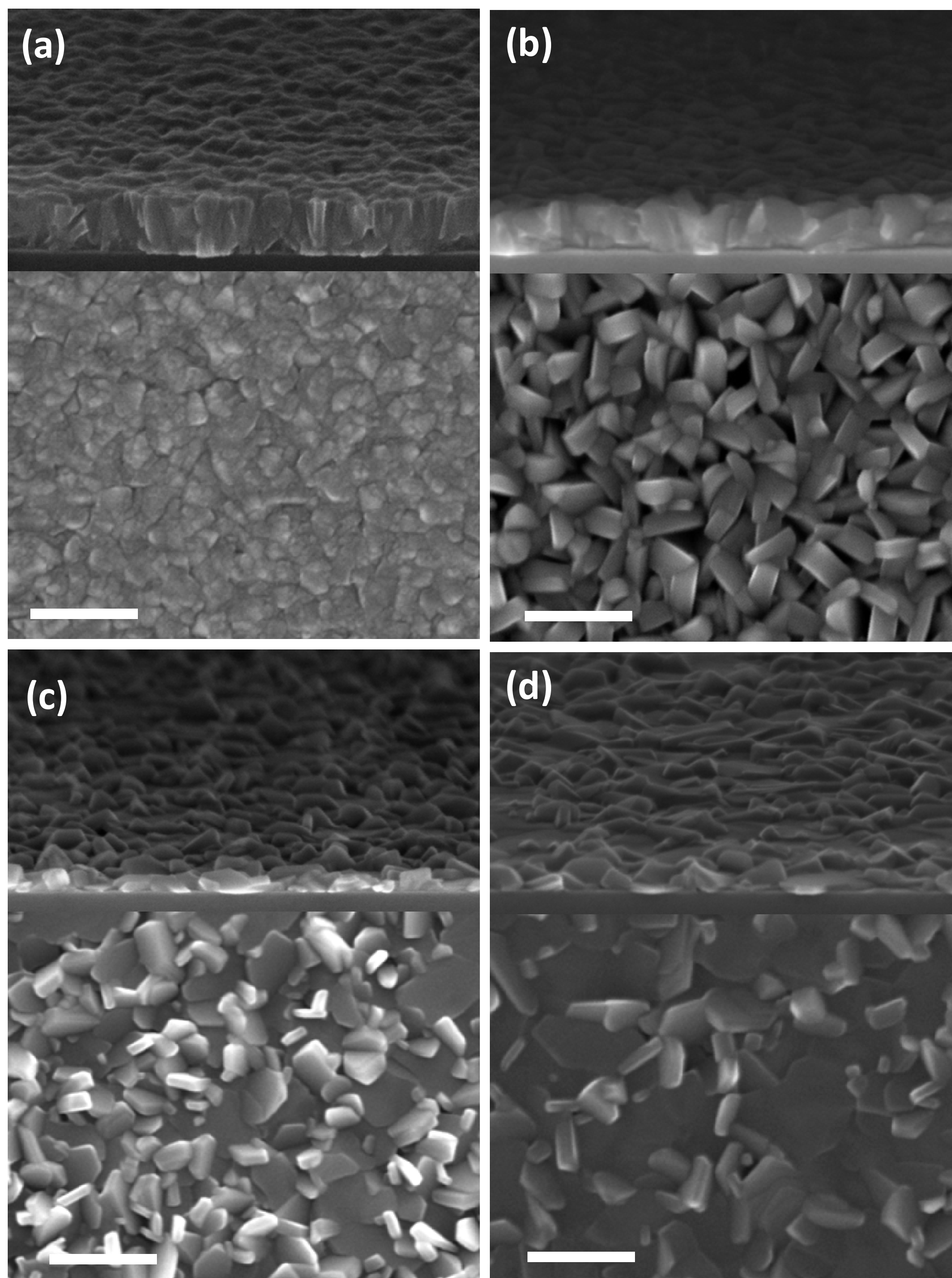

Figure B.2: Top view and cross-sectional SEM images of SnS films deposited on thermal oxide (SiO2) for 1000 ALD cycles at **(a)** 70 °C, **(b)** 120 °C, **(c)** 150 °C, and **(d)** 200 °C. The scale bar is 250 nm.

B.2.3 Crystal structure and film composition

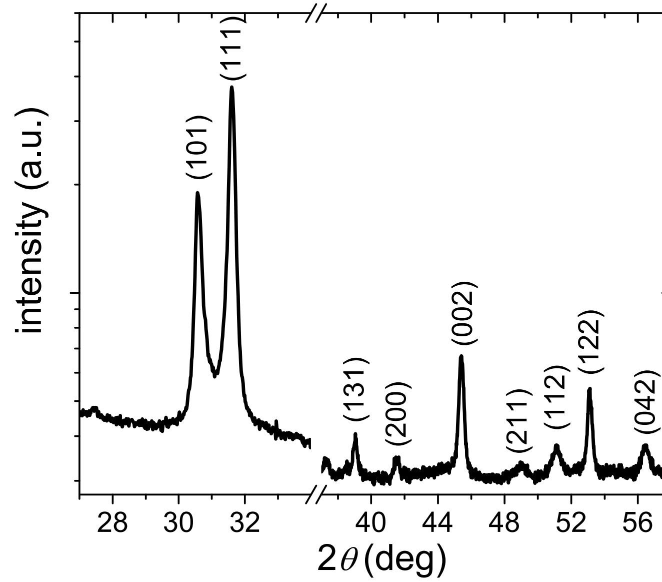

Figure B.3: XRD spectrum of 650 nm-thick SnS films deposited at 70 °C. All peaks match well with Herzenbergite SnS (*JCPDS* No. *39-0354, a* = 4.3291 Å*, b* = 11.1923 Å*, c* = 3.9838 Å).

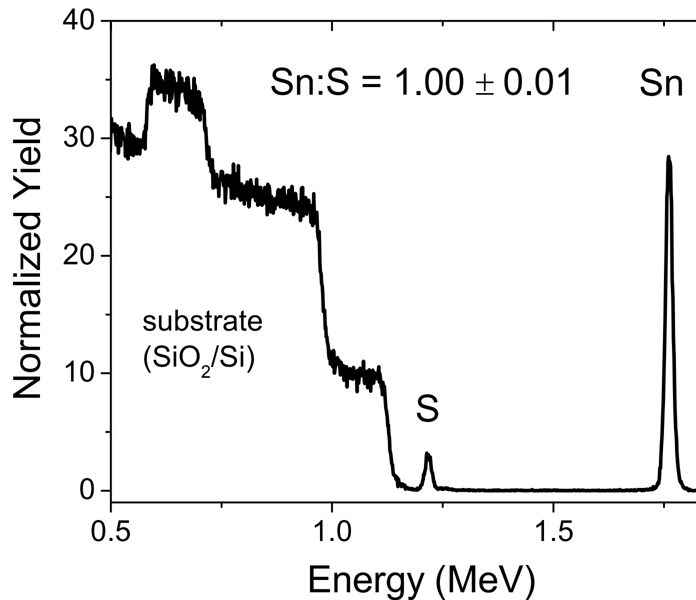

Figure B.4: An RBS spectrum of an ALD film deposited at 70 C, indicating stoichiometric SnS to within ± 1%.

Appendix C

Chlorine-doped SnS Thin Films

In addition to the antimony doped SnS presented in chapter 4, the other potential *n*-type dopant is chlorine. The source of chlorine used in this study was gaseous hydrogen chloride (HCl), which was inserted into the growth cycle of ALD SnS for doping. HCl is a very corrosive and toxic gas; it should be handled with a caution.[120] The SnS film used in this study was deposited from a cyclic amide of Sn(II) precursor (CAT) and 4% H_2S at 70 °C. The first doping attempt was made with pure HCl. Compared to SnS films, the resulting SnS(Cl) films, even at a low HCl:H_2S cycle-ratio less than 1%, showed a significantly lower growth rate (~ 2/3 of an undoped film) and much smaller grain sizes. This result is an indication that HCl might etch away SnS films during the growth process or change the surface condition of the film in a way that retards subsequent SnS growth after HCl exposure. Figure C.1 shows an EDX of a 100-nm SnS film before and after an exposure to 1 Torr of HCl for 6 min at 200 °C. This result indicates a complete conversion from SnS to $SnCl_x$. As a result, HCl is not an ideal precursor for this ALD-growth process since it reacts with the SnS film.

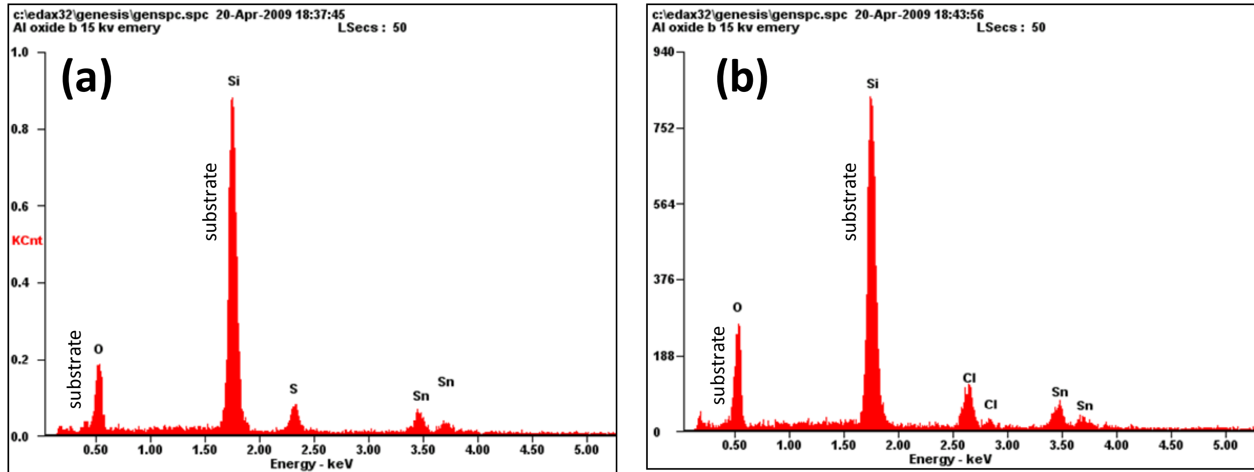

Figure C.1: EDX of a 100 nm-thick SnS film on SiO_2/Si wafer **(a)** before and **(b)** after an exposure to 1 Torr of HCl for 6 min at 200 °C, showing a complete conversion of the film from SnS to $SnCl_x$.

To reduce an effect of HCl on film growth, a dilute 1% HCl in N_2 was used to replace pure HCl. The growth rate and morphology of SnS(Cl) using 1% HCl (Figure C.2) is comparable to undoped SnS, when the HCl:H_2S cycle-ratio is roughly lower than 1:5. Similar to Sb-doped SnS, the resistivity of SnS(Cl) films (Table C.1) significantly increases compared to undoped SnS films. With higher dopant concentration, the films become intrinsic but do not convert to *n*-type. RBS cannot detect any Cl in the films even at a high HCl:H_2S cycle-ratio of 1:2, indicating less than *ca*. 1% Cl in all of these samples. It is worthwhile to note that the reproducibility of this process is quite poor since the concentration of Cl doped into SnS cannot be well controlled; HCl reacts with SnS and thus the amount of Cl incorporated into the films also depends on the HCl exposure (the product of exposed time and HCl partial pressure), in addition to the HCl:H_2S cycle-ratio. The amount of HCl exposed to the samples can fluctuate somewhat, depending on the condition of the tube and chamber wall since HCl is quite dilute and has a strong affinity to stainless steel and also the SnS coated on the chamber wall.

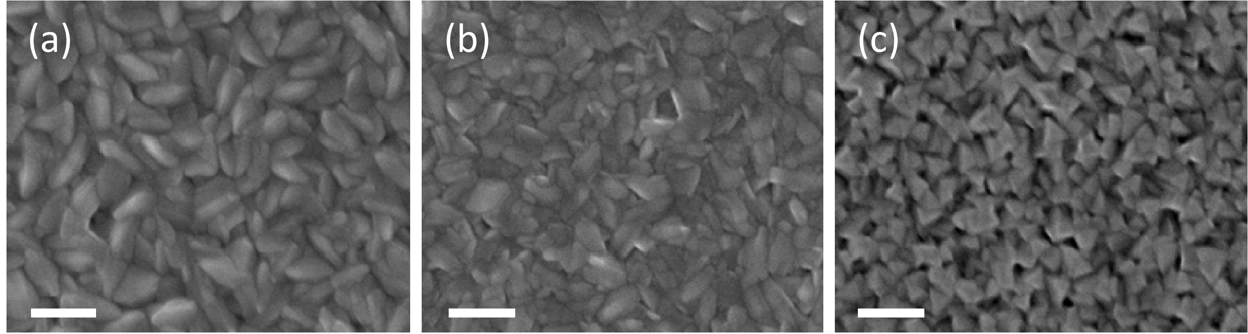

Figure C.2: SEM images of **(a)** SnS, **(b)** SnS (17% Cl), and **(c)** SnS(33% Cl). The scale bar is 200 nm.

Table C.1: Summary of growth rate and electrical properties of undoped and Cl-doped SnS films deposited at 70 °C using CAT for tin precursor with 4% H_2S and 1% HCl as co-reactants.

Sample	Cycle ratio $HCl:H_2S$	growth rate (Å/cycle)	resistivity (Ω cm)	carrier density (cm^{-3})	mobility (cm^2/Vs)
SnS	0:1	1.2	782	$+3.2\times10^{15}$	2.5
SnS(10% Cl)	1:9	1.2	3.40×10^4	below measurement sensitivity	
SnS(17% Cl)	1:5	1.2	$> 10^5$		
SnS(33% Cl)	1:2	0.9	$> 10^5$		

Appendix D

Schematic Diagram of the Reactor

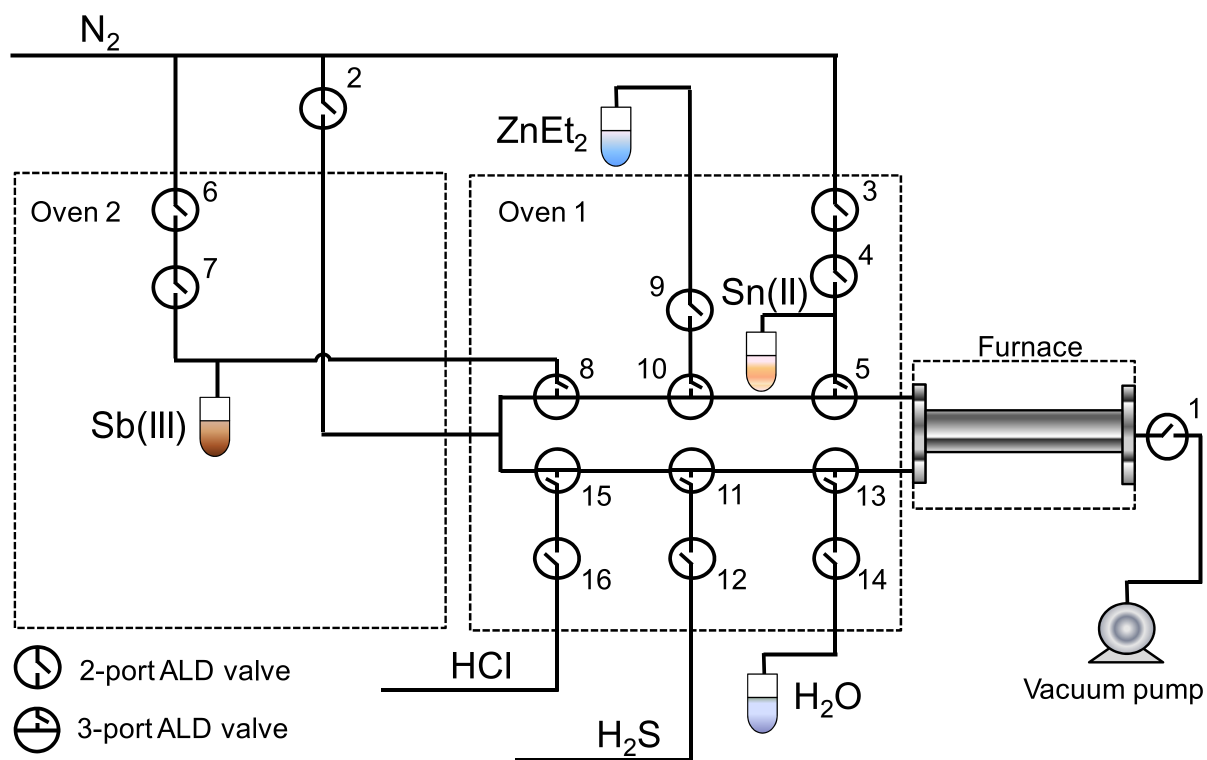

Figure D.1: Schematic diagram of the reactor.

References

1. Sorrell, S.; Speirs, J.; Bentley, R.; Brandt, A.; Miller, R., Global oil depletion: A review of the evidence. *Energy Policy* **2010,** 38, (9), 5290-5295.

2. *World Energy Outlook 2012.*; International Energy Agency: 2012.

3. Green, M. A.; Emery, K.; Hishikawa, Y.; Warta, W.; Dunlop, E. D., Solar cell efficiency tables (version 41). *Progress in Photovoltaics* **2013,** 21, (1), 11.

4. Scheer, R.; Schock, H.-W., *Chalcogenide Photovoltaics: Physics, Technologies, and Thin Film Devices*. Wiley-VCH: 2011.

5. Hamakawa, Y., *Thin-Film Solar Cells: Next Generation Photovoltaics and Its Application*. Springer: New York, 2003.

6. Poortmans, J.; Arkhipov, V., *Thin Film Solar Cells: Fabrication, Characterization and Applications*. Wiley: 2006.

7. Wadia, C.; Alivisatos, A. P.; Kammen, D. M., Materials Availability Expands the Opportunity for Large-Scale Photovoltaics Deployment. *Environmental Science & Technology* **2009,** 43, (6), 2072-2077.

8. Mittiga, A.; Salza, E.; Sarto, F.; Tucci, M.; Vasanthi, R., Heterojunction solar cell with 2% efficiency based on a Cu_2O substrate. *Applied Physics Letters* **2006,** 88, (16).

9. Wu, Y.; Wadia, C.; Ma, W. L.; Sadtler, B.; Alivisatos, A. P., Synthesis and photovoltaic application of copper(I) sulfide nanocrystals. *Nano Letters* **2008,** 8, (8), 2551-2555.

10. Puthussery, J.; Seefeld, S.; Berry, N.; Gibbs, M.; Law, M., Colloidal Iron Pyrite (FeS_2) Nanocrystal Inks for Thin-Film Photovoltaics. *Journal of the American Chemical Society* **2011,** 133, (4), 716-719.

11. Berry, N.; Cheng, M.; Perkins, C. L.; Limpinsel, M.; Hemminger, J. C.; Law, M., Atmospheric-Presure Chemical Vapor Deposition of Iron Pyrite Thin Films. *Adv. Energy Mater.* **2012,** 2, (9), 1124-1135.

12. Mitzi, D. B.; Gunawan, O.; Todorov, T. K.; Wang, K.; Guha, S., The path towards a high-performance solution-processed kesterite solar cell. *Solar Energy Materials and Solar Cells* **2011,** 95, (6), 1421-1436.

13. Scanlon, D. O.; Walsh, A., Bandgap engineering of $ZnSnP_2$ for high-efficiency solar cells. *Applied Physics Letters* **2012,** 100, (25), 251911.

14. Hartman, K.; Johnson, J. L.; Bertoni, M. I.; Recht, D.; Aziz, M. J.; Scarpulla, M. A.; Buonassisi, T., SnS thin-films by RF sputtering at room temperature. *Thin Solid Films* **2011,** 519, (21), 7421-7424.

15. Devika, M.; Reddy, N. K.; Ramesh, K.; Ganesan, R.; Gunasekhar, K. R.; Gopal, E. S. R.; Reddy, K. T. R., Thickness effect on the physical properties of evaporated SnS films. *J. Electrochem. Soc.* **2007,** 154, (2), H67-H73.

16. Reddy, N. K.; Hahn, Y. B.; Devika, M.; Sumana, H. R.; Gunasekhar, K. R., Temperature-dependent structural and optical properties of SnS films. *J. Appl. Phys.* **2007,** 101, (9), 093522.

17. Vidal, J.; Lany, S.; d'Avezac, M.; Zunger, A.; Zakutayev, A.; Francis, J.; Tate, J., Band-structure, optical properties, and defect physics of the photovoltaic semiconductor SnS. *Applied Physics Letters* **2012,** 100, (3).

18. Avellaneda, D.; Nair, M. T. S.; Nair, P. K., Polymorphic tin sulfide thin films of zinc blende and orthorhombic structures by chemical deposition. *J. Electrochem. Soc.* **2008,** 155, (7), D517-D525.

19. Reddy, K. T. R.; Reddy, N. K.; Miles, R. W., Photovoltaic properties of SnS based solar cells. *Sol. Energ. Mat. Sol. C* **2006,** 90, (18-19), 3041-3046.

20. Todorov, T. K.; Tang, J.; Bag, S.; Gunawan, O.; Gokmen, T.; Zhu, Y.; Mitzi, D. B., Beyond 11% Efficiency: Characteristics of State-of-the-Art $Cu_2ZnSn(S,Se)_4$ Solar Cells. *Advanced Energy Materials* **2013,** 3, (1), 34-38.

21. Mathews, N. R.; Anaya, H. B. M.; Cortes-Jacome, M. A.; Angeles-Chavez, C.; Toledo-Antonio, J. A., Tin Sulfide Thin Films by Pulse Electrodeposition: Structural, Morphological, and Optical Properties. *J. Electrochem. Soc.* **2010,** 157, (3), H337-H341.

22. Ichimura, M.; Takeuchi, K.; Ono, Y.; Arai, E., Electrochemical deposition of SnS thin films. *Thin Solid Films* **2000,** 361, 98-101.

23. Ortiz, A.; Alonso, J. C.; Garcia, M.; Toriz, J., Tin sulphide films deposited by plasma-enhanced chemical vapour deposition. *Semicond. Sci. Tech.* **1996,** 11, (2), 243-247.

24. Wiedemeier, H.; Schnering, H. G. V., Refinement of the Structures of GeS, GeSe, SnS and SnSe. *Z. Kristallogr.* **1978,** 148, (3-4), 295-303.

25. Albers, W.; Vink, H. J.; Haas, C.; Wasscher, J. D., Investigations on SnS. *J. Appl. Phys.* **1961,** 32, 2220-&.

26. Turan, E.; Kul, M.; Aybek, A. S.; Zor, M., Structural and optical properties of SnS semiconductor films produced by chemical bath deposition. *J. Phys. D Appl. Phys.* **2009,** 42, (24), 245408.

27. Gao, C.; Shen, H. L.; Sun, L.; Huang, H. B.; Lu, L. F.; Cai, H., Preparation of SnS films with zinc blende structure by successive ionic layer adsorption and reaction method. *Mater. Lett.* **2010,** 64, (20), 2177-2179.

28. Ghosh, B.; Das, M.; Banerjee, P.; Das, S., Fabrication of SnS thin films by the successive ionic layer adsorption and reaction (SILAR) method. *Semicond. Sci. Tech.* **2008,** 23, (12), 125013.

29. Kang, F.; Ichimura, M., Pulsed electrodeposition of oxygen-free tin monosulfide thin films using lactic acid/sodium lactate buffered electrolytes. *Thin Solid Films* **2010,** 519, (2), 725-728.

30. Brownson, J. R. S.; Georges, C.; Levy-Clement, C., Synthesis of a delta-SnS polymorph by electrodeposition. (vol 18, pg 6397, 2006). *Chem. Mater.* **2007,** 19, (12), 3080-3080.

31. Miles, R. W.; Ogah, O. E.; Zoppi, G.; Forbes, I., Thermally evaporated thin films of SnS for application in solar cell devices. *Thin Solid Films* **2009,** 517, (17), 4702-4705.

32. Devika, M.; Reddy, K. T. R.; Reddy, N. K.; Ramesh, K.; Ganesan, R.; Gopal, E. S. R.; Gunasekhar, K. R., Microstructure dependent physical properties of evaporated tin sulfide films. *J. Appl. Phys.* **2006,** 100, (2), 023518.

33. Johnson, J. B.; Jones, H.; Latham, B. S.; Parker, J. D.; Engelken, R. D.; Barber, C., Optimization of photoconductivity in vacuum-evaporated tin sulfide thin films. *Semicond. Sci. Tech.* **1999,** 14, (6), 501-507.

34. Tanusevski, A.; Poelman, D., Optical and photoconductive properties of SnS thin films prepared by electron beam evaporation. *Sol. Energ. Mat. Sol. C.* **2003,** 80, (3), 297-303.

35. Sajeesh, T. H.; Warrier, A. R.; Kartha, C. S.; Vijayakumar, K. P., Optimization of parameters of chemical spray pyrolysis technique to get *n* and *p*-type layers of SnS. *Thin Solid Films* **2010,** 518, (15), 4370-4374.

36. Calixto-Rodriguez, M.; Martinez, H.; Sanchez-Juarez, A.; Campos-Alvarez, J.; Tiburcio-Silver, A.; Calixto, M. E., Structural, optical, and electrical properties of tin sulfide thin films grown by spray pyrolysis. *Thin Solid Films* **2009,** 517, (7), 2497-2499.

37. Reddy, N. K.; Reddy, K. T. R., Preparation and characterisation of sprayed tin sulphide films grown at different precursor concentrations. *Mater. Chem. Phys.* **2007,** 102, (1), 13-18.

38. Bade, B. P.; Garje, S. S.; Niwate, Y. S.; Afzaal, M.; O'Brien, P., Tribenzyltin(IV) chloride Thiosemicarbazones: Novel Single Source Precursors for Growth of SnS Thin Films. *Chem. Vapor. Depos.* **2008,** 14, (9-10), 292-295.

39. Barone, G.; Chaplin, T.; Hibbert, T. G.; Kana, A. T.; Mahon, M. F.; Molloy, K. C.; Worsley, I. D.; Parkin, I. P.; Price, L. S., Synthesis and thermal decomposition studies of homo- and heteroleptic tin(IV) thiolates and dithiocarbamates: molecular precursors for tin sulfides. *J. Chem. Soc. Dalton.* **2002**, (6), 1085-1092.

40. Hibbert, T. G.; Mahon, M. F.; Molloy, K. C.; Price, L. S.; Parkin, I. P., Deposition of tin sulfide thin films from novel, volatile (fluoroalkythiolato)tin(IV) precursors. *J. Mater. Chem.* **2001,** 11, (2), 469-473.

41. Price, L. S.; Parkin, I. P.; Hardy, A. M. E.; Clark, R. J. H.; Hibbert, T. G.; Molloy, K. C., Atmospheric pressure chemical vapor deposition of tin sulfides (SnS, Sn_2S_3, and SnS_2) on glass. *Chem. Mater.* **1999,** 11, (7), 1792-1799.

42. Kim, J. Y.; George, S. M., Tin Monosulfide Thin Films Grown by Atomic Layer Deposition Using Tin 2,4-Pentanedionate and Hydrogen Sulfide. *J. Phys. Chem. C* **2010,** 114, (41), 17597-17603.

43. Barone, G.; Hibbert, T. G.; Mahon, M. F.; Molloy, K. C.; Price, L. S.; Parkin, I. P.; Hardy, A. M. E.; Field, M. N., Deposition of tin sulfide thin films from tin(IV) thiolate precursors. *J. Mater. Chem.* **2001,** 11, (2), 464-468.

44. Parkin, I. P.; Price, L. S.; Hibbert, T. G.; Molloy, K. C., The first single source deposition of tin sulfide coatings on glass: aerosol-assisted chemical vapour deposition using $[Sn(SCH_2CH_2S)_2]$. *J. Mater. Chem.* **2001,** 11, (5), 1486-1490.

45. Ristov, M.; Sinadinovski, G.; Grozdanov, I.; Mitreski, M., Chemical-Deposition of Tin(II) Sulfide Thin-Films. *Thin Solid Films* **1989,** 173, (1), 53-58.

46. Wang, Y.; Gong, H.; Fan, B. H.; Hu, G. X., Photovoltaic Behavior of Nanocrystalline SnS/TiO_2. *J. Phys. Chem. C* **2010,** 114, (7), 3256-3259.

47. Reddy, N. K.; Reddy, K. T. R., Growth of polycrystalline SnS films by spray pyrolysis. *Thin Solid Films* **1998,** 325, (1-2), 4-6.

48. Nair, M. T. S.; Nair, P. K.; Nair, P. K., Simplified Chemical-Deposition Technique for Good Quality Sns Thin-Films. *Semicond. Sci. Tech.* **1991,** 6, (2), 132-134.

49. Sajeesh, T. H.; Poornima, N.; Kartha, C. S.; Vijayakumar, K. P., Unveiling the defect levels in SnS thin films for photovoltaic applications using photoluminescence technique. *Phys. Status Solidi A* **2010,** 207, (8), 1934-1939.

50. Lide, D. R., *CRC Handbook of Chemistry and Physics; 81st edition*. CRC Press: 2000.

51. Lim, B. S.; Rahtu, A.; Park, J. S.; Gordon, R. G., Synthesis and characterization of volatile, thermally stable, reactive transition metal amidinates. *Inorg. Chem.* **2003,** 42, (24), 7951-7958.

52. Hausmann, D. M.; de Rouffignac, P.; Smith, A.; Gordon, R.; Monsma, D., Highly conformal atomic layer deposition of tantalum oxide using alkylamide precursors. *Thin Solid Films* **2003,** 443, (1-2), 1-4.

53. *Hydrogen Sulfide*; MSDS No.001029;. In Airgas Inc: Radnor, PA. April 26, 2010.

54. Dasgupta, N. P.; Mack, J. F.; Langston, M. C.; Bousetta, A.; Prinz, F. B., Design of an atomic layer deposition reactor for hydrogen sulfide compatibility. *Review of Scientific Instruments* **2010,** 81, (4).

55. Karuturi, S. K.; Liu, L. J.; Su, L. T.; Zhao, Y.; Fan, H. J.; Ge, X. C.; He, S. L.; Yoong, A. T. I., Kinetics of Stop-Flow Atomic Layer Deposition for High Aspect Ratio Template Filling through Photonic Band Gap Measurements. *J. Phys. Chem. C* **2010,** 114, (35), 14843-14848.

56. Heo, J.; Hock, A. S.; Gordon, R. G., Low Temperature Atomic Layer Deposition of Tin Oxide. *Chem. Mater.* **2010,** 22, (17), 4964-4973.

57. Devika, M.; Reddy, N. K.; Patolsky, F.; Gunasekhar, K. R., Ohmic contacts to SnS films: Selection and estimation of thermal stability. *J. Appl. Phys.* **2008,** 104, (12), 124503.

58. Ghosh, B.; Das, M.; Banerjee, P.; Das, S., Characteristics of metal/*p*-SnS Schottky barrier with and without post-deposition annealing. *Solid State Sci.* **2009,** 11, (2), 461-466.

59. Patterson, A. L., The Scherrer formula for x-ray particle size determination. *Phys. Rev.* **1939,** 56, (10), 978-982.

60. Nassary, M. M., Temperature dependence of the electrical conductivity, Hall effect and thermoelectric power of SnS single crystals. *J. Alloy Compd.* **2005,** 398, (1-2), 21-25.

61. Chandrasekhar, H. R.; Humphreys, R. G.; Zwick, U.; Cardona, M., Ir and Raman-Spectra of 4-6 Compounds SnS and SnSe. *Phys. Rev. B* **1977,** 15, (4), 2177-2183.

62. Ritter, D.; Weiser, K., Suppression of Interference-Fringes in Absorption-Measurements on Thin-Films. *Opt. Commun.* **1986,** 57, (5), 336-338.

63. Devika, M.; Reddy, N. K.; Patolsky, F.; Ramesh, K.; Gunasekhar, K. R., Temperature dependent structural properties of nanocrystalline SnS structures. *Appl. Phys. Lett.* **2009,** 95, (26), 261907.

64. Tyagi, P.; Vedeshwar, A. G., Anisotropic optical band gap of (102)- and (002)-oriented films of red HgI_2. *Phys. Rev. B* **2001,** 6324, (24), 245315.

65. Valiukonis, G.; Guseinova, D. A.; Krivaite, G.; Sileika, A., Optical-Spectra and Energy-Band Structure of Layer-Type $A^{iv}B^{vi}$ Compounds. *Phys. Status Solidi. B* **1986,** 135, (1), 299-307.

66. Albers, W.; Haas, C.; Vandermaesen, F., The Preparation and the Electrical and Optical Properties of Sns Crystals. *J. Phys. Chem. Solids* **1960,** 15, (3-4), 306-310.

67. Makinistian, L.; Albanesi, E. A., On the band gap location and core spectra of orthorhombic IV-VI compounds SnS and SnSe. *Phys. Status Solidi B* **2009,** 246, (1), 183-191.

68. Yue, G.; Lin, Y.; Wen, X.; Wang, L.; Peng, D., SnS homojunction nanowire-based solar cells. *J. Mater. Chem.* **2012,** 22, (32).

69. Ghosh, B.; Das, M.; Banerjee, P.; Das, S., Fabrication of the SnS/ZnO heterojunction for PV applications using electrodeposited ZnO films. *Semiconductor Science and Technology* **2009,** 24, (2).

70. Bashkirov, S. A.; Gremenok, V. F.; Ivanov, V. A.; Lazenka, V. V.; Bente, K., Tin sulfide thin films and Mo/*p*-SnS/*n*-CdS/ZnO heterojunctions for photovoltaic applications. *Thin Solid Films* **2012,** 520, (17), 5807-5810.

71. Gunasekaran, M.; Ichimura, M., Photovoltaic cells based on pulsed electrochemically deposited SnS and photochemically deposited CdS and $Cd_{1-x}Zn_xS$. *Solar Energy Materials and Solar Cells* **2007,** 91, (9), 774-778.

72. Sanchez-Juarez, A.; Tiburcio-Silver, A.; Ortiz, A., Fabrication of SnS_2/SnS heterojunction thin film diodes by plasma-enhanced chemical vapor deposition. *Thin Solid Films* **2005,** 480, 452-456.

73. Jiang, F.; Shen, H. L.; Wang, W.; Zhang, L., Preparation of SnS Film by Sulfurization and SnS/*a*-Si Heterojunction Solar Cells. *Journal of the Electrochemical Society* **2012,** 159, (3), H235-H238.

74. Sugiyama, M.; Reddy, K. T. R.; Revathi, N.; Shimamoto, Y.; Murata, Y., Band offset of SnS solar cell structure measured by X-ray photoelectron spectroscopy. *Thin Solid Films* **2011,** 519, (21), 7429-7431.

75. Niemegeers, A.; Burgelman, M.; Devos, A., On the CdS/$CuInSe_2$ Conduction-Band Discontinuity. *Applied Physics Letters* **1995,** 67, (6), 843-845.

76. Minemoto, T.; Matsui, T.; Takakura, H.; Hamakawa, Y.; Negami, T.; Hashimoto, Y.; Uenoyama, T.; Kitagawa, M., Theoretical analysis of the effect of conduction band offset of window/CIS layers on performance of CIS solar cells using device simulation. *Solar Energy Materials and Solar Cells* **2001,** 67, (1-4), 83-88.

77. Kumar, B.; Vasekar, P.; Pethe, S. A.; Dhere, N. G.; Koishiyev, G. I., $Zn_xCd_{1-x}S$ as a heterojunction partner for $CuIn_{1-x}Ga_xS_2$ thin film solar cells. *Thin Solid Films* **2009,** 517, (7), 2295-2299.

78. Minemoto, T.; Hashimoto, Y.; Satoh, T.; Negami, T.; Takakura, H.; Hamakawa, Y., Cu(In,Ga)Se_2 solar cells with controlled conduction band offset of window/Cu(In,Ga)Se_2 layers. *Journal of Applied Physics* **2001,** 89, (12), 8327-8330.

79. Kapilashrami, M.; Kronawitter, C. X.; Torndahl, T.; Lindahl, J.; Hultqvist, A.; Wang, W. C.; Chang, C. L.; Mao, S. S.; Guo, J. H., Soft X-ray characterization of $Zn_{1-x}Sn_xO_y$ electronic structure for thin film photovoltaics. *Physical Chemistry Chemical Physics* **2012,** 14, (29), 10154-10159.

80. Platzer-Bjorkman, C.; Torndahl, T.; Abou-Ras, D.; Malmstrom, J.; Kessler, J.; Stolt, L., Zn(O,S) buffer layers by atomic layer deposition in $Cu(In,Ga)Se_2$ based thin film solar cells: Band alignment and sulfur gradient. *J. Appl. Phys.* **2006,** 100, (4), 044506.

81. Sinsermsuksakul, P.; Heo, J.; Noh, W.; Hock, A. S.; Gordon, R. G., Atomic Layer Deposition of Tin Monosulfide Thin Films. *Advanced Energy Materials* **2011,** 1, (6), 1116-1125.

82. Sinton, R. A.; Cuevas, A. In *A Quasi-Steady-State Open-Circuit Voltage Method For Solar Cell Characterization*, Proc. 16th European Photovoltaic Solar Energy Conf., Glasgow, UK, 2000; Glasgow, UK, 2000; pp 1152-1155.

83. Sanders, B. W.; Kitai, A., Zinc Oxysulfide Thin-Films Grown by Atomic Layer Deposition. *Chemistry of Materials* **1992,** 4, (5), 1005-1011.

84. Persson, C.; Platzer-Bjorkman, C.; Malmstrom, J.; Torndahl, T.; Edoff, M., Strong valence-band offset bowing of $ZnO_{1-x}S_x$ enhances *p*-type nitrogen doping of ZnO-like alloys. *Physical Review Letters* **2006,** 97, (14), 146403.

85. Pudov, A. O.; Kanevce, A.; Al-Thani, H. A.; Sites, J. R.; Hasoon, F. S., Secondary barriers in Cd_S-$CuIn_{1-x}Ga_xSe_2$ solar cells. *J. Appl. Phys.* **2005,** 97, (6), 064901.

86. Pudov, A. O.; Sites, J. R.; Contreras, M. A.; Nakada, T.; Schock, H. W., CIGS J-V distortion in the absence of blue photons. *Thin Solid Films* **2005,** 480, 273-278.

87. Liu, X. X.; Sites, J. R., Solar-Cell Collection Efficiency and Its Variation with Voltage. *Journal of Applied Physics* **1994,** 75, (1), 577-581.

88. Hegedus, S. S.; Shafarman, W. N., Thin-film solar cells: Device measurements and analysis. *Progress in Photovoltaics* **2004,** 12, (2-3), 155-176.

89. Kerr, M. J.; Cuevas, A., Generalized analysis of the illumination intensity vs. open-circuit voltage of solar cells. *Solar Energy* **2004,** 76, (1-3), 263-267.

90. Sites, J.; Pan, J., Strategies to increase CdTe solar-cell voltage. *Thin Solid Films* **2007,** 515, (15), 6099-6102.

91. Devika, M.; Reddy, N. K.; Ramesh, K.; Gunasekhar, K. R.; Gopal, E. S. R.; Reddy, K. T. R., Low resistive micrometer-thick SnS : Ag films for optoelectronic applications. *Journal of the Electrochemical Society* **2006,** 153, (8), G727-G733.

92. Zhang, S. A.; Cheng, S. Y., Thermally evaporated SnS:Cu thin films for solar cells. *Micro & Nano Letters* **2011,** 6, (7), 559-562.

93. Dussan, A.; Mesa, F.; Gordillo, G., Effect of substitution of Sn for Bi on structural and electrical transport properties of SnS thin films. *Journal of Materials Science* **2010,** 45, (9), 2403-2407.

94. Yang, R. B.; Bachmann, J.; Reiche, M.; Gerlach, J. W.; Gosele, U.; Nielsch, K., Atomic Layer Deposition of Antimony Oxide and Antimony Sulfide. *Chemistry of Materials* **2009,** 21, (13), 2586-2588.

95. Heald, S.; Stern, E.; Brewe, D.; Gordon, R.; Crozier, D.; Jiang, D. T.; Cross, J., XAFS at the Pacific Northwest Consortium-Collaborative Access Team undulator beamline. *Journal of Synchrotron Radiation* **2001,** 8, 342-344.

96. Na, J. S.; Peng, Q.; Scarel, G.; Parsons, G. N., Role of Gas Doping Sequence in Surface Reactions and Dopant Incorporation during Atomic Layer Deposition of Al-Doped ZnO. *Chemistry of Materials* **2009,** 21, (23), 5585-5593.

97. Kim, S. K.; Choi, G. J.; Kim, J. H.; Hwang, C. S., Growth behavior of Al-doped TiO_2 thin films by atomic layer deposition. *Chemistry of Materials* **2008,** 20, (11), 3723-3727.

98. Heo, J.; Liu, Y. Q.; Sinsermsuksakul, P.; Li, Z. F.; Sun, L. Z.; Noh, W.; Gordon, R. G., $(Sn,Al)O_x$ Films Grown by Atomic Layer Deposition. *Journal of Physical Chemistry C* **2011,** 115, (20), 10277-10283.

99. Sayers, D. E.; Bunker, B. A., X-Ray Absorption: Basic Principles of EXAFS, SEXAFS and XANES. In Koningsberger, D. C.; Prin, R., Eds. Wiley: New York, 1988; p 211.

100. Ravel, B.; Newville, M., ATHENA, ARTEMIS, HEPHAESTUS: data analysis for X-ray absorption spectroscopy using IFEFFIT. *Journal of Synchrotron Radiation* **2005,** 12, 537-541.

101. Kurbanova, R. D.; Movsumzade, A. A.; Allazov, M. R., The SnS-Sb System. *Inorganic Materials* **1987,** 23, (11), 1585-1587.

102. Heald, S. M.; Kaspar, T.; Droubay, T.; Shutthanandan, V.; Chambers, S.; Mokhtari, A.; Behan, A. J.; Blythe, H. J.; Neal, J. R.; Fox, A. M.; Gehring, G. A., X-ray absorption fine structure and magnetization characterization of the metallic Co component in Co-doped ZnO thin films. *Physical Review B* **2009,** 79, (7).

103. Fons, P.; Yamada, A.; Iwata, K.; Matsubara, K.; Niki, S.; Nakahara, K.; Takasu, H., An EXAFS and XANES study of MBE grown Cu-doped ZnO. *Nuclear Instruments & Methods in Physics Research Section B-Beam Interactions with Materials and Atoms* **2003,** 199, 190-194.

104. McCandless, B. E.; Sites, J. R., *Cadmimum Telluride Solar Cells (Handbook of Photovoltaic Science and Engineering)*. John Wiley & Sons, Ltd: 2003.

105. Terheggen, M.; Heinrich, H.; Kostorz, G.; Romeo, A.; Baetzner, D.; Tiwari, A. N.; Bosio, A.; Romeo, N., Structural and chemical interface characterization of CdTe solar cells by transmission electron microscopy. *Thin Solid Films* **2003,** 431, 262-266.

106. Rose, D. H.; Hasoon, F. S.; Dhere, R. G.; Albin, D. S.; Ribelin, R. M.; Li, X. S.; Mahathongdy, Y.; Gessert, T. A.; Sheldon, P., Fabrication procedures and process sensitivities for CdS/CdTe solar cells. *Progress in Photovoltaics* **1999,** 7, (5), 331-340.

107. Guo, Q.; Ford, G. M.; Yang, W. C.; Walker, B. C.; Stach, E. A.; Hillhouse, H. W.; Agrawal, R., Fabrication of 7.2% Efficient CZTSSe Solar Cells Using CZTS Nanocrystals. *Journal of the American Chemical Society* **2010,** 132, (49), 17384-17386.

108. Ahmed, S.; Reuter, K. B.; Gunawan, O.; Guo, L.; Romankiw, L. T.; Deligianni, H., A High Efficiency Electrodeposited Cu_2ZnSnS_4 Solar Cell. *Advanced Energy Materials* **2012,** 2, (2), 253-259.

109. Todorov, T. K.; Gunawan, O.; Gokmen, T.; Mitzi, D. B., Solution-processed $Cu(In,Ga)(S,Se)_2$ absorber yielding a 15.2% efficient solar cell. *Progress in Photovoltaics* **2013,** 21, (1), 82-87.

110. Ohashi, D.; Nakada, T.; Kunioka, A., Improved CIGS thin-film solar cells by surface sulfurization using In_2S_3 and sulfur vapor. *Solar Energy Materials and Solar Cells* **2001,** 67, (1-4), 261-265.

111. Ghosh, B.; Bhattacharjee, R.; Banerjee, P.; Das, S., Structural and optoelectronic properties of vacuum evaporated SnS thin films annealed in argon ambient. *Applied Surface Science* **2011,** 257, (8), 3670-3676.

112. Sinsermsuksakul, P.; Hartman, K.; Kim, S. B.; Heo, J.; Sun, L. Z.; Park, H. H.; Chakraborty, R.; Buonassisi, T.; Gordon, R. G., Enhancing the efficiency of SnS solar cells via band-offset engineering with a zinc oxysulfide buffer layer. *Applied Physics Letters* **2013,** 102, (5).

113. Thompson, C. V., Grain-Growth in Thin-Films. *Annual Review of Materials Science* **1990,** 20, 245-268.

114. Devika, M.; Reddy, N. K.; Reddy, S. V.; Ramesh, K.; Gunasekhar, K. R., Influence of rapid thermal annealing (RTA) on the structural and electrical properties of SnS films. *Journal of Materials Science-Materials in Electronics* **2009,** 20, (11), 1129-1134.

115. Wiedemeier, H.; Csillag, F. J., Decomposition and Thermodynamic Properties of Sn_2S_3. *Zeitschrift Fur Anorganische Und Allgemeine Chemie* **1980,** 469, (10), 197-206.

116. Bradley, R. S., Rates of Evaporation .IV. The Rate of Evaporation and Vapour Pressure of Rhombic Sulphur. *Proceedings of the Royal Society of London Series a-Mathematical and Physical Sciences* **1951,** 205, (1083), 553-563.

117. Meyer, B., Elemental Sulfur. *Chemical Reviews* **1976,** 76, (3), 367-388.

118. Kliegman, J. M.; Barnes, R. K., Glyoxal derivatives—I: Conjugated aliphatic diimines from glyoxal and aliphatic primary amines. *Tetrahedron* **1970,** 26, (10), 2555-2560.

119. Mistryukov, E. A., Facile and scalable synthesis of imidazolium halides using dimethylmethyleneammonium salts as ring closing reagents. *Mendeleev Communications* **2006,** 16, (5), 258-259.

120. *Hydrogen Chloride*; MSDS No.001028;. In Airgas Inc: Radnor, PA. April 26, 2010.